INTERNATIONAL CONFERENCE 2026

"Empowering a Sustainable World through Science and Engineering in the AI Era"

PROCEEDING BOOK

THE INTERNATIONAL CONFERENCE 2026

Theme

"Empowering a Sustainable World through Science and Engineering in the AI Era"

6 – 7 July 2026
Thaksin University, Songkhla, Thailand

Organized by
Faculty of Engineering
Thaksin University

Co-hosted by
Council of Engineers Thailand
The Engineering Institute of Thailand

E – PROCEEDING BOOK

OF THE INTERNATIONAL CONFERENCE 2026

Theme

“Empowering a Sustainable World through Science and Engineering in the AI Era”

6 – 7 July 2026
Thaksin University, Songkhla, Thailand

Published by:
Faculty of Engineering, Thaksin University
Songkhla, Thailand

Publication Year: 2026

MESSAGE FROM THE DEAN

On behalf of the Faculty of Engineering, Thaksin University, I would like to express my sincere appreciation to our co-host organizations, Council of Engineers Thailand and The Engineering Institute of Thailand, for their invaluable support and collaboration. Their partnership has played an important role in strengthening the academic and professional dimensions of this conference.

I would also like to extend my deepest gratitude to our four distinguished keynote speakers: Professor Dr. Chi-Chuan Wang, Professor Emeritus Dr. Worasak Kanok-Nukulchai, Professor Dr. Akito Takasaki, and Dr. Tossaporn Sreeiam. Their expertise, perspectives, and valuable contributions have greatly enriched the academic program and provided inspiration to researchers and participants from diverse fields.

My sincere appreciation also goes to all authors and researchers who contributed their research to the international conference. The quality and diversity of the submitted works reflect the dedication of the research community to advancing knowledge and developing innovative solutions in science, engineering, technology and sustainable development.

I would also like to express my heartfelt appreciation to the faculty members, staff, organizing committees and supporting personnel of the Faculty of Engineering, Thaksin University. Their dedication, teamwork, and considerable efforts throughout the preparation and organization of the conference have been essential to its success.

Finally, I sincerely hope that this conference will not only serve as a platform for disseminating research and innovation but also strengthen professional networks, inspire new ideas, and create opportunities for future academic and research collaboration at both national and international levels.

Assoc. Prof. Dr. Jatuporn Kaew-On
Dean of Faculty of Engineering
Thaksin University

PREFACE

The International Conference 2026, under the theme "Empowering a Sustainable World through Science and Engineering in the AI Era," was held from 6 – 7 July 2026 at Thaksin University, Songkhla, Thailand.

The International Conference 2026 provided an international platform for researchers, academics, engineers, professionals, and students to exchange knowledge, research findings, innovations, and experiences in science and engineering. Particular emphasis was placed on the integration of emerging technologies, artificial intelligence, and engineering solutions to address global challenges and contribute to sustainable development.

The International Conference 2026 covered a broad range of research areas, including artificial intelligence (AI) for Sustainable Development, renewable energy and green technology, environmental engineering and climate solutions, sustainable materials and green manufacturing, the Internet of Things (IoT) and smart sensing, appropriate technology and other related areas of science and engineering.

These proceedings compile the research papers accepted for publication and presented during The International Conference 2026. The Organizing Committee sincerely appreciates the contributions of all authors, reviewers, keynote speakers, session chairs, participants, supporting organizations and partner institutions whose valuable contributions made the conference possible.

We hope that these proceedings will serve as a valuable academic resource, promote the dissemination of scientific knowledge and innovation, and contribute to strengthening research networks and international collaboration toward a more sustainable future.

Organizing Committee
International Conference 2026
Faculty of Engineering, Thaksin University

SCIENTIFIC REVIEW COMMITTEE

To ensure the academic quality and integrity of the conference proceedings, each manuscript included in the proceedings was independently reviewed by three reviewers from different institutions. Their careful evaluations and recommendations contributed significantly to maintaining the scientific quality and academic standards of the conference

The Organizing Committee gratefully acknowledges the contributions of the reviewers who provided their expertise, constructive feedback, and valuable comments in evaluating the manuscripts submitted to the International Conference 2026. The reviewers are listed below:

Name	Affiliation
Prof. Dr. Chanan Angsuthanasombat	Mahidol University
Prof. Dr. Jongjit Hirunlabh	Burapha University
Prof. Dr. Joseph Khedari	Bangkokthonburi University
Assoc. Prof. Dr. Arnon Isaramongkolrak	Nakhon Pathom Rajabhat University, Thailand
Assoc. Prof. Dr. Jarungwit Boonnorat	Rajamangala University of Technology Thanyaburi
Assoc. Prof. Dr. Jompob Waewsak	Thaksin University
Assoc. Prof. Dr. Nipon Ketjoy	Naresuan University
Assoc. Prof. Dr. Patiwet Wuttisarnwattana	Chiang Mai University
Assoc. Prof. Dr. Pramual Choorat	Srinakharinwirot University
Assoc. Prof. Dr. Prapita Thanarak	Naresuan University
Assoc. Prof. Dr. Santi Chuetor	King Mongkut's University of Technology North Bangkok
Assoc. Prof. Dr. Suratsavadee Koonlaboon Korkua	Walailak University
Asst. Prof. Dr. Amawasee Rukrueng	Thaksin University
Asst. Prof. Dr. Arak Bunmat	Rajamangala University of Technology Isan
Asst. Prof. Dr. Chakchai Meaunmas	Thaksin University
Asst. Prof. Chakrit Panpean	King Mongkut's University of Technology North Bangkok
Asst. Prof. Dr. Naruemon Setthaya	University of Phayao
Asst. Prof. Dr. Niramol Juntarachat	Thaksin University
Asst. Prof. Dr. Pagasukon Mekrattanachai	University of Phayao
Asst. Prof. Dr. Patipat Vongruang	University of Phayao
Asst. Prof. Dr. Prayut Kongsuk	Rajamangala University of Technology Tawan-ok, Chanthaburi Campus
Asst. Prof. Dr. Promphak Boonraksa	Rajamangala University of Technology Suvarnabhumi
Asst. Prof. Dr. Sirinuch Jindaruk	Naresuan University
Asst. Prof. Dr. Surapong Rattanakul	King Mongkut's University of Technology Thonburi
Asst. Prof. Dr. Terapong Boonraksa	Rajamangala University of Technology Rattanakosin

Asst. Prof. Dr. Thitima Na Songkhla	Thaksin University
Asst. Prof. Dr. Tosaphol Ratniyomchai	Suranaree University of Technology
Asst. Prof. Dr. Warit Werapun	Prince of Songkla University
Asst. Prof. Dr. Weerawut Naebpetch	Thaksin University
Dr. Alongkorn Pirayawaraporn	Chiang Mai University
Dr. Apichai Suyaphan	King Mongkut's University of Technology Thonburi, Thailand
Dr. Chakkresit Chindawong	University of Phayao
Dr. Duangduen Asavasuthirakul	Naresuan University
Dr. Jerawat Sopajarn	Thaksin University
Dr. Jermphiphut Jaruenpunyasak	Prince of Songkla University
Dr. Jitimon Angskun	Rangsit University
Dr. Jittima Varagul	Suranaree University of Technology
Dr. Kidsanapong Puntsri	Rajamangala University of Technology Isan
Mr. Kumpanat Suttijirapan	Rajamangala University of Technology Lanna
Dr. Mojtaba Safari	Thaksin University
Dr. Nattapong Suksaba	Kasetsart University
Dr. Nopphadol Udomluck	Chiang Mai University
Dr. Patipat Kamdenlek	Thaksin University
Dr. Ploybussara Gomasang	Silpakorn University
Dr. Pokpong Prakobkaew	King Mongkut's University of Technology North Bangkok
Dr. Pracha Kumpakdee	Ubon Ratchathani University
Dr. Prathai Watcharakitchakorn	Silpakorn University
Mr. Ruttana Petchtom	Rajamangala University of Technology Lanna
Dr. Sompoj Komkaew	Rajamangala University of Technology Rattanakosin
Dr. Supachai Kaewpoun	Thaksin Universiy
Dr. Suttipan Aksornnium	Thaksin University
Dr. Thammarit Khamplod	Kasetsart University
Dr. Thatchayut Unjitwattana	Chiang Mai University
Mr. Wiwat Suren	Thaksin University

CONTENTS

I. Artificial Intelligence for Sustainable Development

Autoencoder-Guided Reinforcement Learning on Payload Images for Network Intrusion Detection

Pitpibul Kukong and Wanida Putthividhya

Department of Computer Science, Faculty of Science and Technology, Thammasat University
Pathum Thani, 12130, Thailand.
*Correspondence: pitpibul.kuko@dome.tu.ac.th

Abstract

Network Intrusion Detection Systems face major challenges in detecting zero-day attacks due to the scarcity and class imbalance of labeled training data. This paper proposes an unsupervised autoencoder-guided reinforcement learning framework for intrusion detection that eliminates the need for labeled attack data. Packet payloads are represented as grayscale images and processed directly by a Deep Q-Network agent. A convolutional autoencoder is trained exclusively on benign traffic to learn normal behavior patterns. The resulting reconstruction error is used to generate label-free reward signals, enabling reinforcement learning without ground truth labels. This design avoids the limitations of supervised reward mechanisms and mitigates the impact of class imbalance. The proposed framework is evaluated on the CIC-IDS2017 dataset. Experimental results show that the model achieves a recall of 99.80%. This is comparable to supervised baselines (99.94%) despite using only benign data during training. In addition, the framework remains robust under severe class imbalance in the data. The framework maintains high recall, whereas supervised models exhibit significant performance degradation. Recall is adopted as the primary evaluation metric because missing attacks is more critical than raising false alarms in security applications. These results demonstrate that effective and robust intrusion detection can be achieved without labeled attack data, making the proposed approach suitable for real-world deployment where such data are scarce and imbalanced.

Keywords: network intrusion detection; deep reinforcement learning; autoencoder; unsupervised learning

1. Introduction

Network security remains a critical concern as cyber threats continue to evolve in sophistication and scale. The global average cost of data breaches reached 4.88 million dollars in 2024, representing a 10% increase from the previous year [1]. The FBI reported losses exceeding 16.6 billion dollars from more than 859,000 cybercrime complaints in 2024, marking a 33% increase from 2023 [2]. Traditional signature-based intrusion detection systems can identify known attacks but fail to detect zero-day exploits and polymorphic malware. Machine learning approaches have been introduced to address this limitation. However, they face two fundamental challenges. First, supervised learning requires labeled datasets that include both benign and attack samples. In practice, such datasets are difficult to obtain and maintain. Network traffic is highly imbalanced, with benign samples dominating and attack instances being rare and unevenly distributed. This imbalance degrades the performance of supervised models and limits their effectiveness in real-world deployment. Second, many anomaly detection methods rely on static thresholds. These methods produce high false positive rates and require manual recalibration when network conditions change.

Recent advances in deep learning have improved intrusion detection performance. Convolutional neural networks have shown strong results when network traffic is represented as images [3, 4]. However, these approaches still rely on supervised learning and require labeled attack data. Reinforcement learning (RL) has also been explored for adaptive decision-making in network security [5]. Nevertheless, most existing RL-based approaches depend on reward signals derived from ground truth labels. This design effectively reduces reinforcement learning to a form of supervised learning and inherits the same limitations under data scarcity and class imbalance.

This paper proposes an unsupervised autoencoder-guided reinforcement learning framework for network intrusion detection. The framework eliminates the need for labeled attack data. A key component is a label-free reward mechanism derived from reconstruction error. A convolutional autoencoder is trained exclusively on benign traffic to learn a profile of normal behavior. The reconstruction error is used to generate rewards that guide a Deep Q-Network agent. This design enables reinforcement learning without ground truth labels and avoids the limitations of supervised reward definitions. Because the reward mechanism does not depend on attack labels, the framework naturally mitigates the impact of class imbalance. It can also detect novel attacks through deviations from learned normal behavior.

Extensive experiments on the CIC-IDS2017 dataset demonstrate the effectiveness of the proposed framework. The AE-RL model achieves high recall (99.80%), comparable to supervised learning (99.94%), despite using only benign data during training. Moreover, the framework remains robust under severe class imbalance, maintaining consistently high recall (92.37% - 99.95%), while supervised models suffer significant degradation (99.63% - 72.78%). These results highlight the practicality of the proposed approach for real-world deployment, where labeled attack data are scarce and imbalanced.

The main contributions of this work are summarized as follows.

- An unsupervised intrusion detection framework that integrates autoencoders with reinforcement learning, eliminating the need for labeled attack data during training.
- A label-free reward mechanism derived from reconstruction error, enabling reinforcement learning without ground truth labels and avoiding the limitations of supervised reward design.
- A learning framework that mitigates the impact of class imbalance by relying solely on benign data for model training and reward generation.
- An end-to-end approach in which a Deep Q-Network agent directly processes payload image representations derived from raw network data.
- A comprehensive evaluation on the CIC-IDS2017 dataset, demonstrating effective detection performance under both balanced and imbalanced conditions.

2. Related Work

This section reviews prior work relevant to our study, focusing on learning-based approaches for network intrusion detection. The discussion is structured around three main themes, namely deep learning methods for intrusion detection, autoencoder-based anomaly detection, and reinforcement learning techniques applied to network security.

2.1 Deep Learning for Network Intrusion Detection

Deep learning has significantly advanced intrusion detection by enabling automatic feature extraction from raw network data. Vinayakumar et al. [6] showed that deep neural networks outperform traditional machine learning methods by learning hierarchical representations without manual feature engineering. However, most existing approaches rely on supervised learning under the assumption of balanced labeled datasets.

Image-based traffic representation has emerged as an effective approach for enabling deep learning models to analyze raw network data. Taheri et al. [3] converted network flows into grayscale images and achieved 99.98% accuracy on the CTU-13 dataset using DenseNet with transfer learning from ImageNet. Kotak and Elovici [4] transformed TCP payload bytes into 28 × 28 grayscale images for IoT device identification, achieving over 99% accuracy. Kaur et al. [7] extracted flow features and converted them into 9 × 9 image representations, demonstrating 99% accuracy on CIC-IDS2017. More recently, Khan et al. [8] introduced ByteStack-ID, which converts packet payload bytes into 16 × 16 grayscale images based on byte frequency distribution and applies a stacking ensemble of CNN classifiers, achieving an 81% macro F1-score on CIC-IDS2017. These studies demonstrate the effectiveness of image-based representations for intrusion-related tasks. Nevertheless, they are developed within supervised learning frameworks and assume the availability of balanced labeled attack samples.

Together, these studies highlight the effectiveness of deep learning and image-based representations for network intrusion detection. However, their reliance on supervised learning and balanced labeled datasets motivates the exploration of alternative learning paradigms that can operate effectively under limited or unlabeled data conditions.

2.2. Anomaly Detection with Autoencoders

Autoencoders have shown effectiveness for unsupervised anomaly detection by learning normal behavior patterns. Jain and Shah [9] achieved 97.50% accuracy on CIC-IDS2017 using CNN-based autoencoders trained exclusively on benign traffic. Borgioli et al. [10] proposed a 1D convolutional autoencoder trained on benign packets only, using the 99th percentile of benign reconstruction errors as the anomaly threshold and achieving 99% detection accuracy on the EDGE-IIOTSET dataset while remaining robust to dataset poisoning. More recently, Suresh et al. [11] introduced a dual-stage framework that combines an autoencoder-based anomaly detector with density-based clustering for fine-grained attack categorization, reaching 99.46% anomaly detection accuracy on CSE-CIC-IDS2018 under severe class imbalance. The reconstruction error naturally serves as an anomaly score, with normal traffic producing a low error and attacks producing a high error.

However, autoencoder-based systems typically employ static thresholds for classification, which leads to two problems. First, selecting optimal thresholds requires manual tuning and domain expertise. Second, static thresholds cannot adapt to varying network conditions or attack intensities, resulting in either high false positives or missed attacks.

2.3. Reinforcement Learning in Network Security

Reinforcement learning enables adaptive decision-making through interaction with environments. Lopez-Martin et al. [5] applied several DRL algorithms (DQN, DDQN, Policy Gradient, and Actor-Critic) to supervised intrusion detection on the NSL-KDD and AWID datasets, showing that DDQN matches or exceeds classical machine learning baselines while offering substantially faster inference. Hossain [12] proposed DQ-IDS using Deep Q-Networks with experience replay, achieving 97.18% accuracy on CICIoT2023. He et al. [13] developed TA-NIDS using Proximal Policy Optimization with anomaly scores as state space, demonstrating over 99% accuracy with strong transferability across datasets.

Despite these advances, existing RL-based systems depend on supervised reward mechanisms. They require ground truth labels during training to provide rewards (e.g., +1 for correct classification, −1 for incorrect), limiting their applicability when labeled attack data are scarce or unavailable.

3. Methodology

This section presents an unsupervised autoencoder-guided reinforcement learning framework for network intrusion detection. The task is formulated as binary classification to distinguish normal traffic from attacks. The framework addresses the limitations of traditional supervised learning approaches, which typically assume the availability of balanced labeled datasets.

An unsupervised autoencoder is trained exclusively on benign traffic to model normal network behavior and therefore does not rely on balanced training data. During reinforcement learning, the autoencoder guides a Deep Q-Network agent to differentiate between normal traffic and attacks. The framework incorporates a dynamic reward function that adaptively assigns rewards and penalties based on the agent's decisions during learning. The agent learns decision policies from reward signals derived from reconstruction error, enabling the detection of novel attacks without labeled attack samples.

The remainder of this section elaborates on the design and components of the proposed framework. We first present an overview of the system architecture, followed by the essential components, including packet payload representation, autoencoder-based normal behavior modeling, reward generation, and the reinforcement learning formulation.

3.1. Framework Overview

Figure 1 presents an overview of the proposed autoencoder-guided reinforcement learning framework for network intrusion detection. The framework consists of two main components: a convolutional autoencoder (AE) and a Deep Q-Network (DQN) agent. These components are constructed sequentially in two phases, as illustrated in the figure.

Initially, the autoencoder (AE) is trained exclusively on benign traffic to learn normal network behavior. For this purpose, only the payload portion of each network packet is extracted and converted into a 128×128 grayscale image. The resulting images are then used to train the autoencoder. Autoencoders are well suited for this task due to their unsupervised learning capability.

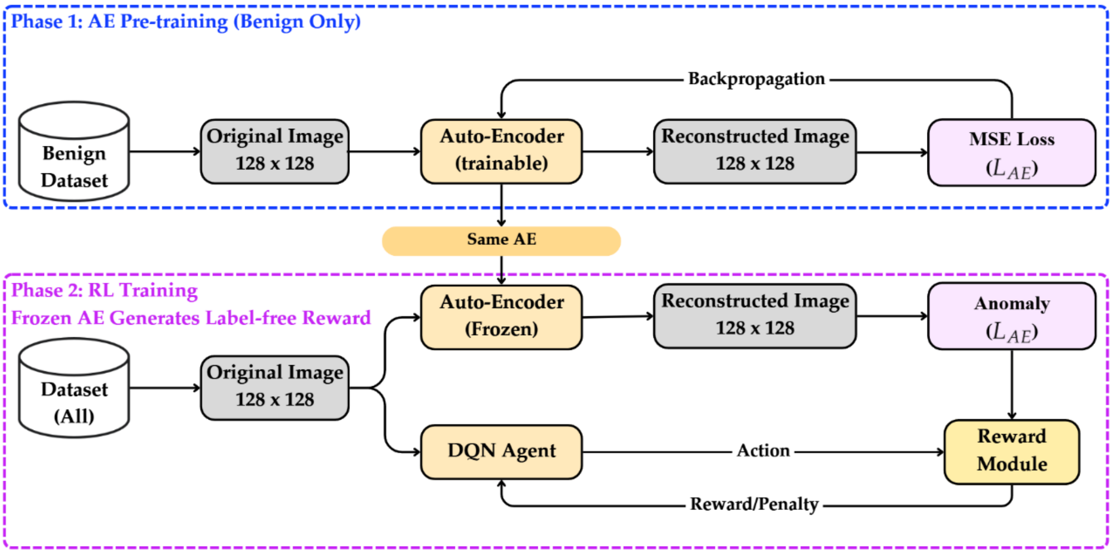

Figure 1. Autoencoder-Guided Reinforcement Learning Framework. The frozen autoencoder generates reconstruction-error based rewards, while the DQN agent learns optimal classification policies from raw payload images.

The autoencoder trained in the previous phase guides a DQN agent during the subsequent reinforcement learning phase. Each payload image is provided simultaneously to both the autoencoder and the DQN agent. The autoencoder processes the image and computes a reconstruction error. At the same time, the DQN agent processes the received image as a state input and selects an action (ALLOW or BLOCK). Our reward module then compares the selected action with the reconstruction error to determine the reward accordingly. The resulting reward is fed back to the DQN agent for policy learning.

3.2. Payload Image Representation

Network traffic is transformed into visual representations to take advantage of the spatial pattern recognition capabilities of CNNs. For each network flow, the payload bytes from all packets are extracted, concatenated, and processed into a fixed-length vector of 16,384 elements (128 × 128). Padding with zeros handles flows shorter than this length, whereas longer flows are truncated. The vector is normalized using Min-Max scaling to the [0, 255] range. It is then reshaped into a 128 × 128 grayscale image. This transformation preserves the sequential byte patterns of network payloads while enabling convolutional operations for feature extraction.

3.3. Convolutional Autoencoder

The autoencoder architecture consists of an encoder that compresses input images into a 16-dimensional latent representation and a decoder that reconstructs the original image. The encoder employs three convolutional layers with filter sizes 96, 128, and 196, using 5 × 5 and 3 × 3 kernels with stride 2 and ReLU activation. Dropout layers (rate 0.2) follow each convolution to prevent overfitting. The decoder mirrors this structure using transposed convolutions to progressively upsample from the latent space back to 128 × 128 resolution, with a final sigmoid activation to produce pixel values in [0, 1].

The autoencoder is trained exclusively on benign traffic to learn normal behavior patterns. The training objective is to minimize the reconstruction error between the input and the output. Mean Squared Error (MSE), denoted as LAE and shown in Eq. 1, is used as the loss function.

$$L_{AE} = \frac{1}{n}\sum_{i=1}^{n}(x_i - \hat{x_i})^2 \qquad (1)$$

where x_i denotes the original input image and $\hat{x_i}$ denotes the reconstructed image. After training, the autoencoder is fixed and used as an unsupervised anomaly scorer. In this role, benign traffic produces low reconstruction error, as it follows learned patterns. In contrast, attack traffic produces a higher error due to deviation from normal behavior.

3.4. Deep Q-Network Agent (DQN Agent)

Our DQN agent implements a CNN-based Q-function approximator that maps states to action values. The architecture consists of four convolutional layers followed by fully connected layers that output Q-values for each action. The following subsections describe the key components of the DQN architecture, including the state representation, action space, and reward function.

Table 1. DQN feature-extractor (CNN) architecture.

Layer	Configuration	Output
Input	grayscale payload image	1 × 128 × 128
Conv 1	32 filters, 3×3, ReLU, MaxPool 2×2	32 × 64 × 64
Conv 2	64 filters, 3×3, BatchNorm, ReLU, MaxPool 2×2	64 × 32 × 32
Conv 3	128 filters, 3×3, BatchNorm, ReLU, MaxPool 2×2	128 × 16 × 16
Conv 4	256 filters, 3×3, BatchNorm, ReLU, MaxPool 2×2	256 × 8 × 8
FC 1	Linear 512, ReLU, Dropout 0.2	512
FC 2	Linear 256, ReLU	256
FC 3	Linear 128	128 (feature dim)

3.4.1. DQN State Space

The state st is the raw 128 × 128 payload image. Unlike traditional feature-based approaches, the agent directly processes pixel intensities, enabling end-to-end learning of relevant patterns without manual feature engineering.

3.4.2. Action Space

The action space is discrete with two actions: A = {0 : ALLOW, 1 : BLOCK}. The ALLOW action permits traffic to pass. The BLOCK action flags the traffic as malicious.

3.4.3. Reward Function

Our reward function guides the agent without using ground truth labels. Reward is derived from the reconstruction error produced by the autoencoder. Recall that the autoencoder is trained only on benign traffic. It learns a representation of normal behavior. As a result, benign samples produce low reconstruction error. Anomalous traffic produces higher error due to deviation from learned patterns. The reconstruction error therefore serves as an unsupervised anomaly score.

The reward function uses this anomaly score to guide the agent. It encourages actions that align with the inferred normality of the input. This design allows reinforcement learning without labeled attack data. Our reward function takes two inputs: the agent's action {0 : ALLOW, 1 : BLOCK} and the reconstruction loss L_{AE} defined in Eq. 1. A key component of the reward formulation is the threshold τ, which separates normal and anomalous behavior. The threshold is derived from the benign training data and set to 0.01. This value was selected through empirical evaluation. As shown in the threshold sensitivity analysis in Section 5.4, τ = 0.01 provides the best balance between recall and precision, resulting in the highest F1-score. Values below the threshold indicate likely benign traffic, whereas values above the threshold indicate potential anomalies. Combining the two actions with the two ranges yields four scenarios as shown in Eq. 2. In general, correct decisions are rewarded, whereas incorrect decisions are penalized. The reward/penalty magnitude depends on the severity of deviation from normal behavior. All reward values lie within the bounded interval [-1, +1], where -1.00 represents the maximum penalty and the $tanh$-based terms asymptotically approach ±1 as L_{AE} increases.

$$R_t = \begin{cases} +0.01 & if\ a_t = 0, L_{AE} \leq \tau \\ -\, tanh(10 \cdot L_{AE}) & if\ a_t = 0, L_{AE} > \tau \\ -\,1.00 & if\ a_t = 1, L_{AE} \leq \tau \\ +\, tanh(10 \cdot L_{AE}) & if\ a_t = 1, L_{AE} > \tau \end{cases} \tag{2}$$

where R_t is the reward at time step t, a_t is the action of the agent, L_{AE} is the reconstruction loss, and τ is the fixed threshold.

When the agent correctly allows benign traffic ($a_t = 0, L_{AE} \leq \tau$), a small reward is given. This prevents bias toward always allowing traffic. When the agent incorrectly blocks benign traffic ($a_t = 1, L_{AE} \leq \tau$), a false alarm occurs. In this case, a fixed penalty of -1.00 is applied. This reflects clear misclassifications. When the agent incorrectly allows anomalous traffic ($a_t = 0, L_{AE} > \tau$), a penalty is applied. The penalty increases with reconstruction error. This emphasizes the cost of missing attacks. When the agent correctly blocks anomalous traffic($a_t = 1, L_{AE} > \tau$), a reward is given. The reward also increases with reconstruction error. This encourages the detection of strongly anomalous samples.

The $tanh$ function is used to bound reward values within $[-1, 1]$. It provides smooth gradients and stable learning. The scaling factor controls sensitivity to reconstruction error.

The structure of our reward function is asymmetric. Correct attack detection is rewarded more strongly than correct benign classification ($+tanh(10 \cdot L_{AE})$ vs. $+0.01$), biasing the agent toward attack detection. This reflects the priorities of security-critical applications.

Unlike supervised approaches, reward in our unsupervised autoencoder-guided reinforcement learning framework is not derived from class labels. It is inferred from the structure of normal data. This allows the framework to operate under label scarcity and class imbalance.

3.4.4. Training Algorithm

The DQN agent is trained using experience replay and a target network following Mnih et al. [14]. At each time step, the agent observes a state s_t, selects an action at, receives a reward r_t, and transitions to the next state s_{t+1} . Each transition (s_t, a_t, r_t, s_{t+1}) is stored in a replay buffer with a capacity of 200,000 samples.

During training, mini-batches are sampled randomly from the replay buffer. This process reduces temporal correlation between consecutive samples and improves training stability. The Q-network is updated by minimizing the loss defined in Eq. 3.

$$L(\theta) = \mathbb{E}_{(\mathbb{s},\mathbb{a},\mathbb{r},\mathbb{s}')\sim\mathbb{D}}\left[\left(y - Q(s,a;\theta)\right)^2\right] \tag{3}$$

where θ denotes the parameters of the Q-network and y is the target value defined as

$$y = r + \gamma \max_{a'} Q(s', a'; \theta^-)$$

A separate target network with parameters θ^- is used to stabilize training. The target network is updated periodically. The discount factor γ is set to 0.99 to balance immediate and future rewards.

Action selection follows an ϵ-greedy exploration strategy. The parameter ϵ controls the probability of selecting a random action. Training begins with $\epsilon = 1.0$ to encourage exploration. The value gradually decays to $\epsilon = 0.05$ during training. The Q-network is optimized using the Adam optimizer. The learning rate α is set to 0.0001.

All models were trained on an RTX 4070 Ti SUPER (16 GB) GPU. The autoencoder was trained for 30 epochs (batch size 32, Adam, learning rate 0.0001, MSE loss, early stopping patience 5), taking approximately 1.5 hours. The DQN agent was trained for up to 1,000,000 timesteps (replay buffer 200,000, batch size 32, discount factor 0.99, epsilon annealed 1.0–0.05, Adam, learning rate 0.0001), taking approximately 6.2 hours. The mean evaluation reward stabilizes within the first 200,000 timesteps, well before the configured budget, and the best-performing policy by this metric was checkpointed.

4. Experimental Setup

This section describes the experimental design used to evaluate the proposed autoencoderguided reinforcement learning framework. The experiments assess the effectiveness of the framework for intrusion detection under both balanced and imbalanced conditions. The proposed AE-RL approach is also compared with supervised DQN counterparts trained using labeled attack data. The evaluation focuses on detection performance, robustness to class imbalance, and the ability to operate without labeled attack samples. The following subsections describe the dataset, pre-processing pipeline, partitioning strategy, and evaluation metrics.

4.1. Dataset and Data Pre-processing

The proposed framework is evaluated on the CIC-IDS2017 dataset [15], which contains realistic network traffic captured over five days in July 2017. The traffic is provided as raw PCAP files.
Table 2 indicates that the CIC-IDS2017 dataset contains approximately 55,920,130 packets. Among these, 51,810,267 packets correspond to benign traffic. The remaining 4,109,863 packets correspond to malicious traffic across 14 attack categories.

These files are processed to construct network flows using 5-tuple identification, namely the source IP address, the destination IP address, the source port, the destination port, and the protocol. For each flow, only the payload bytes are extracted, while the headers of the packet are discarded. The extracted payloads are then converted into grayscale images for the framework input. This representation enables both the autoencoder and the DQN agent to process the same raw payload input during learning. As a result, the dataset contains 1.139 million flow records, including both benign and malicious traffic across the 14 attack categories. Due to the requirement for payload-based image representation, only attack types with sufficient payload content are selected. These include SSH-Patator, DoS Slowloris, DoS Slowhttptest, DoS Hulk, DoS GoldenEye, and DDoS. Attacks with sparse payload data are excluded.

Table 2 shows the complete distribution of both raw packets and processed flows in the CICIDS2017 dataset. Due to payload-based image representation requirements, we focus on six attack types that provide sufficient discriminative payload content. The table also highlights severe class imbalance, which reflects realistic network traffic conditions. Specifically, benign traffic comprises 895,638 flows, whereas several attack categories contain fewer than 5,000 samples.

Table 2. Complete CIC-IDS2017 dataset distribution.

Traffic Type	Packets	Flows
Benign	51,810,267	895,638
Attack Types Used in This Study		
DoS Hulk	2,191,807	14,108
DoS GoldenEye	99,003	7,458
DoS Slowhttptest	36,874	4,216
DoS Slowloris	46,327	3,873
DDoS	989,426	45,392
Traffic Type	**Packets**	**Flows**
SSH-Patator	163,095	2,979
Other Attack Types (Excluded)		
PortScan	321,442	158,676
FTP-Patator	105,618	3,991
Bot	12,853	1,228
Web Attack – Brute Force	27,771	1,363
Web Attack – XSS	7,483	631
Infiltration	59,754	6
Heartbleed	49,290	1
Web Attack – SQL Injection	120	12
Total (All Types)	55,920,130	1,139,572
Used in Study (Benign + Selected Attacks)	55,336,799	973,664

4.2. Dataset Partitioning Strategy

The dataset is partitioned to support three objectives: normal behavior learning for the autoencoder, policy learning for reinforcement learning, and fair comparison with supervised baselines. To ensure unbiased evaluation, the test set is balanced with an equal number of benign and attack samples. Table 3 summarizes the partitioning strategy.

Attack traffic is divided into 70% for the RL training environment, 10% for validation, and 20% for testing, resulting in 15,605 test samples. The benign test samples are then selected to match this count. They are drawn equally from all five capture days, yielding 15,605 samples in total, or approximately 3,121 per day.

The remaining benign traffic is divided into 45% for autoencoder training (AE-Train), 45% for the RL training environment (RL-Train), and 10% for validation. This strategy ensures that the autoencoder learns exclusively from normal behavior while maintaining a balanced evaluation across both classes. For the class imbalance experiments described in Section 5.3, a subset of 318,586 benign flows from RL-Train is used with varying attack sample counts.

Table 3. Dataset partitioning strategy.

Traffic Type	AE-Train	RL-Train	Validation	Test
Benign	45% (396,015)	45% (396,015)	10% (88,003)	– (15,605)
Attack	–	70% (54,177)	10% (7,740)	20% (15,605)

Table 3 summarizes how the dataset is partitioned in our experiments. The AE-Train set contains 396,015 benign flows for learning normal behavior patterns. The RL-Train environment combines 396,015 benign flows with 54,177 attack flows. For class imbalance experiments, a subset of 318,586 benign flows from RL-Train is used with varying attack sample counts.

4.3. Evaluation Metrics

The proposed framework is evaluated using standard classification metrics, including Accuracy, Precision, Recall, and F1-score. Among these, Recall is treated as the primary metric because the framework is designed for security-critical environments where missing attacks is more costly than raising false alarms.

5. Results and Discussion

The proposed unsupervised AE-RL framework is evaluated on a binary intrusion detection task (Benign vs Attack). The experiments are designed to assess two aspects of the framework. The first is the overall intrusion detection performance compared with supervised DQN counterparts. The second is the robustness of the framework under severe class imbalance, which reflects realistic network traffic conditions.

5.1. Performance Comparison with Supervised Learning

Table 4 presents the performance comparison on the balanced test set. The supervised baseline uses imbalanced training data (5.8:1 ratio) reflecting realistic scenarios.

Table 4. Binary classification performance comparison.

Metric	AE-only	AE-RL	Supervised
Accuracy	91.51%	91.78%	99.30%
Precision	85.52%	86.02%	98.67%
Recall	99.95%	99.80%	99.94%
F1-Score	92.17%	92.40%	99.30%
Training Labels	Benign Only	Benign Only	Benign + Attack

The experimental results indicate that supervised models slightly outperform that trained through our proposed AE-RL framework. This observation is consistent with expectations. Supervised learning benefits from access to both benign and attack labels during training. Such labeled data enables the model to learn explicit decision boundaries between classes. In contrast, our proposed framework operates without attack labels and relies on deviations from normal behavior. This difference naturally leads to a performance gap in favor of supervised approaches.

Despite this expected performance gap, the proposed framework demonstrates several important advantages under realistic deployment conditions. The model trained through the AE-RL framework achieves 99.80% recall, detecting attacks nearly as effectively as supervised learning (99.94%) without labeled attack data. This result highlights the ability of the framework to maintain strong attack detection performance under label scarcity.

A trade-off appears in precision (86.02% vs. 98.67%). The reconstruction-error-based reward design induces conservative blocking behavior, yielding more false positives (14% vs. 1.3%). The lower precision reflects the security-oriented design priority of maximizing attack detection over minimizing false alarms. As a result, the agent tends to block suspicious traffic aggressively.

5.2. Contribution of the Reinforcement Learning Component

To isolate the contribution of the reinforcement learning component, we evaluate the autoencoder as a standalone detector (AE-only). A flow is classified as an attack when its reconstruction error exceeds the same threshold τ used by the RL reward function. As shown in Table 4, the AE-only detector achieves 91.51% accuracy, 85.52% precision, 99.95% recall, and 92.17% F1-score. These results are comparable to those of the AE-RL framework.

The close performance is expected because both approaches rely on the same anomaly information derived from reconstruction error. The autoencoder therefore serves as the primary source of attack discrimination. Nevertheless, AE-RL achieves slightly higher accuracy, precision, and F1-score while maintaining comparable recall. This suggests that the RL agent learns a more effective decision policy than fixed thresholding alone.

These findings clarify the role of reinforcement learning in the proposed framework. The contribution of the RL component is not to improve anomaly detection itself, but to learn a decision policy from reconstruction-error-based rewards without attack labels. More importantly, the RL formulation provides a flexible decision framework that can integrate anomaly signals from multiple autoencoders or heterogeneous detectors. This capability is difficult to achieve with a fixed threshold-based approach and provides a foundation for future adaptive intrusion detection systems.

5.3. Impact of Class Imbalance on Supervised Learning

To evaluate the robustness of the proposed AE-RL framework under realistic data scarcity conditions, we investigate its performance under varying class imbalance ratios and compare the results with supervised learning counterparts (CNN). Different imbalance conditions are created by keeping the benign sample count fixed at 396,015 while progressively reducing the number of attack samples from 6,000 to 4,200.

Table 5. Supervised CNN performance under varying class imbalance.

Attack Samples	Imbalance Ratio	Accuracy	Recall	F1-Score
6,000	53:1	99.16%	99.63%	99.15%
5,400	59:1	89.38%	74.91%	85.26%
4,800	66:1	88.43%	77.83%	88.30%
4,200	76:1	86.00%	72.78%	85.75%

Table 6. AE-RL framework performance under varying class imbalance.

Attack Samples	Imbalance Ratio	Accuracy	Recall	F1-Score
6,000	53:1	91.12%	98.94%	91.77%
5,400	59:1	89.03%	95.21%	89.67%
4,800	66:1	90.75%	99.95%	91.53%
4,200	76:1	88.84%	92.37%	89.22%

Tables 5 and 6 compare the impact of class imbalance on both approaches. The supervised CNN shows significant performance degradation as imbalance increases. Its recall drops from 99.63 % at a 53:1 ratio to 72.78 % at a 76:1 ratio, a decline of 26.85 percentage points. This result indicates strong dependence on labeled attack availability during supervised training.

In contrast, the AE-RL framework maintains consistently high recall across all imbalance conditions. The recall ranges from 92.37 % to 99.95 %. Even at the most extreme imbalance (76:1), AE-RL achieves 92.37 % recall. This result exceeds the supervised CNN by 19.59 percentage points. This stability suggests that the proposed reward mechanism remains effective even when attack samples become increasingly scarce.

This robustness arises from the framework's independence from labeled attack data. The autoencoder is trained only on benign traffic. Its reward signals are therefore unaffected by the availability of attack samples. These results demonstrate that the AE-RL framework mitigates the brittleness of supervised approaches under realistic data scarcity conditions.

5.4. Threshold Sensitivity Analysis

The threshold τ is the only parameter converting a reconstruction error into an ALLOW/BLOCK decision, so we assess how strongly the results depend on it. We evaluate the AE-only detector on the balanced test set while sweeping τ across a range of evenly spaced values, from 0 to 0.025 in steps of 0.005 (Table 7).

Table 7. AE-only detection performance versus the anomaly threshold τ.

T	Precision	Recall	F1
0.000	0.5000	1.0000	0.6667
0.005	0.8295	0.9995	0.9066
0.010	0.8552	0.9995	0.9217
0.015	0.8449	0.7246	0.7801
0.020	0.6984	0.2260	0.3415
0.025	0.0068	0.0005	0.0010

At τ= 0, every sample is classified as an attack. As a result, recall reaches 100%, while precision is only 50%. Increasing the threshold improves precision with little impact on recall. The best performance is achieved at $\tau = 0.01$, yielding 85.5% precision, 99.9% recall, and an F1-score of 0.922.
Performance remains stable for thresholds between 0.005 and 0.010. Within this range, the F1-score stays above 0.90. Beyond $\tau = 0.01$, recall drops rapidly. It decreases to 72.5% at $\tau = 0.015$ and 22.6% at $\tau = 0.020$. At $\tau = 0.025$, detection performance is almost completely lost.

This behavior can be explained by the reconstruction-error distributions. Attack samples are concentrated within a relatively narrow error range. In contrast, benign samples exhibit a longer upper tail. Increasing the threshold beyond the attack region suppresses both true positives and false positives. As a result, recall deteriorates rapidly.

Based on these results, $\tau = 0.01$ is selected for all experiments. This value provides the highest F1-score while preserving near-perfect recall. The detector is robust to small threshold variations around this value. However, performance becomes highly sensitive when the threshold is increased further. This observation motivates the adaptive-threshold direction discussed in Section 5.5.

5.5. Discussion

The results demonstrate the practical feasibility of unsupervised AE-RL intrusion detection framework. Supervised learning achieves higher accuracy (99.30% vs 91.78%) and precision (98.67% vs 86.02%). However, the recall gap is only 0.14% (99.80% vs 99.94%). Recall reflects the ability to detect attacks and minimize false negatives, which is critical in security applications. This small gap therefore supports the use of the proposed unsupervised framework in settings where labeled attack data are scarce.

The framework can potentially detect novel attacks by identifying deviations from normal behavior learned during unsupervised training. More importantly, the proposed reward mechanism operates without attack labels. This design supports stable learning under label scarcity and class imbalance.

However, several limitations remain. The framework depends on the quality of benign training data. Poor-quality samples may lead to inaccurate modeling of normal behavior. This can propagate unreliable reward signals to the DQN agent. The framework also requires sufficient payload content for effective representation. Payloads with limited information may reduce the quality of learned patterns. In addition, the framework exhibits a higher false positive rate (14%). This behavior reflects its conservative attack detection strategy, which prioritizes recall over specificity.

The lower precision of the proposed framework (86.02% vs 98.67%) indicates a higher number of false alarms. On the balanced test set, 14% of flows flagged as attacks are actually benign. This behavior is a direct consequence of the threshold selection. The threshold is chosen to preserve near-perfect recall, which is the primary objective in security applications. As a result, some benign flows with unusually high reconstruction errors are also classified as attacks. This effect originates from the long upper tail of the benign error distribution. Future work may reduce false alarms through adaptive threshold estimation or an additional verification stage.

The comparison between AE-only and AE-RL provides further insight into the role of reinforcement learning. The close performance of the two approaches is expected because both rely on the same anomaly information derived from reconstruction error. The RL agent does not replace the anomaly detection capability of the autoencoder. Instead, it learns a decision policy from label-free rewards. More importantly, the RL formulation provides a flexible decision framework that can integrate anomaly signals from multiple autoencoders or heterogeneous detectors. This capability extends beyond the limitations of a fixed threshold-based classifier and provides a foundation for future adaptive intrusion detection systems.

6. Conclusions

This paper presented an unsupervised autoencoder-guided reinforcement learning framework for network intrusion detection that eliminates labeled attack data requirements. The framework achieves 99.80% recall on CIC-IDS2017, demonstrating near-parity with supervised baselines (99.94%) while training exclusively on benign samples. The primary contribution lies in using reconstruction error-based rewards to guide Deep Q-Network policy learning without attack labels. Evaluated on six attack types, the approach trades precision (86.02% vs 98.67%) for practical deployment feasibility where labeled attacks are scarce. The minimal recall gap (0.14%) validates unsupervised intrusion detection for security-critical applications. Future work includes reward function refinement to reduce false positives and extension to multi-class classification.

References

[1] IBM Security. Cost of a data breach report 2024. Technical report, IBM Corporation and Ponemon Institute, Cambridge, MA, July 2024.

[2] Federal Bureau of Investigation. 2024 internet crime report. Technical report, Internet Crime Complaint Center (IC3),Washington, DC, 2024.

[3] Shayan Taheri, Milad Salem, and Jiann-Shiun Yuan. Leveraging image representation of network traffic data and transfer learning in botnet detection. Big Data and Cognitive Computing, 2(4):37, 2018. doi: 10.3390/bdcc2040037.

[4] J. Kotak and Y. Elovici. IoT device identification using deep learning on network traffic. IEEE Transactions on Information Forensics and Security, 17:1725–1738, 2022.

[5] M. Lopez-Martin, B. Carro, and A. Sanchez-Esguevillas. Application of deep reinforcement learning to intrusion detection for supervised problems. Expert Systems with Applications, 141: 112963, 2020. doi: 10.1016/j.eswa.2019.112963.

[6] R. Vinayakumar, M. Alazab, K. P. Soman, P. Poornachandran, A. Al-Nemrat, and S. Venkatraman. Deep learning approach for intelligent intrusion detection system. IEEE Access, 7:41525-41550, 2019.

[7] R. Kaur, D. Singh, and P. Kumar. Deep image learning for intrusion detection: A novel approach using convolutional neural networks. In Proc. Int. Conf. Computing, Communication and Security, pages 1–6, 2020.

[8] Irfan Khan, Yasir Ali Farrukh, and Syed Wali. ByteStack-ID: Integrated stacked model leveraging payload byte frequency for grayscale image-based network intrusion detection. In arXiv preprint arXiv:2310.09298, 2024.

[9] M. Jain and A. Shah. Anomaly detection using convolutional neural networks (CNN). ESP International Journal of Advancements in Computational Technology, 2(3):12–22, 2024. doi: 10.56472/25838628/IJACT-V2I3P102.

[10] Niccolo Borgioli, Federico Aromolo, Linh Thi Xuan Phan, and Giorgio Buttazzo. A convolutional autoencoder architecture for robust network intrusion detection in embedded systems. Journal of Systems Architecture, 156:103283, 2024. doi: 10.1016/j.sysarc.2024.103283.

[11] K. S. Suresh, Thenmozhi Elumalai, Radhakrishnan Rajamani, Anubhav Kumar, Balamurugan Balusamy, Sumendra Yogarayan, and Kaliyaperumal Prabu. An unsupervised cloud-centric intrusion diagnosis framework using autoencoder and density-based learning. Future Internet, 18(1):54, 2026. doi: 10.3390/fi18010054.

[12] Md. Alamgir Hossain. Deep Q-learning intrusion detection system (DQ-IDS): A novel reinforcement learning approach for adaptive and self-learning cybersecurity. ICT Express, 11:875–880, 2025. doi: 10.1016/j.icte.2025.05.007.

[13] Mingshu He, Xiaojuan Wang, Peng Wei, Liu Yang, Yinglei Teng, and Renjian Lyu. Reinforcement learning meets network intrusion detection: A transferable and adaptable framework for anomaly behavior identification. IEEE Transactions on Network and Service Management, 21(2): 2477–2492, 2024. doi: 10.1109/TNSM.2024.3352586.

[14] V. Mnih et al. Human-level control through deep reinforcement learning. Nature, 518(7540): 529–533, 2015.

[15] I. Sharafaldin, A. H. Lashkari, and A. A. Ghorbani. Toward generating a new intrusion detection dataset and intrusion traffic characterization. In Proc. 4th Int. Conf. Information Systems Security and Privacy (ICISSP), pages 108–116, 2018.

[16] Check Point Software Technologies. Thailand cyber threat landscape report: CPX APAC 2025. Cited in Bangkok Post, February 2025.

A Multi-Level Evaluation Framework for Explainable AI: The Triangle Graph Approach

Peemapat Podsoonthorn*, Wanida Putthividhya, Thapana Boonchoo

Department of Computer Science, Faculty of Science and Technology, Thammasat University (Rangsit Campus), Pathumthani 12121, Thailand
*Correspondence: peemapat.pods@dome.tu.ac.th

Abstract

While machine learning performance is commonly evaluated using standard metrics such as accuracy and F1-score, transitioning to Explainable AI (XAI) introduces a steep learning curve due to the fragmented landscape of explanation methods and evaluation strategies. To address this challenge, we propose a unified multi-level evaluation framework aligned with the standard machine learning pipeline. The framework decomposes model behavior into three levels: Input, Internal, and Output, each associated with appropriate explanation and evaluation mechanisms. Quantitative results from these levels are integrated into a novel Triangle Graph visualization that enables intuitive assessment of holistic model reliability. We further introduce the Holistic Reliability Score (HRS), a scalar metric derived from the normalized triangle area, together with a weighted formulation for domain-specific priorities. The framework is evaluated across text (IMDb, ISOT), tabular (UCI Adult), and image (CIFAR-10) datasets using BERT, Bi-LSTM, XGBoost, MLP, and ResNet-20 architectures. Results show that single metrics such as F1, Input-Level NAOPC, or Internal-Level NAOPC lead to different model-selection conclusions, whereas the proposed HRS integrates these signals into a unified reliability assessment. The Triangle Graph further reveals trade-offs between predictive performance and multi-level explanation faithfulness that remain hidden under standard evaluation.

Keywords: Explainable AI, Faithfulness Evaluation, NAOPC, Triangle Graph, Holistic Reliability Score

1. Introduction

The rapid advancement of machine learning, particularly deep neural networks, has significantly improved predictive performance across diverse application domains. Despite these successes, increasing model complexity often comes at the expense of transparency. Many high-performing systems operate as "black-box" models whose internal decision-making processes are difficult for practitioners to interpret.

Explainable Artificial Intelligence (XAI) has emerged as an important research direction to address this challenge. XAI aims to improve transparency, increase user trust, support regulatory compliance, and facilitate model debugging [1,2]. Existing approaches generally include model-agnostic methods that explain predictions externally and model-specific methods that exploit architectural information directly. These methods provide complementary perspectives for understanding model behavior.

As XAI research has matured, generating explanations alone is no longer sufficient. Explanations must also be evaluated for quality and reliability. This has led to the development of quantitative evaluation properties such as Faithfulness and Robustness [3,4]. However, XAI evaluation introduces its own challenges. Different explanation techniques may produce conflicting feature attributions, while different evaluation metrics can yield inconsistent interpretations [5,6]. Consequently, transitioning from traditional model evaluation to XAI evaluation often presents a steep learning curve for practitioners [7].

Existing frameworks partially address these issues by providing taxonomies, toolkits, or auditing guidelines. However, they often focus on isolated aspects of explanation generation or evaluation.

Practitioners still lack a unified approach that simultaneously considers predictive performance and explanation quality across different levels of model analysis.
To address this limitation, this paper proposes a unified multi-level evaluation framework aligned with the standard machine learning pipeline. The framework organizes model behavior into three complementary levels: Input, Internal, and Output. Each level combines qualitative explanation methods with quantitative evaluation metrics to provide structured analysis from different perspectives.

To unify these evaluation results, we introduce the Triangle Graph, a tri-axial visualization that provides a holistic representation of predictive performance and explainability. We further introduce the Holistic Reliability Score (HRS), a scalar metric derived from the normalized triangle area together with a weighted formulation for domain-specific priorities.

The proposed framework is evaluated across text, tabular, and image tasks using multiple datasets and architectures. Experimental results demonstrate that the framework reveals trade-offs between predictive performance and explainability that remain hidden under conventional evaluation approaches.

2. Related Work

Model transparency challenges arise at different stages of machine learning systems. Understanding model behavior therefore requires analysis from multiple perspectives rather than relying on a single explanation stage. Following the structure of the proposed framework, related work is organized into qualitative explanation methods, quantitative evaluation metrics, and existing XAI evaluation frameworks.

2.1. Qualitative Explanation Methods

Qualitative explanation methods provide human-interpretable descriptions of model behavior by identifying influential features and revealing model reasoning patterns.
Input Level. Model-agnostic approaches explain predictions without requiring access to model internals. Representative methods include SHAP [8], which estimates feature importance using Shapley values, and LIME [9], which approximates local decision boundaries using interpretable surrogate models.

Internal Level. Internal explanations rely on model-specific methods that access architectural information directly. Representative techniques include Integrated Gradients (IG) [10], attention-based attribution for transformers [11,12], Grad-CAM [13] for CNNs, and SHAP TreeExplainer [8] for tree-based models. Output Level. Interpretation at the Output Level focuses on model predictions and confidence scores, which provide the most direct representation of model behavior.

2.2. Quantitative Evaluation Metrics

While qualitative explanations provide descriptive information, quantitative metrics assess their reliability. Common evaluation properties include Faithfulness and Robustness [3,4]. Faithfulness measures whether important features genuinely influence predictions and is commonly evaluated through perturbation-based metrics such as Comprehensiveness (COMP), Sufficiency (SUFF), and AOPC [14]. More recently, AOPC has been extended through normalization into Normalized AOPC (NAOPC), improving comparability across settings [15]. Predictive performance is typically evaluated using standard metrics including Accuracy, Precision, Recall, and F1-score.

2.3. Existing Frameworks and Research Gap

Several studies have proposed structured approaches for XAI evaluation. Co-12 [16] organizes evaluation properties into a comprehensive taxonomy, AIX360 [17] provides a toolkit for explanation selection, and HEXP [18] offers structured qualitative auditing.

Although these frameworks provide valuable capabilities, they primarily focus on isolated aspects of explanation generation or evaluation. A common limitation is the lack of a unified mechanism that jointly considers predictive performance and explanation quality across multiple analysis levels.

Consequently, practitioners still lack a straightforward way to assess overall model reliability. This limitation motivates the need for a unified multi-level evaluation framework.

3. Methodology

To address the fragmented nature of XAI evaluation, we propose a unified multi-level framework aligned with the standard machine learning pipeline. Unlike existing approaches that evaluate predictive performance and explanation quality independently, the proposed framework integrates these dimensions into a unified representation through the Triangle Graph and a scalar Holistic Reliability Score (HRS).

The framework organizes model analysis into three complementary evaluation levels: Input (Feature Influence), Internal (Model Thinking), and Output (Model Prediction), as illustrated in Figure 1. Each level captures a different aspect of model behavior and consists of two stages: qualitative explanation generation and quantitative evaluation. Although this study instantiates the framework with SHAP, architecture-specific attribution methods, NAOPC [15], and F1-score, practitioners may substitute explanation methods or metrics that better match their task, model type, or deployment requirements.

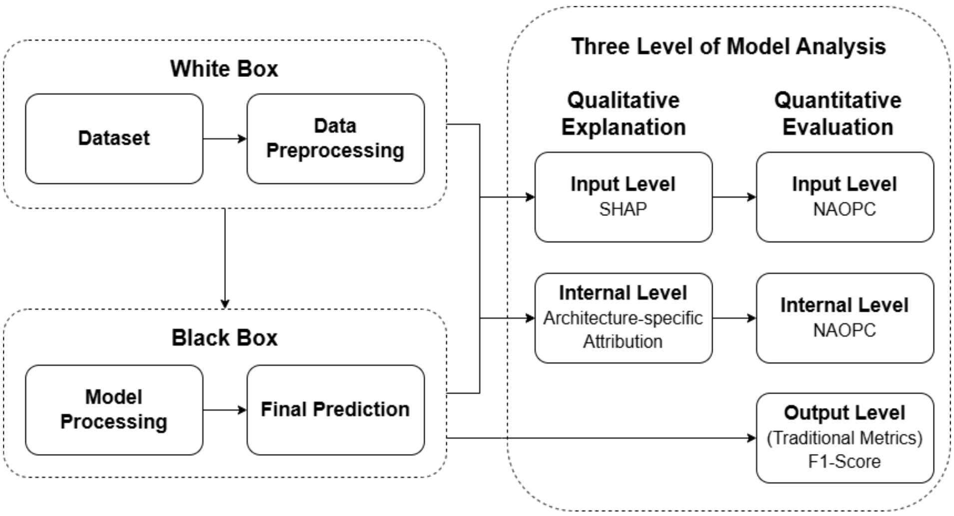

Figure 1. Overview of the proposed multi-level evaluation framework. The standard ML pipeline maps onto three evaluation levels, each associated with corresponding qualitative explanation methods and quantitative metrics.

3.1. Qualitative Explanation Methods

The first stage of the framework focuses on generating qualitative explanations to explain model behavior. These explanations identify influential features and reveal internal processing patterns that contribute to model decisions. Because different evaluation levels capture different aspects of model behavior, different explanation strategies are employed accordingly. Input Level. SHAP [8] is adopted as the model-agnostic explanation method because it can be applied across text, tabular, and image models while providing Shapley-value-based attributions with desirable consistency properties. SHAP assigns each feature a Shapley value that quantifies its contribution to the prediction, providing theoretically grounded feature attribution. Internal Level. Internal representations vary across architectures. Therefore, the framework employs architecture-specific explanation methods summarized in Table 1. These methods are selected to directly exploit each model's computational structure. Output Level. At this level, the model prediction itself serves as the qualitative representation of model behavior. Additional explanation techniques are therefore less emphasized.

Table 1. Architecture-specific internal-level explanation methods.

Architecture	Method	Rationale
Transformer (BERT)	Gradient-weighted Attention Attribution [11,12]	Combines attention scores with gradient information to generate token-level explanations reflecting contextual dependencies.
Recurrent (Bi-LSTM)	Gradient x Input [10]	Computes feature contribution directly from gradients at the current embedding representation.
Tree-based (XGBoost)	SHAP TreeExplainer [8]	Computes exact Shapley values by exploiting the internal tree structure.
Feedforward (MLP)	Integrated Gradients [10]	Attributes prediction changes to input features through gradients accumulated from a baseline to the observed input.
Convolutional (CNN)	Grad-CAM [13]	Produces spatial attribution maps using gradient-weighted activation maps.

3.2. Quantitative Evaluation Metrics

Following qualitative explanation generation, the second stage focuses on quantitative evaluation. While qualitative explanations provide descriptive information, they do not indicate whether the generated explanations faithfully represent model behavior. Quantitative evaluation is therefore required to assess explanation quality and predictive performance.

Different evaluation levels require different quantitative metrics. The Input and Internal Levels evaluate explanation Faithfulness, whereas the Output Level evaluates predictive performance. Other metrics can be used within the same framework when they are more suitable for a particular application.

3.2.1. NAOPC: Quantifying Input and Internal Level Faithfulness

The Input and Internal Levels assess explanation quality using Faithfulness. The underlying intuition is that if an explanation correctly identifies influential features, progressively removing these features should substantially reduce model confidence.

The framework employs the Normalized Area Over the Perturbation Curve (NAOPC) [15] to quantify this effect. SHAP produces the Input score s_1, while architecture-specific explanations produce the Internal score s_2. Given an input sample x with N ranked features and confidence function f, AOPC [14] is defined as:

$$AOPC = \frac{1}{N} \Sigma_{k=1}^{N} [f(x) - f(x^{(k)})] \quad (1)$$

where $x^{(k)}$ represents the perturbed input after masking the top-k ranked features.

Because AOPC [14] values may vary across datasets and architectures, normalization is applied:

$$NAOPC = \frac{AOPC - AOPC_{min}}{AOPC_{max} - AOPC_{min}}, \in [0,1] \quad (2)$$

where $AOPC_{max}$ and $AOPC_{min}$ denote upper and lower bounds estimated through beam search. Larger values indicate stronger agreement between explanations and actual model behavior.

3.2.2. F1-Score: Quantifying Output-Level Performance

Unlike the Input and Internal Levels, the Output Level evaluates predictive performance rather than explanation quality. We use positive-class binary F1 for IMDb, ISOT, and UCI Adult, and macro-averaged F1 for the multiclass CIFAR-10 dataset.

For each class, F1 is the harmonic mean of precision and recall; macro-averaged F1 is computed as:

$$F1_{macro} = \frac{1}{C} \sum_{c=1}^{C} \frac{2P_c R_c}{P_c + R_c} \tag{3}$$

where Pc and Rc are the precision and recall for class c. For the binary datasets, s3 is the positive-class F1 term shown inside the summation; for CIFAR-10, s3 is the macro-average in Equation 3.

3.2.3. Holistic Reliability Score and Triangle Integration

The three evaluation levels provide complementary perspectives on model reliability. Individually, each score captures only one aspect of model behavior. Interpreting these scores independently can make overall assessment difficult.

To provide a unified view, the proposed framework integrates quantitative results from all evaluation levels. Specifically, s_1 represents Input-Level Faithfulness, s_2 represents Internal-Level Faithfulness, and s_3 represents predictive performance, as illustrated in Figure 2.

These scores are projected onto a tri-axial radar chart with axes separated by 120 degrees. The corresponding vertices are:

$$P_1 = (0, s_1),\ P_2 = (-(\tfrac{\sqrt{3}}{2})s_2, -(\tfrac{1}{2})s_2),\ P_3 = ((\tfrac{\sqrt{3}}{2})s_3, -(\tfrac{1}{2})s_3)$$

Applying the shoelace formula to these vertices gives the triangle area [19]:

$$A = \frac{\sqrt{3}}{4}(s_1 s_2 + s_2 s_3 + s_3 s_1) \tag{4}$$

$$A_{max} = \frac{3\sqrt{3}}{4} \tag{5}$$

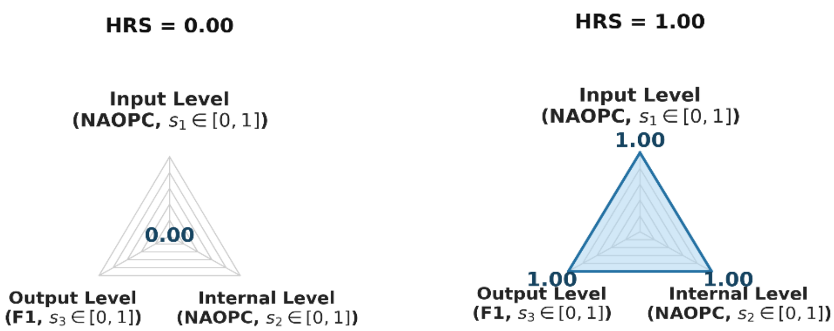

Figure 2. Reference Triangle Graphs showing the minimum and maximum cases for the three radial axes used in HRS computation: Input-Level NAOPC (s_1), Internal-Level NAOPC (s_2), and Output-Level F1 (s_3), each scaled from 0 to 1.

The Holistic Reliability Score (HRS) normalizes this area by its maximum value:

$$HRS = \frac{A}{A_{max}} = \frac{s_1 s_2 + s_2 s_3 + s_3 s_1}{3} \quad (6)$$

HRS ranges from 0 to 1 and summarizes normalized triangle area across the Input, Internal, and Output Levels. It does not independently measure symmetry: triangle shape indicates how evenly the scores are distributed, whereas HRS represents their combined area.

To support application-specific priorities, a weighted extension is introduced:

$$HRS_w = \frac{w_1 w_2\, s_1 s_2 + w_2 w_3\, s_2 s_3 + w_3 w_1\, s_3 s_1}{w_1 w_2 + w_2 w_3 + w_3 w_1},\ w_i \geq 0,\ \Sigma_{i=1}^{3} w_i = 1 \quad (7)$$

where w_1, w_2, w_3 are user-defined weights for the Input, Internal, and Output Levels. This preserves the geometric interpretation while allowing application-specific priorities.

3.2.4. Weight Selection

The default setting uses equal weights, $w_1=w_2=w_3=1/3$, when no domain priority is specified. All weights are non-negative and normalized so that $w_1+w_2+w_3=1$. In this experiment, the domain-specific weights for (Input, Internal, Output) are IMDb (0.40,0.20,0.40), ISOT (0.50,0.10,0.40), UCI Adult (0.30,0.30,0.40), and CIFAR-10 (0.20,0.50,0.30). These weights should be selected before evaluation according to deployment context. Automatic weight selection from data characteristics or stakeholder preferences remains future work.

4. Experimental Setup

To evaluate the generalizability of the proposed framework, experiments are conducted across three modalities: text, tabular, and image. This multi-modal setting demonstrates that the framework is not tied to a specific domain and can expose reliability trade-offs across different architectures and data types.

4.1. Datasets and Architectures

Experiments are performed on four benchmark datasets spanning multiple tasks and modalities. Text Modality. IMDb Reviews [20] contains 50,000 movie reviews for binary sentiment classification, while ISOT Fake News [21] contains 44,898 articles for binary fake-news detection. Two text architectures are evaluated: Bi-LSTM [22] and fine-tuned BERT-base [23]. Tabular Modality. The UCI Adult dataset [24] contains 48,842 records for binary income prediction (≤50K vs. >50K). Two architectures are evaluated: XGBoost [25] and a two-hidden-layer MLP [26]. Standard preprocessing including categorical encoding, missing-value handling, and feature normalization is applied where appropriate. Image Modality. CIFAR-10 [27] contains 60,000 images across ten classes. To reduce computational cost, balanced subsets of 5,000 training and 1,000 testing images are used. ResNet-20 [28] is adopted as the image classification architecture.

4.2. Framework Application

The proposed framework is applied across all experimental settings using the same three-level structure. Qualitative explanations are first generated using architecture-appropriate methods, followed by quantitative evaluation using corresponding metrics.

4.2.1. Qualitative Explanation Setup

At the Input Level, SHAP [8] is applied using modality-appropriate configurations: a word-level text masker for text, KernelExplainer for tabular data, and GradientExplainer for image data.

At the Internal Level, architecture-specific explanation methods summarized in Table 1 are employed. Gradient-weighted Attention Attribution is used for BERT, Gradient x Input for Bi-LSTM, SHAP TreeExplainer for XGBoost, Integrated Gradients for MLP, and Grad-CAM for ResNet-20. These methods are selected to exploit each architecture's computational characteristics directly.

4.2.2. Quantitative Evaluation Setup

Faithfulness is evaluated using NAOPC [15] at both the Input and Internal Levels. Predictive performance is evaluated on the complete test set using F1-score.
HRS is computed using Equation 6 with equal weights by default, while weighted HRS_w uses the domain-specific configurations described in Section 3.2.4.

4.2.3. Implementation Details

All experiments used random seed 42. For each model, Input and Internal NAOPC used the same 200 test samples: stratified sampling for adult and random sampling without replacement for text and CIFAR-10. Text evaluation used at most the first 20 words or valid tokens with beam size 1; Adult evaluated all 14 features and CIFAR-10 all 64 non-overlapping 4 x 4 blocks with beam size 2. Perturbations replaced words with [UNK], internal token embeddings with zeros, tabular features with training-set means, and image blocks with the original image's per-channel means. Confidence changes were measured for the originally predicted class, including incorrect predictions. Kernel SHAP used 50 k-means centroids, Gradient SHAP used 50 randomly selected training images, and MLP Integrated Gradients used 50 steps from the scaled training mean.

5. Results and Discussion

This section reports the qualitative and quantitative outcomes of the proposed multi-level evaluation framework. We first summarize how qualitative explanations support inspection of model behavior, then compare the evaluated architectures using NAOPC, F1, HRS, and HRS_w Finally, we validate the diagnostic value of the framework and analyze the resulting Triangle Graphs.

5.1. Qualitative Results

Qualitative explanations were generated for all three modalities as the first stage of the framework. This stage makes model behavior inspectable before numerical evaluation. Qualitative explanations show which input features, tokens, or image regions are emphasized by an explanation method. The same explanations also help compare whether Input-Level and Internal-Level explanations point to similar or different evidence. Figure 3 presents representative Internal-Level explanations for text, tabular, and image classification tasks. In the text panel, the y-axis lists tokens and the x-axis reports their Gradient-weighted Attention attribution scores, so longer bars indicate stronger token-level internal evidence for BERT. In the tabular panel, the y-axis lists UCI Adult features and the x-axis reports TreeExplainer attribution scores for XGBoost. In the image panel, Grad-CAM is shown as a spatial heatmap rather than a numeric x-y plot. Warmer regions indicate image areas used more strongly by ResNet-20 for classification. Together, these examples show that the Internal Level is architecture-dependent and must be interpreted with methods matched to each model type. However, qualitative inspection alone is subjective and difficult to compare across datasets, architectures, and explanation methods. Therefore, the qualitative stage is used as supporting evidence. Model comparison is based on the quantitative NAOPC, F1, HRS, and Triangle Graph results reported in the following sections.

5.2. Quantitative Results

The quantitative analysis converts the qualitative explanation outputs and predictive performance into comparable scores for each evaluation level.

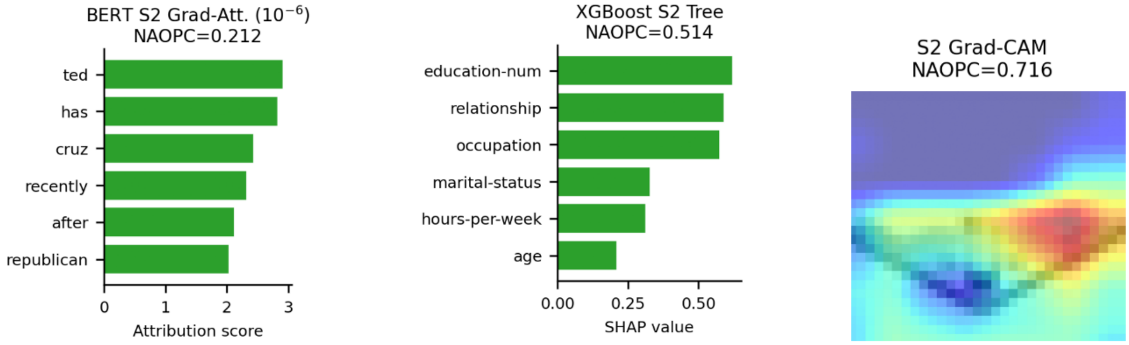

Figure 3. Representative Internal-Level qualitative explanations for text, tabular, and image classification tasks.

Table 2 summarizes the three axis scores and the derived HRS and HRS_w for all architecture-dataset combinations. Input and Internal scores are NAOPC [15] values averaged over 200 sampled observations, while Output is binary F1 for IMDb, ISOT, and UCI Adult and macro-F1 for CIFAR-10. Weighted HRS_w follows Equation 7 using domain-specific priorities for Input, Internal, and Output. As reported in Table 2, no evaluated architecture is uniformly strongest across all three axes. The score differences arise from the interaction between dataset modality, architecture, and the explanation method used at each level. Thus, reliability cannot be inferred from Output F1 alone.

Table 2. Multi-level evaluation results for evaluated architectures.

Modality	Dataset	Architecture	Input NAOPC	Internal NAOPC	Output F1	HRS	HRS_w
Text	IMDb	BERT	0.7958	0.2800	0.8971	0.3960	0.4755
Text	IMDb	Bi-LSTM	0.9218	0.2331	0.8869	0.4130	0.5141
Text	ISOT	BERT	0.7648	0.2121	1.0000	0.3797	0.5847
Text	ISOT	Bi-LSTM	0.8756	0.2563	0.9896	0.4482	0.6714
Tabular	UCI Adult	XGBoost	0.7853	0.5137	0.7190	0.4458	0.4496
Tabular	UCI Adult	MLP	0.8756	0.4508	0.6804	0.4324	0.4358
Image	CIFAR-10	ResNet-20	0.6595	0.7158	0.7378	0.4956	0.5020

For IMDb and ISOT, BERT and Bi-LSTM achieve high Output F1. Their Internal NAOPC [15] scores are much lower than their Input NAOPC scores. One possible explanation is that SHAP perturbs words directly, whereas Gradient x Input and Gradient-weighted Attention Attribution operate over embeddings or attention patterns. Thus, BERT can reach perfect F1 on ISOT while still receiving the lowest HRS because its high Output score is combined with weaker Input and Internal faithfulness.

For UCI Adult, XGBoost and MLP produce comparatively even score profiles. XGBoost obtains higher Internal NAOPC, which may reflect TreeExplainer's direct use of tree structure, while MLP obtains higher Input NAOPC under SHAP KernelExplainer. Their HRS values are therefore close. For CIFAR-10, ResNet-20 obtains the highest HRS despite moderate F1; this result may reflect the interaction between Grad-CAM, convolutional spatial features, and the block-level SHAP perturbation procedure. It is the only evaluated case where Internal NAOPC exceeds Input NAOPC.

These differences should not be attributed solely to model architecture. Input and Internal scores may also be affected by the attribution method, perturbation baseline, masking strategy, feature granularity, tokenization, dataset characteristics, and model training. For example, word-level masking may not align perfectly with BERT subword tokenization, while image-block perturbation may affect SHAP and Grad-CAM differently. The results therefore reflect the combined effect of the model, explanation method, and evaluation configuration.

5.3. Framework Validation

To validate the contribution of the proposed framework, we compare conclusions obtained from Output F1 with those obtained from HRS within the same dataset. The framework is not intended to replace individual XAI methods; it supplements predictive evaluation by jointly considering explanation faithfulness and predictive performance.

Table 3. Within-dataset comparison of predictive and integrated framework evaluation.

Dataset	Models compared	F1-based conclusion	HRS-based conclusion
IMDb	BERT vs. Bi-LSTM	BERT higher: 0.8971 vs. 0.8869	Bi-LSTM higher: 0.4130 vs. 0.3960
ISOT	BERT vs. Bi-LSTM	BERT higher: 1.0000 vs. 0.9896	Bi-LSTM higher: 0.4482 vs. 0.3797
UCI Adult	XGBoost vs. MLP	XGBoost higher: 0.7190 vs. 0.6804	XGBoost higher: 0.4458 vs. 0.4324

Table 3 demonstrates the framework through within-dataset comparisons. On IMDb and ISOT, BERT achieves slightly higher F1, whereas Bi-LSTM achieves higher HRS because of its combined Input, Internal, and Output profile. On UCI Adult, XGBoost achieves both higher F1 and slightly higher HRS than MLP, although MLP has the stronger Input-Level score. ResNet-20 is presented separately because no second image architecture was evaluated on CIFAR-10. HRS comparisons are most meaningful between models evaluated on the same dataset under consistent evaluation settings.

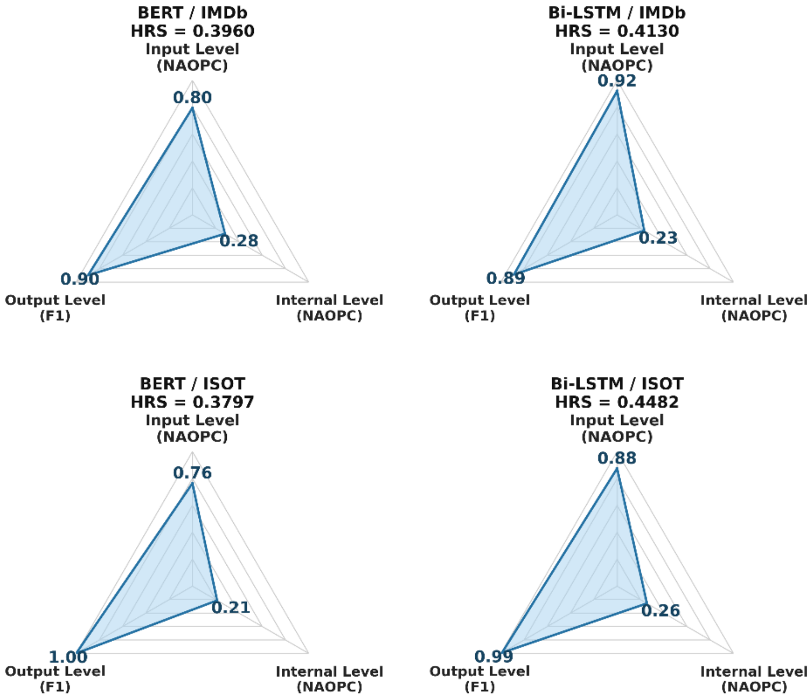

Figure 4. Triangle Graphs for BERT and Bi-LSTM on IMDb and ISOT. Each radial axis ranges from 0 to 1 and represents Input NAOPC, Internal NAOPC, or Output F1.

5.4. Triangle Graph Analysis

As shown in Figure 4, the Triangle Graphs use radial axes rather than Cartesian x-y axes. The top axis represents Input NAOPC, the lower-right axis represents Internal NAOPC, and the lower-left axis represents Output F1. Values farther from the center indicate stronger scores. The IMDb and ISOT results form elongated shapes with short Internal axes, showing a consistent gap between predictive performance and internal faithfulness. On ISOT, BERT and Bi-LSTM are nearly identical by F1, but Bi-LSTM forms a larger triangle due to stronger Input and Internal scores.

Figure 5 shows that the tabular and image experiments have visually more symmetric profiles than the text experiments, with ResNet-20 producing the most symmetric triangle. Its combination of Input, Internal, and Output scores also produces the largest normalized triangle area and therefore the highest HRS among the evaluated cases. Triangle symmetry and HRS area provide complementary, rather than identical, information.

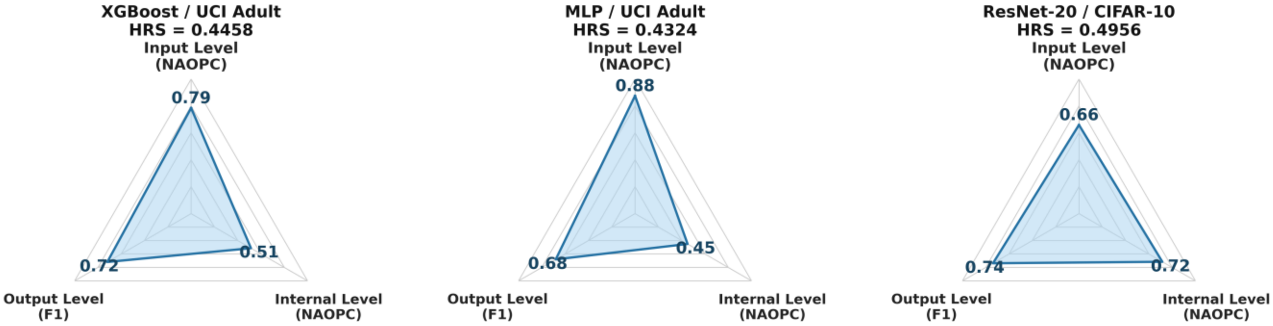

Figure 5. Triangle Graphs for tabular and image architectures on UCI Adult and CIFAR-10. The radial axes follow the same Input NAOPC, Internal NAOPC, and Output F1 scale as Figure 4.

5.5. Limitations

The study has several limitations. First, NAOPC [15] is computationally expensive, and the reported estimates use 200 samples with modality-specific evaluation units: at most 20 words or tokens for text, all 14 features for Adult, and 64 image blocks for CIFAR-10. Confidence intervals and sensitivity analyses across alternative sample sizes, feature limits, perturbation baselines, and beam sizes were not conducted. Second, Internal-Level scores depend on the selected attribution method and may reflect attribution limitations rather than model behavior alone. Third, cross-dataset HRS values are descriptive because the tasks, feature units, and perturbation procedures differ. Finally, only one architecture was evaluated on CIFAR-10, and the domain-specific HRS weights were manually assigned rather than validated with stakeholders.

6. Conclusions

This paper presented a multi-level XAI evaluation framework that combines Input-Level attribution faithfulness, architecture-specific attribution faithfulness, and predictive performance through the Triangle Graph and an area-based Holistic Reliability Score. Within the evaluated datasets, the framework showed that models with similar predictive performance can exhibit different attribution-faithfulness profiles. The within-dataset comparisons demonstrate how HRS can supplement F1-score by making the source of model differences explicit. These findings demonstrate the diagnostic utility of the framework in the evaluated settings rather than establishing a universal model ranking or a fully validated measure of reliability. Further evaluation across additional architectures, attribution methods, perturbation strategies, and practitioner studies is required before broader application. Future work will also investigate computational efficiency, uncertainty estimation, and systematic selection of domain-specific weights.

Acknowledgements
The first author gratefully thanks Wanida Putthividhya and Thapana Boonchoo for their guidance, supervision, and valuable feedback throughout this work. The authors also thank the Department of Computer Science, Faculty of Science and Technology, Thammasat University for institutional support.

References
[1] Arrieta, A. B.; Diaz-Rodriguez, N.; Del Ser, J.; Bennetot, A.; Tabik, S.; Barbado, A.; Garcia, S.; Gil-Lopez, S.; Molina, D.; Benjamins, R.; Chatila, R.; Herrera, F. Explainable Artificial Intelligence (XAI): Concepts, Taxonomies, Opportunities and Challenges toward Responsible AI. Information Fusion 2020, 58, 82-115.
[2] Goodman, B.; Flaxman, S. European Union Regulations on Algorithmic Decision-Making and a Right to Explanation. AI Magazine 2017, 38 (3), 50-57.
[3] Jacovi, A.; Goldberg, Y. Towards Faithfully Interpretable NLP Systems: How Should We Define and Evaluate Faithfulness? arXiv 2020, arXiv:2004.03685.
[4] Alvarez-Melis, D.; Jaakkola, T. S. On the Robustness of Interpretability Methods. arXiv 2018, arXiv:1806.08049.
[5] Krishna, S.; Han, T.; Gu, A.; Wu, S.; Jabbari, S.; Lakkaraju, H. The Disagreement Problem in Explainable Machine Learning: A Practitioner's Perspective. arXiv 2022, arXiv:2202.01602.
[6] Neely, M.; Schouten, S. F.; Bleeker, M. J. R.; Lucic, A. Order in the Court: Explainable AI Methods Prone to Disagreement. arXiv 2021, arXiv:2105.03287.
[7] Kaur, H.; Nori, H.; Jenkins, S.; Caruana, R.; Wallach, H.; Wortman Vaughan, J. Interpreting Interpretability: Understanding Data Scientists' Use of Interpretability Tools for Machine Learning. In Proceedings of the 2020 CHI Conference on Human Factors in Computing Systems; ACM: New York, NY, USA, 2020; pp. 1-14.
[8] Lundberg, S. M.; Lee, S.-I. A Unified Approach to Interpreting Model Predictions. In Advances in Neural Information Processing Systems 30; Curran Associates, Inc., 2017; pp. 4765-4774.
[9] Ribeiro, M. T.; Singh, S.; Guestrin, C. Why Should I Trust You? Explaining the Predictions of Any Classifier. In Proceedings of the 22nd ACM SIGKDD International Conference on Knowledge Discovery and Data Mining; ACM: New York, NY, USA, 2016; pp. 1135-1144.
[10] Sundararajan, M.; Taly, A.; Yan, Q. Axiomatic Attribution for Deep Networks. In Proceedings of the 34th International Conference on Machine Learning; PMLR, 2017; Vol. 70, pp. 3319-3328.
[11] Vaswani, A.; Shazeer, N.; Parmar, N.; Uszkoreit, J.; Jones, L.; Gomez, A. N.; Kaiser, L.; Poloukhin, I. Attention Is All You Need. In Advances in Neural Information Processing Systems 30; Curran Associates, Inc., 2017; pp. 5998-6008.
[12] Jain, S.; Wallace, B. C. Attention Is Not Explanation. In Proceedings of NAACL-HLT 2019; Association for Computational Linguistics, 2019; pp. 3543-3556.
[13] Selvaraju, R. R.; Cogswell, M.; Das, A.; Vedantam, R.; Parikh, D.; Batra, D. Grad-CAM: Visual Explanations from Deep Networks via Gradient-Based Localization. International Journal of Computer Vision 2020, 128 (2), 336-359.
[14] DeYoung, J.; Jain, S.; Rajani, N. F.; Lehman, E.; Xiong, C.; Socher, R.; Wallace, B. C. ERASER: A Benchmark to Evaluate Rationalized NLP Models. In Proceedings of the 58th Annual Meeting of the Association for Computational Linguistics; Association for Computational Linguistics, 2020; pp. 4443-4458.
[15] Edin, J.; Motzfeldt, A. G.; Christensen, C. L.; Ruotsalo, T.; Maaloe, L.; Maistro, M. Normalized AOPC: Fixing Misleading Faithfulness Metrics for Feature Attribution Explainability. In Proceedings of the 63rd Annual Meeting of the Association for Computational Linguistics; Association for Computational Linguistics, 2025; pp. 1715-1730.

[16] Nauta, M.; Trienes, J.; Pathak, S.; Nguyen, E.; Peters, M.; Schmitt, Y.; Schlötterer, J.; van Keulen, M.; Seifert, C. From Anecdotal Evidence to Quantitative Evaluation Methods: A Systematic Review on Evaluating Explainable AI. ACM Computing Surveys 2023, 55 (13s), Article 295, 1-42.
[17] Arya, V.; Bellamy, R. K. E.; Chen, P.-Y.; Dhurandhar, A.; Hind, M.; Hoffman, S. C.; Houde, S.; Liao, Q. V.; Luss, R.; Mojsilovic, A.; Mourad, S.; Pedemonte, P.; Raghavendra, R.; Richards, J.; Sattigeri, P.; Shanmugam, K.; Singh, M.; Varshney, K. R.; Wei, D.; Zhang, Y. One Explanation Does Not Fit All: A Toolkit and Taxonomy of AI Explainability Techniques. arXiv 2019, arXiv:1909.03012.
[18] Sokol, K.; Flach, P. Explainability Fact Sheets: A Framework for Systematic Assessment of Explainable Approaches. In Proceedings of the 2020 Conference on Fairness, Accountability, and Transparency; ACM: New York, NY, USA, 2020; pp. 56-67.
[19] Braden, B. The Surveyor's Area Formula. The College Mathematics Journal 1986, 17 (4), 326-337.
[20] Maas, A. L.; Daly, R. E.; Pham, P. T.; Huang, D.; Ng, A. Y.; Potts, C. Learning Word Vectors for Sentiment Analysis. In Proceedings of the 49th Annual Meeting of the Association for Computational Linguistics: Human Language Technologies; Association for Computational Linguistics, 2011; pp. 142-150.
[21] Ahmed, H.; Traore, I.; Saad, S. Detection of Online Fake News Using N-Gram Analysis and Machine Learning Techniques. In Intelligent, Secure, and Dependable Systems in Distributed and Cloud Environments; Springer, 2017; pp. 127-138.
[22] Hochreiter, S.; Schmidhuber, J. Long Short-Term Memory. Neural Computation 1997, 9 (8), 1735-1780.
[23] Devlin, J.; Chang, M.-W.; Lee, K.; Toutanova, K. BERT: Pre-Training of Deep Bidirectional Transformers for Language Understanding. In Proceedings of NAACL-HLT 2019; Association for Computational Linguistics, 2019; pp. 4171-4186.
[24] Becker, B.; Kohavi, R. Adult [Dataset]. UCI Machine Learning Repository, 1996.
[25] Chen, T.; Guestrin, C. XGBoost: A Scalable Tree Boosting System. In Proceedings of the 22nd ACM SIGKDD International Conference on Knowledge Discovery and Data Mining; ACM: New York, NY, USA, 2016; pp. 785-794.
[26] Goodfellow, I.; Bengio, Y.; Courville, A. Deep Learning; MIT Press: Cambridge, MA, USA, 2016.
[27] Krizhevsky, A. Learning Multiple Layers of Features from Tiny Images; Technical Report; University of Toronto: Toronto, ON, Canada, 2009.
[28] He, K.; Zhang, X.; Ren, S.; Sun, J. Deep Residual Learning for Image Recognition. In Proceedings of the IEEE Conference on Computer Vision and Pattern Recognition; IEEE, 2016; pp. 770-778.

II. Renewable Energy and Green Technology

A Study on the Effects of Translucent Roofing Sheets on Indoor Lighting Conditions During Thailand's Rainy Season

Pocharapon Silakoop[1*], Preeda Chantawong[2*], Dusit Ngamrungroj[1], Pinthudit Klinkajorn[2]

[1] Energy Engineering Technology Department of Power Engineering Technology,
College of Industrial Technology, King Mongkut's University of Technology North Bangkok,[3]
[2] Department of Social and Applience, College of Industrial Technology, King Mongkut's University of Technology North Bangkok, Bangkok 10800, Thailand
Corresponding Email: pocharaponwdet11@gmail.com[1*], cpreeda@yahoo.com [2*]

Abstract: Lighting is an essential factor for human vision, daily life, and work efficiency. Natural light, in particular, is an important energy source that helps reduce electricity consumption within buildings. Therefore, designing buildings to effectively utilize natural daylight has become a significant approach for energy conservation and for creating suitable indoor environmental conditions. At present, translucent roofing materials such as polycarbonate sheets and fiberglass sheets are widely used as roofing components in buildings to increase the amount of natural light entering indoor spaces and reduce dependence on artificial lighting. However, the light transmission and light diffusion performance of each material differ, especially under varying weather conditions during the rainy season, when cloud cover increases, outdoor light intensity decreases, and humidity levels rise. These factors can significantly affect indoor lighting conditions. Thailand has a tropical climate with a long rainy season. As a result, the use of translucent roofing sheets in buildings may be influenced by such climatic conditions, causing indoor illuminance levels to fall below standard requirements or user needs. This may affect work efficiency, visual comfort, and overall energy consumption within buildings. Therefore, this research aims to study the effects of translucent roofing sheets on indoor lighting conditions during Thailand's rainy season by comparing the light transmission properties of different translucent roofing materials. The findings are expected to provide useful information for selecting appropriate roofing materials in building design to improve lighting efficiency and energy conservation.

Keywords: Natural light, polycarbonate, fiberglass, Translucent Roofing

1. Introduction

Natural light is considered an important factor in enhancing visual efficiency and reducing electrical energy consumption within buildings. Translucent roofing materials are therefore used to increase the transmission of light into interior spaces.[1],[2] Natural lighting plays a vital role in enhancing visual comfort, improving occupants' performance, and reducing electrical energy consumption within buildings. [3],[4] In modern architectural design, translucent roofing sheets are widely used in industrial buildings, warehouses, agricultural structures, and residential spaces to allow daylight to penetrate interior areas while minimizing the need for artificial lighting during daytime.[5] Different translucent roofing materials possess varying light transmission and diffusion properties, which directly affect indoor illuminance levels and lighting quality [4].

Thailand is a tropical country with high solar radiation throughout most of the year. However, during the rainy season, cloud cover and weather variability significantly reduce natural light intensity, affecting indoor daylight availability. These environmental changes may affect the performance of translucent roofing sheets in providing adequate indoor illumination. Inadequate lighting conditions can negatively influence visibility, occupants' comfort, and work efficiency, especially in buildings that rely heavily on natural daylight [6].

Although translucent roofing materials are commonly applied in Thailand, studies focusing specifically on their lighting performance during the rainy season remain limited. Therefore, this research aims to investigate the effects of different translucent roofing sheets on indoor lighting conditions during Thailand's rainy season in order to provide useful information for selecting suitable roofing materials and improving energy-efficient building design [7-8].

This study investigates the effects of different translucent roofing sheets on indoor lighting conditions during Thailand's rainy season, focusing on their light transmission performance and their suitability for improving indoor illumination and energy-efficient building design.

2. Materials and Methods

This study evaluates the indoor lighting performance of translucent roofing sheets during the rainy season in Thailand, using a specially constructed experimental house for research purposes. Two types of translucent roofing materials were investigated: polycarbonate roofing sheets and fiberglass roofing sheets. Both materials are translucent, as illustrated in Figure 1. The two types of roofing materials were installed on the upper portion of the roof to assess their daylight transmission properties and their effectiveness in providing natural illumination within the building.

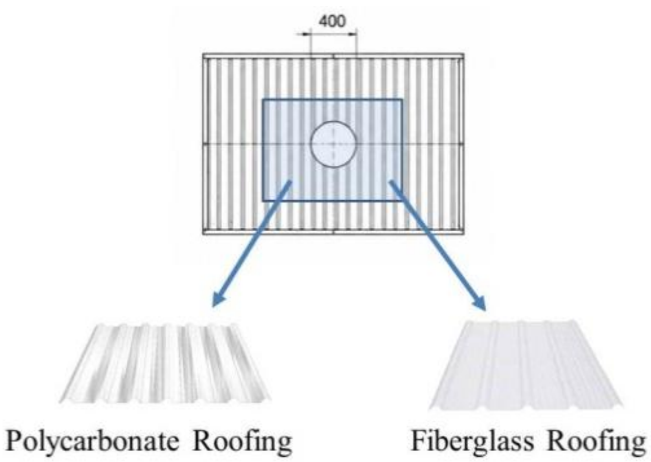

Figure 1. Translucent roofing materials used in the study: (a) polycarbonate roofing sheet and (b) fiberglass roofing sheet**.**

To evaluate the daylight transmission performance of the roofing materials, a circular opening with a diameter of 400 mm was constructed at the center of the roof of each experimental house. The translucent roofing sheets were installed over the opening, as illustrated in Figure 2. Indoor illuminance levels resulting from daylight transmission through the roofing materials were measured and compared under natural daylight conditions during Thailand's rainy season. Indoor illuminance levels were measured using a Digital Lux Meter, while a Data Logger was employed for continuous data acquisition. The measurement system consisted of nine Light Dependent Resistors (LDRs), designated as S1–S9, which were installed on the floor of each experimental house.

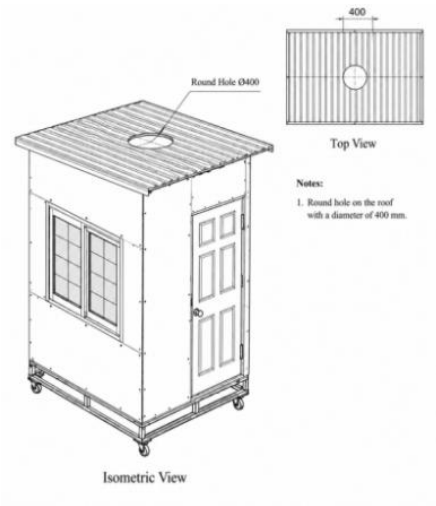

Figure 2. Circular roof opening (400 mm diameter) used to evaluate the daylight transmission performance of translucent roofing materials.

The sensors were arranged in a grid pattern, as illustrated in Figure 3, to evaluate the spatial distribution of daylight transmitted through the translucent roofing materials via the circular roof opening. The measurements were conducted during daytime, from sunrise to sunset. Data collection for each type of roofing sheet was carried out over a one-day period, from 05:00 a.m. to 07:00 p.m. The study was performed under typical rainy-season weather conditions in Thailand, encompassing both overcast and predominantly cloudy skies. Illuminance data were recorded at predetermined time intervals and subsequently analyzed to compare the daylight transmission performance of the two types of translucent roofing sheets. The collected data were used to evaluate the effectiveness of each roofing material in providing natural illumination within the building.

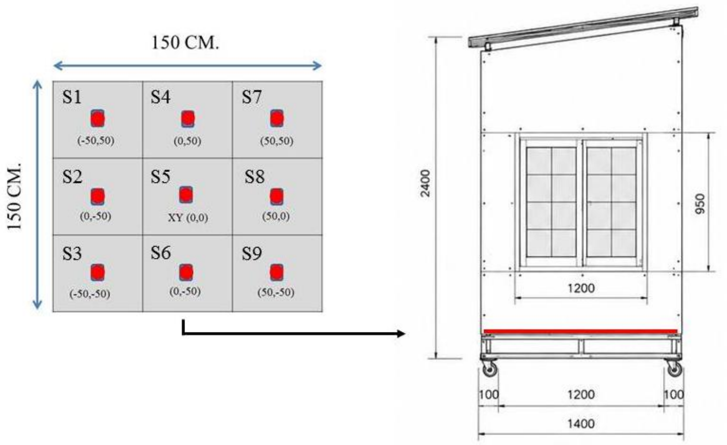

Figure 3. Installation layout of Light Dependent Resistor (LDR) sensors for indoor illuminance measurements in the experimental house.

The experimental procedure focused on comparing the lighting performance, light distribution, and daylight penetration of each roofing material. The collected data were analyzed using descriptive and comparative methods to determine the suitability of translucent roofing sheets for improving indoor lighting conditions and supporting energy-efficient building design in Thailand. Thermocouples were installed to monitor the temperature conditions inside and outside the experimental house, as shown in Figure 4.

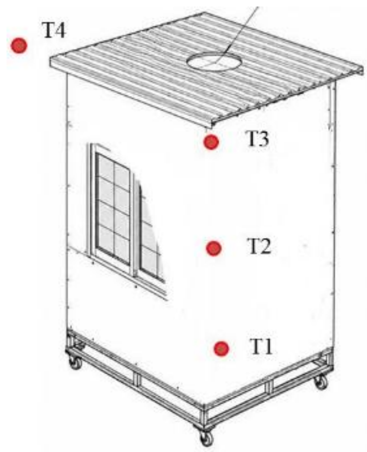

Figure 4. Installation of thermocouple sensors for indoor and outdoor temperature measurements

Temperature measurements were recorded simultaneously with illuminance data and stored in the Data Logger throughout the experimental period. A total of four thermocouple measurement points were established. Three thermocouples were installed inside the experimental house: Point 1 (T1) was located at floor level, corresponding to the height of the illuminance sensors; Point 2 (T2) was positioned at the center of the indoor space; and Point 3 (T3) was installed directly beneath the translucent roofing sheet. The fourth thermocouple, Point 4 (T4), was installed outside the experimental house to measure ambient outdoor temperature. This arrangement enabled the evaluation of temperature distribution within the test house and the comparison of indoor and outdoor thermal conditions.

3. Results and Discussion

The experimental results of illuminance measurements through the fiberglass roofing sheet are presented in Figure 5. During the early morning period, when natural daylight was relatively low, the indoor illuminance level was approximately 100 lux. As solar elevation increased toward midday and the sun's rays became more perpendicular to the roofing surface, the measured illuminance gradually increased, reaching a peak value of approximately 500 lux.

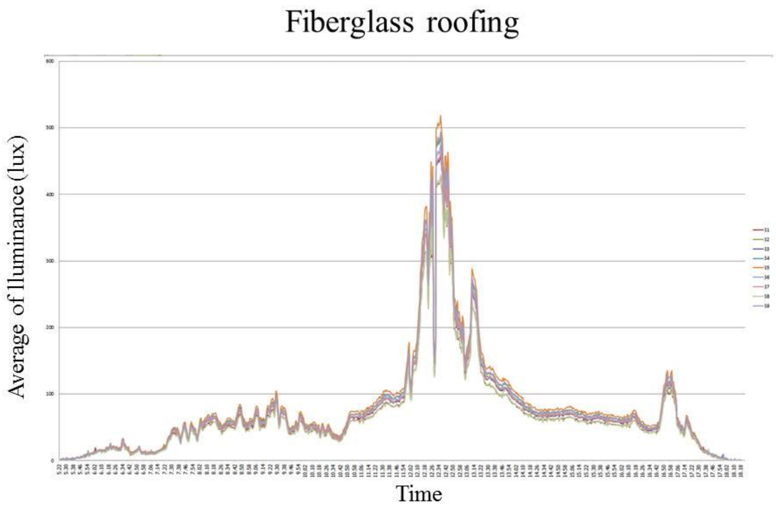

Figure 5. Indoor illuminance levels transmitted through the fiberglass roofing sheet

After midday, the illuminance level gradually decreased as the solar angle changed and daylight availability declined. During the afternoon period, illuminance values decreased to approximately 100 lux and continued to decline until reaching nearly 0 lux after sunset. These results demonstrate the variation in daylight transmission through the fiberglass roofing sheet throughout the day under natural lighting conditions. Temperature measurements were conducted simultaneously with illuminance measurements throughout the experimental period. The temperature profiles obtained from the experimental house equipped with the fiberglass roofing sheet are presented in Figure 6. During the morning period, temperatures ranged from approximately 27 °C to 32 °C. As solar radiation increased toward midday, temperatures gradually rose. The highest temperature was recorded beneath the fiberglass roofing sheet, reaching approximately 40 °C. At the same time, the indoor air temperature within the experimental house ranged between 30 °C and 33 °C, while the outdoor ambient temperature reached approximately 35 °C. Following midday, temperatures gradually decreased as solar radiation diminished, continuing to decline until the evening period. These results indicate that the fiberglass roofing sheet allowed daylight penetration while maintaining indoor temperatures lower than the temperature measured directly beneath the roofing material.

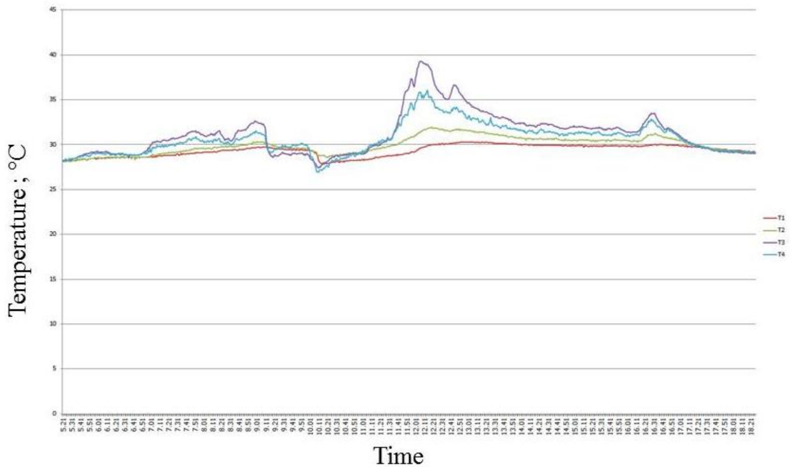

Figure 6. Temperature profiles measured at different locations within the experimental house equipped with the fiberglass roofing sheet.

The daylight transmission performance of the polycarbonate roofing sheet was evaluated and compared with that of the fiberglass roofing sheet. The illuminance measurements obtained from the experimental house equipped with the polycarbonate roofing sheet are presented in Figure 7.
During the early morning period, the measured indoor illuminance ranged from approximately 100 to 200 lux. As the solar altitude increased toward midday and the incident sunlight became more perpendicular to the roofing surface, the illuminance level gradually increased from approximately 200 lux to a peak value of about 1,000 lux.

After midday, the illuminance level gradually decreased as solar radiation and daylight availability declined. During the afternoon period, illuminance values ranged from approximately 100 to 400 lux before continuing to decrease toward 0 lux after sunset. The results indicate that the polycarbonate roofing sheet provided significantly higher daylight transmission than the fiberglass roofing sheet, particularly during periods of peak solar radiation around midday.

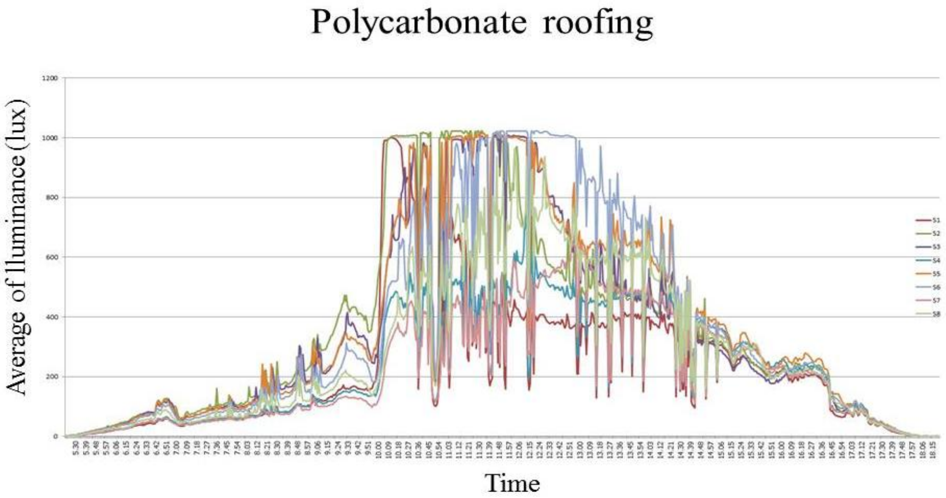

Figure 7. Indoor illuminance levels transmitted through the polycarbonate roofing sheet.

Temperature measurements were also conducted in the experimental house equipped with the polycarbonate roofing sheet, as presented in Figure 8. During the morning period, the recorded temperatures ranged from approximately 27 °C to 32 °C. As solar radiation increased toward midday, temperatures gradually rose.

The highest temperature was observed directly beneath the polycarbonate roofing sheet, reaching approximately 40 °C. Meanwhile, the indoor air temperature within the experimental house ranged between 30 °C and 35 °C, whereas the outdoor ambient temperature reached approximately 36 °C. Following midday, temperatures gradually decreased as solar radiation diminished and continued to decline until the evening period.

These results indicate that the polycarbonate roofing sheet allowed greater daylight transmission while maintaining indoor thermal conditions comparable to those observed in the experimental house equipped with the fiberglass roofing sheet.

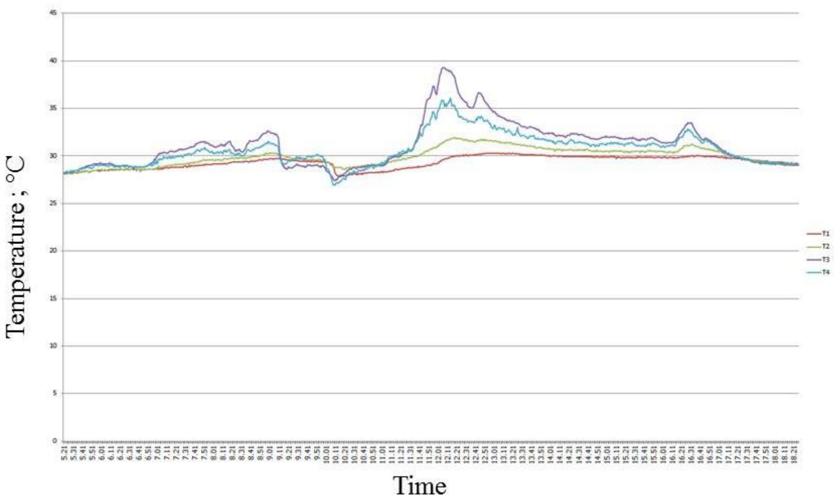

Figure 8. Temperature profiles measured at different locations within the experimental house equipped with the polycarbonate roofing sheet.

4. Conclusions

This study investigated the performance of translucent roofing materials in providing natural indoor daylight during Thailand's rainy season through a comparative experimental analysis of fiberglass and polycarbonate roofing sheets. The results showed that both materials were capable of transmitting natural daylight into the experimental houses, thereby reducing reliance on artificial lighting during daytime hours. However, significant differences were observed in their daylight transmission performance.

The polycarbonate roofing sheet demonstrated clearly superior optical performance compared with the fiberglass roofing sheet. During peak daylight conditions around midday, the polycarbonate roofing achieved indoor illuminance levels of approximately 1,000 lux, whereas the fiberglass roofing reached a maximum of approximately 500 lux. The higher illuminance provided by the polycarbonate sheet reflects its greater ability to transmit natural daylight through the roofing system. This characteristic is particularly beneficial for enhancing visual comfort and reducing the need for electric lighting during daytime operation, even under cloudy and overcast conditions commonly experienced during Thailand's rainy season.

The temporal variation in illuminance throughout the day followed a similar pattern for both materials. Illuminance gradually increased after sunrise, reached a peak at midday when solar radiation was strongest, and then decreased toward sunset. Nevertheless, the polycarbonate roofing consistently provided higher illuminance levels than the fiberglass roofing throughout the measurement period, confirming its superior daylight utilization performance.

In addition to illuminance measurements, thermal performance was assessed through continuous temperature monitoring at multiple locations inside and outside the experimental houses. The results indicated that both roofing materials exhibited similar thermal behavior. The maximum temperature beneath the translucent roofing reached approximately 40°C at midday, while indoor air temperatures ranged between 30–35°C. Outdoor temperatures were approximately 35–36°C during the same period. Although the polycarbonate roofing transmitted significantly more daylight, no substantial increase in indoor air temperature was observed compared with the fiberglass roofing. This indicates that improved daylight transmission can be achieved without causing a significant deterioration in indoor thermal conditions.

From an application perspective, the findings suggest that polycarbonate roofing sheets offer considerable advantages for daylighting applications in residential, agricultural, and industrial buildings where natural lighting is desirable. Enhanced daylight transmission can reduce electricity consumption for artificial lighting, supporting energy-efficient and sustainable building design. In addition, increased access to natural daylight can improve indoor environmental quality and occupant comfort.

According to standard indoor illuminance requirements stipulated by building regulations, recommended lighting levels vary by function: general circulation areas such as corridors, stairs, and elevators require approximately 100 lux; office-related spaces such as meeting rooms require 200–300 lux; computer workstations and clinical examination rooms require 300–500 lux; and visually demanding tasks such as laboratories or assembly work require 500 lux or higher. The illuminance levels measured in this study indicate that translucent roofing materials can be applied to achieve indoor lighting conditions that comply with these regulatory standards.

In summary, the results demonstrate that polycarbonate roofing sheets provide superior natural daylighting performance while maintaining thermal conditions comparable to those of fiberglass roofing sheets. Therefore, polycarbonate materials are more suitable for enhancing natural indoor illumination in buildings located in tropical regions with prolonged rainy seasons, such as Thailand.

Future research should investigate additional types of translucent roofing materials, alternative roof geometries and installation configurations, seasonal variations throughout the year, and the long-term energy-saving potential of daylight utilization. Moreover, studies integrating illuminance performance, thermal behavior, occupant comfort, and economic analysis would provide a more comprehensive evaluation of translucent roofing systems for sustainable building applications.

5. Acknowledgements

The researcher would like to express sincere gratitude to the advisor and all faculty members for their valuable guidance, constructive suggestions, and academic support throughout the duration of this research.

References

[1] Bora,R.,etal.(2023).*The Effect of Light Shelf and Translucent Ceiling on Daylighting Performance in Office Building in Thailand.*

[2] Yu,F.,&Leng,J.(2020).*Quantitative effects of glass roof system parameters on energy and daylightingperformances.*Lighting Research & Technology, 30(8).

[3] Asdrubali, F. (2003). *Daylighting performance of sawtooth roofs of industrial buildings.* Lighting Research & Technology, 35(4), 343–359.

[4] Schöttl, P., et al. (2018). *Daylight Performance of a Translucent Textile Membrane Roof with Thermal Insulation.* Buildings, 8(9), 118.

[5] Yu, F., & Leng, J. (2020). *Quantitative effects of glass roof system parameters on energy and daylighting performances.* Lighting Research & Technology.

[6] Bora, R., et al. (2023). *The Effect of Light Shelf and Translucent Ceiling on Daylighting Performance in Office Building in Thailand.* Journal of Built Environment

[7] Chung, Y.G.; Seo, S.Y. Polycarbonate daylighting performance on the top-lit building. Applied Mechanics and Materials 2013, 361–363, 925–929. https://doi.org/10.4028/www.scientific.net/AMM.361-363.925.

[8] Gürlich, D.; Reber, A.; Biesinger, A.; Eicker, U. Daylight performance of a translucent textile membrane roof with thermal insulation. Buildings 2018, 8, 118. https://doi.org/10.3390/buildings8090118.

InC MPPT with nonlinear control for a PV boost converter feeding an AC grid-connected converter

Unchittha Prasatsap[1], Nattapong Nernchad[2], Sakda Somkun[1], Matheepot Phattanasak[3*], Ehsan Jamshidpour[4], and Serge Pierfederici[5]

[1] School of Renewable Energy and Smart Grid Technology (SGtech), Naresuan University, Phitsanulok 65000, Thailand
[2] Electrical Technology Program, Faculty of Industrial Technology, Uttaradit Rajabhat University, Uttaradit, Thailand
[3]Department of Teacher Training in Electrical Engineering, King Mongkut's University of Technology North Bangkok, Thailand
[4] Group of Research in Electrical Engineering, University of Lorraine, Nancy, France
[5] LEMTA, University of Lorraine, Nancy, France
* Correspondence: matheepot.p@fte.kmutnb.ac.th

Abstract

Extracting the maximum power from photovoltaic (PV) panels is crucial. This paper presents an approach to implement the maximum power point tracker (MPPT) using the well-known incremental conduction (InC) method, with a boost converter feeding a three-phase AC grid via an inverter. A PV panel is connected to a PV capacitor. The capacitor voltage is controlled via a nonlinear cascade control system, with the inner loop regulating the inductor current and the outer loop regulating the PV capacitor voltage to extract maximum power under the given conditions. The output voltage of the boost converter, connected to the inverter, is controlled by the inverter using a well-known cascade PI controller. Simulation results show that, with nonlinear control, the tracking response is faster than that of the PI controller with a lower PV capacitance, while the inductor current can be limited.

Keywords: Photovoltaic cells; InC MPPT; Boost converter; Three-phase inverter

1. Introduction

Electrical energy for industrial, transportation, and household use is crucial. Electricity can be generated from renewable sources. Renewable energy is particularly important now due to the scarcity of crude oil and natural gas, driven by global conflicts, as well as problems such as global warming and pollution [1]-[3].

Sunlight is abundant during the day and can be converted into electricity using photovoltaic (PV) cells connected in series [4]-[5]. To extract the maximum power under the given conditions, a maximum power point tracker (MPPT) is always used. Several types of MPPTs are available in the literature, ranging from a simple perturb-and-observe (P&O) MPPT to more sophisticated ones that use built-in, optimized artificial intelligence to overcome partial shading [6]-[11]. Nonetheless, all MPPT algorithms generate a reference signal for a power circuit, typically a high-efficiency DC-DC switching converter. The output from the MPPT can be a duty cycle, a current reference, or a PV voltage reference, depending on the control structure of the DC-DC converter being used.

Because the PV panel is considered a current source, a capacitor is usually connected at the PV connector to establish the PV voltage [12]. The capacitance must be sufficient to hold the voltage constant during MPPT processing [13]. Therefore, a high capacitance, typically provided by an electrolytic capacitor, is used. However, its life is short due to its structure. If the capacitance can be reduced, a small capacitance with other technologies, such as film types, can be used to offer long-life operation. This brings us not only a long-life system but also lower cost, smaller size, and volume [14].

In a PV system, to prevent a fire caused by a short circuit, the PV current must be controlled for safety. A cascade control structure is commonly used. It offers a current-limiting function to ensure that the inductor current in the DC-DC converter series to the PV panel connector can be limited to the short-circuit current Isc, whereas other classic one-loop controllers can fail.

The controller in each control loop can be chosen by the designer. The classic controller, such as the PI controller, relies on the commonly used small-signal model. This type of controller requires only a small number of sensors. However, this results in a slow response. Moreover, to establish the small-signal model, a linearization technique that depends on the chosen operating point is used. This leads to a small-signal model that is fixed at the chosen operating point. When the system changes its operating point, the response may differ from the one selected. Although this is a drawback of the controller, it is still used due to its cost. In contrast, nonlinear controllers, such as flatness-based, Lyapunov-based, and passivity-based control, do not require linearization. Only differential equations are sufficient. In some cases, e.g., trajectory-tracking control, a large-signal average model is needed. However, the number of sensors increases compared to a PI control. But it offers high performance. Ultimately, everything depends on the user's affordability.

In this work, a boost converter is used as an MPPT converter, feeding a three-phase inverter connected to a three-phase grid. The inverter is assumed to be well controlled by a conventional PI controller, which is not presented in this paper [15]-[16]. The PI controller regulates the DC bus voltage across the DC bus capacitor, which is fed by the MPPT boost converter [14]. The contribution count on the MPPT control converter. The boost converter is controlled by a cascade control structure, and trajectory-tracking control is employed. A large-signal model is required [17].

2. Materials and Methods

The studied system is shown in Figure 1. The PV panels are connected to the PV capacitor C_{PV}, and a boost converter feeds energy to the output capacitor C_{DC}. Across C_{DC}, it is the output port, which is connected to the three-phase inverter feeding energy to a stiff grid. The model of the whole system under study will be presented in this section. Then, the controllers of the DC-DC boost converter, which will be a cascade control structure, are presented. The InC MPPT algorithm, which is well known to the audience, is omitted [18].

2.1 Hypotheses

In this study, the hypotheses are that

1) The three-phase grid is supposed to be a stiff grid.
2) The three-phase inverter is well controlled in the dq reference frame.
3) The DC bus voltage is regulated by the inverter, and beyond this paper
4) The uncertainty dynamics are slow compared to the other state variables.

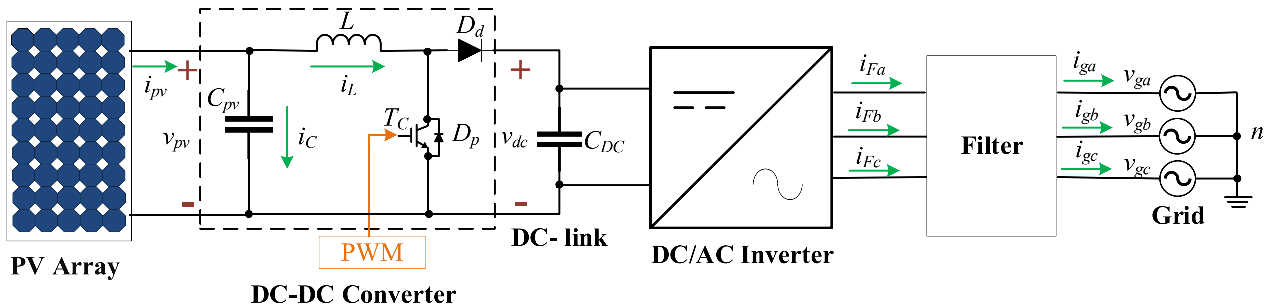

Figure 1. Three-phase inverter connecting to a grid fed by PV arrays with a boost converter MPPT [14].

2.1 PV modeling

The model of PV is chosen as in Figure 2 in MATLAB/Simulink, it is a classic one-diode model.

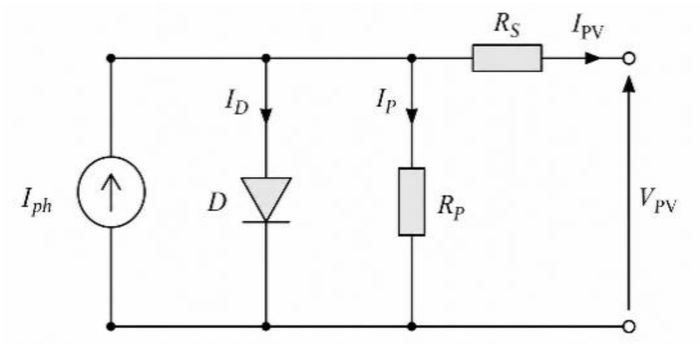

Figure 2. One diode PV model [18].

The current I_D relates the voltage across the diode voltage V_D where the diode ideally factor is one [18].

$$I_D = I_O\left(e^{\frac{qV_D}{kTN_{cell}}} - 1\right) \tag{1}$$

where q is the electron charge, I_o Diode saturation current, k Boltzmann constant, T temperature, N_{cell} Number of cells connected in series in a module.

The PV voltage also depends on the irradiation, temperature, the series resistance R_s, and the PV current. For the sake of simplicity, the temperature is fixed at 25 °C. The used PV panel is illustrated in Figure 3, where three irradiation levels are shown for the selected points at 0.8 kW/m^2, 0.4 kW/m^2, and 0.3 kW/m^2, as examples. The maximum power at each operating point is 5.66 kW, 2.81 kW, and 2.09 kW, respectively. The maximum power point can be found by varying the PV voltage.

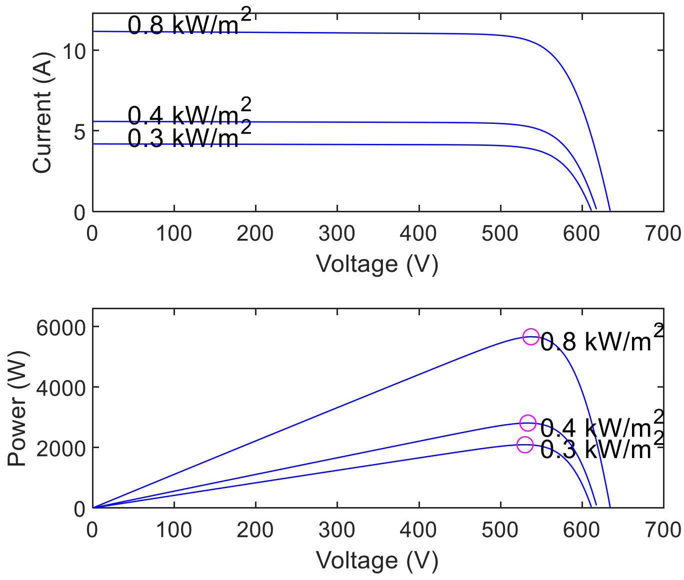

Figure 3 Used PV characteristic curves obtained from experiment in [14].

2.2 Boost converter modeling

The boost converter uses one inductor L, one controlled switch Tc, one diode Dd, and an output capacitor C_{DC}. Three state variables are the PV voltage across the PV capacitor (v_{pv}), the current (i_L) flowing through the boost inductor, and the voltage (v_{DC}) across the output capacitor C_{DC}. Note that the switch Tc is controlled by the duty cycle d associated with the switching command u. It is modeled as follows:

$$C_{pv}\frac{dv_{pv}}{dt} = i_{pv} - i_L + \underbrace{\left(i_{pv} - i_L\right)\sum_{k=1}^{\infty}(-1)^k\left(\frac{\Delta C_{pv}}{C_{pv}}\right)^k}_{I_{P1}} \tag{2}$$

$$L\frac{di_L}{dt} = v_{pv} - ri_L - (1-d)v_{DC} \\ \underbrace{-\left(\Delta ri_L - \left\{v_{pv} - ri_L - (1-d)v_{DC} - \Delta ri_L\right\}\sum_{k=1}^{\infty}(-1)^k\left(\frac{\Delta L}{L}\right)^k\right)}_{V_T} \tag{3}$$

$$C\frac{dv_{DC}}{dt} = (1-d)i_L - i_o + \underbrace{\left\{(1-d)i_L - i_o\right\}\sum_{k=1}^{\infty}(-1)^k\left(\frac{\Delta C}{C}\right)^k}_{I_{P2}} \tag{4}$$

where Δ represents the variation of the value of inductance, resistance, and capacitance, which are uncertainties of this converter. These uncertainties are assumed to be slow compared to the state variables, namely the inductor current and capacitor voltages.

2.3 Three-phase inverter

The three-leg inverter in Figure feeds the grid through an LCL filter. This three-phase inverter is modeled in the dq reference frame, where the inductances $L_{jd} = L_{jq} = L_j$, resistances $r_{jd} = r_{jq} = r_j$ for $j \in [F, d]$ represent two sets of inductances used as the LCL filter. The DC bus dynamics link the dq-reference-frame quantities to the DC bus voltage dynamics as follows:

$$\begin{cases} L_F\dfrac{di_{Fd}}{dt} = v_d - r_F i_{Fd} - v_{Fd} + \omega L_F i_{Fq} + \varphi_{Fd} \\ L_F\dfrac{di_{Fq}}{dt} = v_q - r_F i_{Fq} - v_{Fq} - \omega L_F i_{Fd} + \varphi_{Fq} \\ L_g\dfrac{di_{gd}}{dt} = v_{Fd} - r_g i_{gd} - v_{gd} + \omega L_g i_q + \varphi_{gd} \\ L_g\dfrac{di_{gq}}{dt} = v_{Fq} - r_g i_{gq} - v_{gq} - \omega L_g i_d + \varphi_{gq} \end{cases} \tag{5}$$

where

$$\varphi_{Fd} \\ = -\Delta r_F i_{Fd} + \omega\Delta L_F i_{Fq} \\ + \left(v_d - r_F i_{Fd} - v_{Fd} + \omega L_F i_{Fq} - \Delta r_F i_{Fd} + \omega\Delta L_F i_{Fq}\right)\sum_{k=1}^{\infty}(-1)^k\left(\frac{\Delta L_F}{L_F}\right)^k$$

$$\varphi_{Fq} \\ = -\Delta r_F i_q - \omega\Delta L_F i_{Fd} + \left(v_q - r_F i_{Fq} - v_{Fq} - \omega L_F i_{Fd} - \Delta r_F i_{Fq} - \omega\Delta L_{Fd}\right)\sum_{k=1}^{\infty}(-1)^k\left(\frac{\Delta L_F}{L_F}\right)^k$$

$$\varphi_{gd} = -\Delta r_g i_{gd} + \omega \Delta L_g i_{gq} + \left(v_{Fd} - r_g i_{gd} - v_{gd} + \omega L_g i_{gq} - \Delta r_g i_{gd} + \omega \Delta L_g i_{gq}\right) \sum_{k=1}^{\infty} (-1)^k \left(\frac{\Delta L_g}{L_g}\right)^k$$

$$\varphi_{gq} = -\Delta r_g i_q - \omega \Delta L_g i_{gd} + \left(v_{Fq} - r_g i_{gq} - v_{gq} - \omega L_g i_{gd} - \Delta r_g i_{gq} - \omega \Delta L_{gd}\right) \sum_{k=1}^{\infty} (-1)^k \left(\frac{\Delta L_g}{L_g}\right)^k$$

$$C_{DC} \frac{dv_{DC}}{dt} = i_o - i_{inv} + (i_o - i_{inv}) \sum_{k=1}^{\infty} (-1)^k \left(\frac{\Delta C_{DC}}{C_{DC}}\right)^k \tag{6}$$

Note that the dynamics of the voltages across the grid filter capacitor can be obtained in the same manner.

This inverter is controlled by a PI controller with a cascade control structure. The inner current-control loops for i_d and i_q. The outer DC bus voltage is controlled by another PI controller. The current reference i_{dref} links to the active power, which is generated from the DC bus voltage controller, while the current reference i_{qref}, linked to reactive power, is set to be zero in this study.

2.4 MPPT algorithm

The well-known incremental conduction method is chosen for this study. The output from the MPPT is the PV voltage across the PV capacitance [10], [18]. The step voltage for each operation can be chosen based on the specified change time; it is also adjustable.

2.5 Control algorithm

Cascade control is chosen for this study due to its features, including the ability to control and limit the inductor current for safety.

2.5.1. Outer-control loop

The outer loop is the energy stored in the PV capacitor

$$y = \frac{1}{2} C_{pv} v_{pv}^2 \tag{7}$$

It must follow its reference y_{ref}, the error $\varepsilon_y = y_{ref} - y$ is controlled to respond as a second-order system.

$$\dot{\varepsilon}_y + 2\zeta \omega_{ny} \varepsilon_y + \omega_{ny}^2 \int \varepsilon_y \, d\tau = 0 \tag{8}$$

The control parameters are the damping factor ζ and the angular frequency ω_{ny}.
Considering the variation of the energy of the PV capacitor

$$\dot{y} = p_{pv} - p_{iB} - p_{loss} \tag{9}$$

Where p_{iB} is the input power of the boost converter, p_{loss} is the losses due to uncertainties.

$$\dot{y}_{ref} + 2\zeta \omega_{ny} \varepsilon_y + \omega_{ny}^2 \int \varepsilon_y \, d\tau = \dot{y} = p_{pv} - p_{iB} - p_{loss} \tag{10}$$

The inductor current reference of the boost converter to force the energy $\varepsilon_y = 0$ can be obtained using

$$i_{Lref} = \frac{p_{iB}}{v_{pv}} = \frac{\left(p_{pv} - v_{pv} I_{P1_{est}}\right)}{v_{pv}} - \frac{\left(\dot{y}_{ref} + 2\zeta\omega_{ny}\varepsilon_y + \omega_{ny}^2 \int \varepsilon_y \, d\tau\right)}{v_{pv}} \tag{11}$$

Where the loss power $p_{loss} = v_{pv} I_{P1}$ is replaced by a product of current source $I_{p1_{est}}$ and the PV voltage. The current source $I_{p1_{est}}$ can be found using an observer.

2.5.2. Inner-control loop

The inner loop uses the same equation as for the energy loop for the current error $\varepsilon_i = i_{ref} - i_L$

$$\dot{\varepsilon}_i + 2\zeta\omega_{ni}\varepsilon_i + \omega_{ni}^2 \int \varepsilon_i \, d\tau = 0 \tag{12}$$

The duty cycle d is obtained thanks to the dynamic equation of the boost converter in (*3*)

$$\frac{di_{ref}}{dt} - \frac{\left(v_{pv} - r i_L - (1-d) v_{DC} - V_{T_{est}}\right)}{L} + 2\zeta\omega_{ni}\varepsilon_i + \omega_{ni}^2 \int \varepsilon_i \, d\tau = 0 \tag{13}$$

The voltage source $V_{T_{est}}$ replaces the uncertainties. $V_{T_{est}}$ can also be found using the observer.

2.5.3. Nonlinear observer

To address uncertainties, especially those that can lead to power loss, a nonlinear observer inspired by [19] is used.
Considering the system with a control input d and a vector of the slow uncertainties W

$$\begin{cases} \dot{x} = f(x, \gamma_i) + g_C d + g_u W \\ \dot{W} = 0 \end{cases} \tag{14}$$

Note that the controller for the inverter section is not treated here.The state variable for this system is defined as $x = [v_{PV} \; i_L \; v_{DC}]^T$ and $W = [I_{P1} \;\; V_T \;\; I_{P2}]^T$. Note that the controller for the inverter section does not treated here.

The estimated state variable x_{est} and the observer is given by

$$\begin{cases} \dot{x}_{est} = f(x, \gamma_i) + g_C d + g_u W_{est} - K_1 (x_{est} - x) \\ \dot{W}_{est} = K_2 (\dot{x}_{est} - \dot{x}) - \eta_1 (x_{est} - x) + \eta_2 \end{cases} \tag{15}$$

with

$$\eta_1 = g_u^T - K_1 K_2$$
$$\eta_2 = g_u^T \frac{\partial H_d}{\partial \tilde{x}} \tag{16}$$

Where $H_d = \frac{1}{2} C_{PV} \left(v_{PV} - v_{PVref}\right)^2 + \frac{1}{2} L \left(i_L - i_{Lref}\right) + \frac{1}{2} C_{DC} \left(v_{DC} - V_{DCref}\right)^2, \tilde{x} = x - x_{ref}, and\ K_1 > 0, K_2 > 0.$
Considering the dynamic error

$$\begin{cases} \dot{\xi}_x = \dot{x}_{est} - \dot{x} \\ \dot{\xi}_p = \dot{P}_{est} - \dot{P} \end{cases} \tag{17}$$

To evaluate that the operation of the observer is stable, a Lyapunov candidate function $V(x)$ is proposed

$$V(x) = H_d + \frac{\xi_x^T \xi_x}{2} + \frac{\xi_p^T \xi_p}{2} \tag{18}$$

With $V(0) = 0$ and $V(x) > 0$ for all $x \neq 0$. Its time derivative with the given dynamic error is negative. It means that the system is stable.

$$\dot{V}(x) < 0 \tag{19}$$

Regarding the control and observer algorithms, there are five sensors: two for voltage and three for current.

3. Results and Discussion

To validate the proposed control system, a simulation is done using MATLAB/Simulink. The power system is modeled using the Simscape toolbox and interfaces with a trigger block that contains the controllers. The block samples the signals with the same switching frequency F_s. The simulation parameters are given in Table 1.

Table 1. Parameters for the considered system.

Parameters for the system	**Values**
PV array, VoC, Isc	639.6 V, 13.93 A
DC bus voltage reference, V_DCref	650 V
Switching frequency, fs	10 kHz
Inductance, L,r for boost converter	2 mH, 0.01 ohm
Capacitance, C_{DC}	680 uF
Capacitance, C_{pv}	120 uF
Inductance, $L_{f1} - L_{f3}$ for grid inverter	1 mH
Inductance, $L_{g1} - L_{fg3}$ for grid inverter	0.6 mH
Capacitance, C_F for grid inverter	4.7 uF
Grid, Phase voltage	$220\sqrt{2}$ V

Table 2. Parameters for control.

Item	**Value**
ω_{ny}	250 rad/s
ω_{ni}	2500 rad/s
ζ	$\sqrt{2}/2$
Sampling time MPPT	100 ms
V_step	1 V
Observer gain K_1	10000
Observer gain K_2	0

3.2. Simulation results

Three scenarios are given in this section: the first describes normal operation with the known parameters, which are used in the controller algorithms. The second scenario is handled using approximate modeling of the series resistance in the boost converter inductance. For the first and second scenarios, the irradiance is given in Figure with a constant temperature of 25 °C. In the third scenario, the solar irradiance is fixed at 800 W/m^2 and the resistance parallel to C_{PV} is introduced and it changes from 10000 Ω to 1000 Ω at t = 0.1 s to demonstrate the observer function.

3.2.1. First scenario

The simulation results for the first scenario are shown in Figure 4 – Figure 6. The irradiation profile is shown in Figure. The solar irradiance starts at a constant of 400 W/m^2. Then, at t = 0.1 seconds, it steps to 800 W/m^2 and remains there for 0.1 seconds. Finally, it steps down to 300 W/m^2.

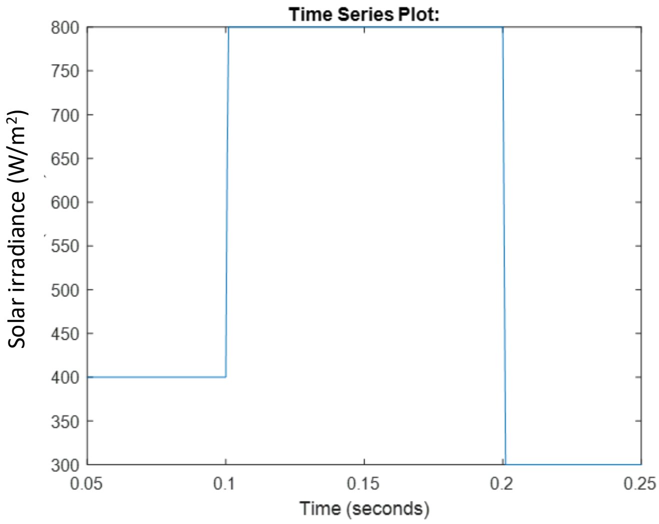

Figure 4. Solar irradiance for this study in W/m^2 units.

When the solar irradiance changes (see Figure 4), the MPPT provides the PV voltage reference to the boost converter controller to extract power. The trajectory-tracking control forces the energy y to its reference value in steady state. The response is shown in Figure 5. The trajectory is modeled as a first-order system with a chosen time constant that is lower than the MPPT sampling time. When the solar irradiance changes at t = 0.1 s, the actual energy changes accordingly. It is the same at t = 0.2 s, but in the opposite direction. The energy controller provides the current reference for the inner current loop, as detailed in Figure 6

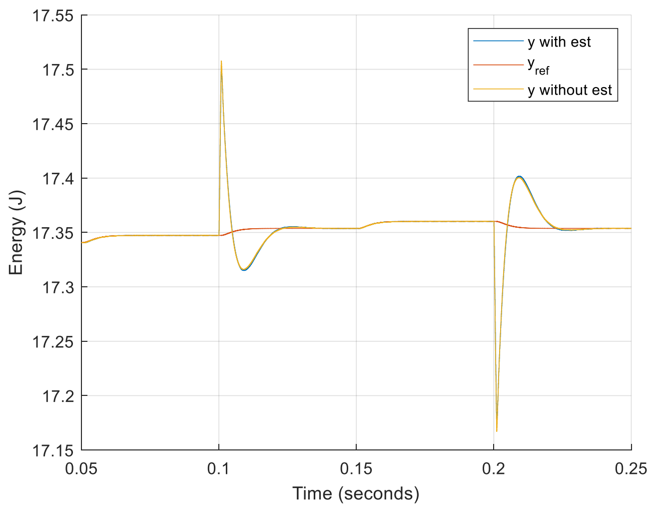

Figure 5 Energy in C_{PV} and its reference.

Figure 6 shows the waveforms on the AC side, where the three-phase inverter is fed by the DC bus connected to the stiff grid. In this study, active power is controlled via the d-axis current, while the reactive power is zero (i.e., $i_q = 0$). The responses of V_{DC} and the AC current are shown, with the inverter controlled by PI control as stated in the hypotheses.

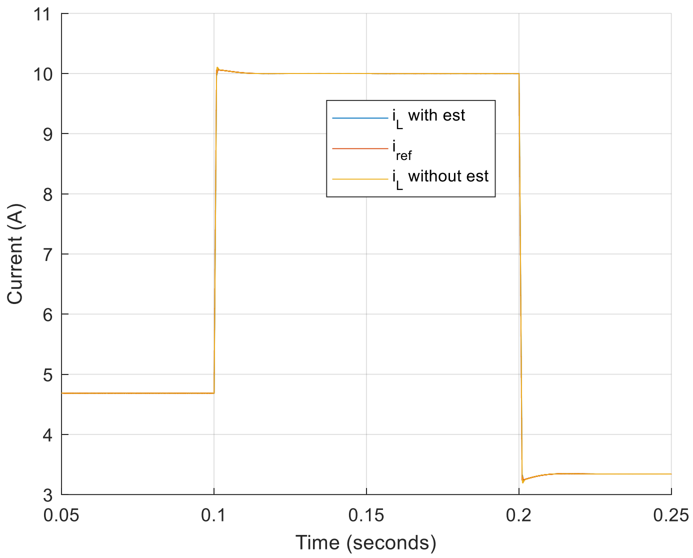

Figure 6 Inductor current and its reference.

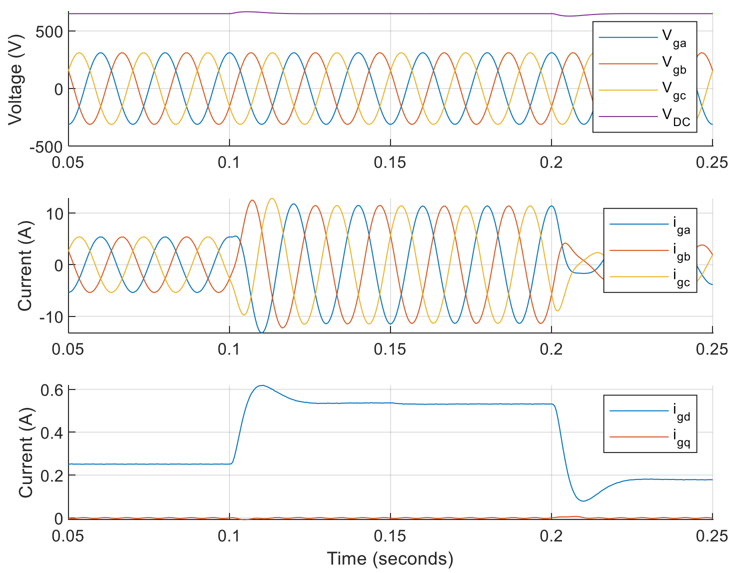

Figure 7. Waveforms of the output voltage V_{DC}, the grid voltage, the current feeding the grid, and the grid current in dq reference frame.

3.2.1. Second scenario

In this scenario, the series resistance of the inductor in the boost converter is abruptly changed from 10 mΩ to 20 Ω at t = 0.15 seconds, as shown in Figure 8. Because the controller includes an integral term, it can drive the error to zero. However, with information from the observer, the response is faster and can acquire more energy from the solar panels.

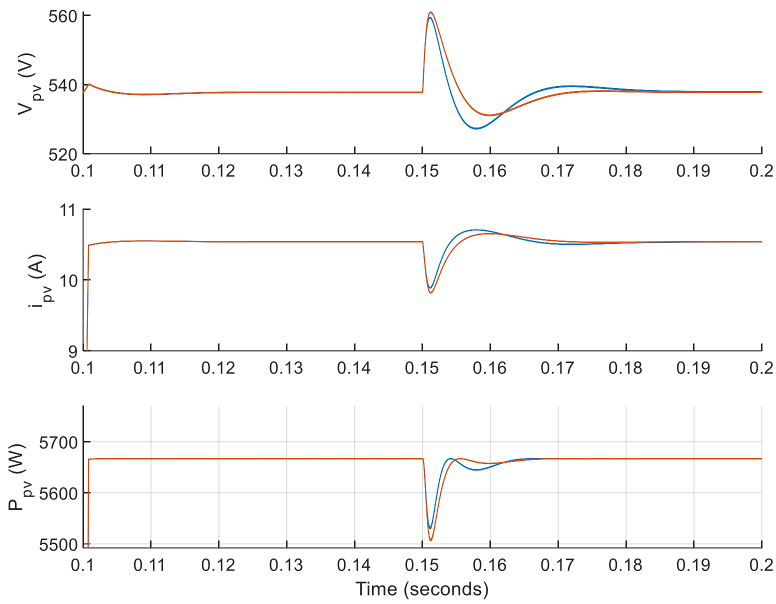

Figure 8 Abrupt change of the series resistance at t = 0.15 from 10 mΩ to 20 Ω. The blue line is obtained with the observer, and the orange line without the observer.

3.2.3. Third scenario

In this test, a resistor is added in parallel with the PV capacitor to represent losses due to the capacitor and other related losses. The results, shown in Figure 9 and Figure 10, are obtained from the system with and without the proposed observer. To draw power from the PV panels, the energy in maj C indice maj P maj V is controlled according to the MPPT command, which is the PV capacitor voltage shown in Fig. 9. The PV voltage, PV current, and PV power are shown in Fig. 10. It is clear that with the observer, the influence of the resistance is reduced.

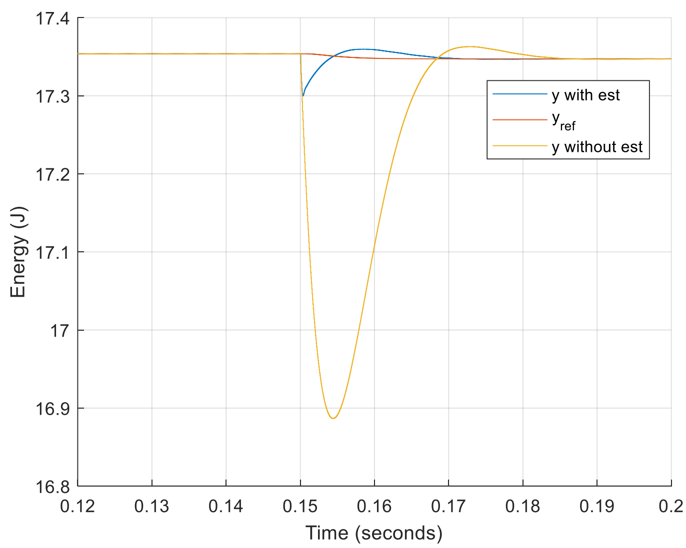

Figure 9 Energy in C_{PV} and its reference when there is an abrupt change of the parallel resistance of C_{PV} at t = 0.15 from 10000 Ω to 1000 Ω. The blue line is obtained with the observer, and the orange line without the observer.

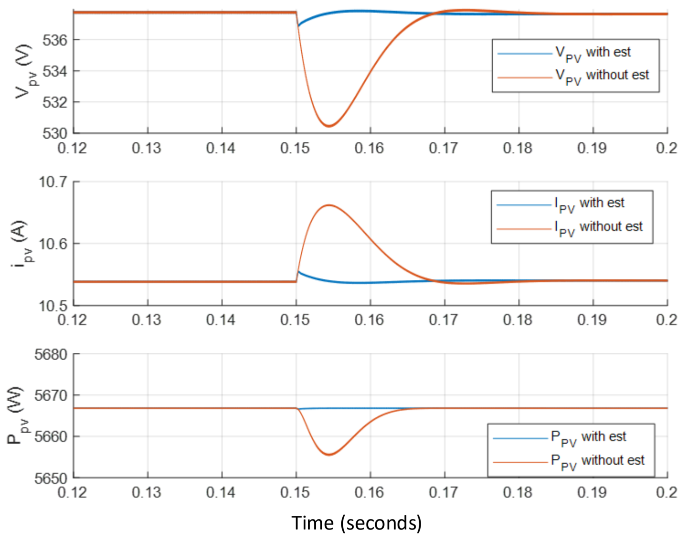

Figure 10 A sudden change of the parallel resistance of C_{PV} at t = 0.15 from 10000 Ω to 1000 Ω. The blue line is obtained with the observer, and the orange line without the observer.

Without the observer, the PV capacitor can be as low as 2 μF for this application, where the system remains stable. However, ripples on the PV voltage are higher than with higher capacitance.

4. Conclusions

This paper presents a PV grid-connected system. The hypotheses are that 1) the three-phase grid is stiff, 2) the three-phase inverter is well controlled in the dq reference frame, 3) the DC bus voltage is regulated by the inverter, and 4) the uncertainty dynamics are slow compared to the other state variables. We focus on the DC-DC converter, which receives its command from the InC MPPT and feeds the DC bus, which is regulated by the three-phase inverter connected to a three-phase grid. We propose using a cascade control structure to draw power from PV panels via the MPPT. The control algorithm is equipped with a disturbance observer to account for power losses due to uncertainties in the system between the PV panel and the inverter. Uncertainties due to passive elements such as capacitance, inductance, and parasitic resistance affect the performance of the MPPT. However, inductance and capacitance are closely related to ripples in the current and voltage, respectively. Parasitic resistances most influence the performance of the MPPT. With the proposed control algorithm with observer, good results are achieved, with less influence from losses. The controlled PV voltage improves by about 1.3035% when the observer is used. The presence of this influence is only about 11 W lower. Therefore, the observer may allow reducing the number of sensors to further benefit.

5. Acknowledgements

The schematic diagram was generated by ChatGPT.

References

[1] Burhanuddin, J.; Ishak, A. M.; Hasim, A. S. A.; Burhanudin, J.; Dardin, S. M. F. B. S. M.; Ibrahim, T. A Review of Wave Energy Converters in the Southeast Asia Region. IEEE Access 2022, 10, 125754–125771.

[2] Lu, H.; et al. A Capacitor-Assisted MPPT Buck-Boost Interface for Low-Internal-Resistance Energy Harvesting. IEEE Trans. Power Electron. 2026. https://doi.org/10.1109/TPEL.2026.3692751.

[3] Liu, Y.; et al. A Wide-Dynamic-Range Photovoltaic Energy Harvester With Adaptive Power-Scalable MPPT Control and Direct Power-to-Digital Converter. IEEE J. Solid-State Circuits 2026. https://doi.org/10.1109/JSSC.2026.3675521.
[4] Qi, P.; Zhang, H.; Chen, A.; Zhang, G.; Cheng, C.; Wang, J. Model-Free Predictive Control Strategy for Photovoltaic Grid-Forming Inverters with MPPT and Power-Dispatch Capabilities. Chin. J. Electr. Eng. 2026. https://doi.org/10.23919/CJEE.2026.000027.
[5] Lima, A. C.; Schardong, C.; Bellinaso, L. V.; Tambara, R. V.; Michels, L. Direct Adaptive Control of Photovoltaic Boost Converters With Ultra-Low Input Capacitance. IEEE Open J. Ind. Appl. 2026, 7, 547–562.
[6] Corti, F.; Lozito, G. M.; Meshram, V. S.; Reatti, A. Toward Fast-Tracking in Solar Vehicles: Neural MPPT and Supercapacitor Synergy. IEEE Trans. Ind. Electron. 2026. https://doi.org/10.1109/TIE.2026.3692871.
[7] Nautiyal, D. C.; Tripathi, S.; Sahu, H. S. Prediction and Estimation of Maximum Power of a PV String Under Partial Shading Conditions. IEEE Trans. Ind. Appl. 2026. https://doi.org/10.1109/TIA.2026.3661377.
[8] Yang, H.; et al. Integrated Solar Cell-Supercapacitor for Enhanced Power Output of PV Arrays under Partial Shading. IEEE Trans. Ind. Appl. 2026. https://doi.org/10.1109/TIA.2026.3683341.
[9] Prajapat, A. K.; Simon, S. P.; Nayak, P. S. R.; Sundareswaran, K.; Padhy, N. P. Distributed MPPT in Dual-Faced Open Cubic PV System Using K-Means Clustering. IEEE J. Photovolt. 2026. https://doi.org/10.1109/JPHOTOV.2026.3673773.
[10] Abdourraziq, M. A.; Maaroufi, M.; Ouassaid, M. A New Variable Step Size INC MPPT Method for PV Systems. In Proceedings of the 2014 International Conference on Multimedia Computing and Systems (ICMCS); Marrakech, Morocco, 2014; pp 1563–1568. https://doi.org/10.1109/ICMCS.2014.6911212.
[11] Mahmoud, Y.; Xiao, W.; Zeineldin, H. H. A Simple Approach to Modeling and Simulation of Photovoltaic Modules. IEEE Trans. Sustain. Energy 2012, 3 (1), 185–186.
[12] Mahmoud, Y.; El-Saadany, E. Accuracy Improvement of the Ideal PV Model. IEEE Trans. Sustain. Energy 2015, 6 (3), 909–911.
[13] Spertino, F.; Sumaili, J.; Andrei, H.; Chicco, G. PV Module Parameter Characterization from the Transient Charge of an External Capacitor. IEEE J. Photovolt. 2013, 3 (4), 1325–1333.
[14] Prasatsap, U.; Jamshidpour, E.; Phattanasak, M.; Somkun, S. Study of MPPT Performance of Two-Stage Photovoltaic Grid-Connected Inverter. In Proceedings of the 2024 International Conference on Materials and Energy: Energy in Electrical Engineering (ICOME-EE); Bangkok, Thailand, 2024; pp 1–4. https://doi.org/10.1109/ICOME-EE64119.2024.
[15] Srita, S.; Somkun, S. Implementation and Performance Comparison of Harmonic Mitigation Schemes for Three-Phase Grid-Connected Voltage-Source Converter under Grid Voltage Distortion: HiL and Experimental Validation. AEU Int. J. Electron. Commun. 2023, 161, 154552.
[16] Srita, S.; Somkun, S.; Kaewchum, T.; Rakwichian, W.; Zacharias, P.; Kamnarn, U.; et al. Modeling, Simulation and Development of Grid-Connected Voltage Source Converter with Selective Harmonic Mitigation: HiL and Experimental Validations. Energies 2022, 15 (7).
[17] Renaudineau, H.; Houari, A.; Martin, J.-P.; Pierfederici, S.; Meibody-Tabar, F.; Gerardin, B. A New Approach in Tracking Maximum Power under Partially Shaded Conditions with Consideration of Converter Losses. Sol. Energy 2011, 85 (11), 2580–2588.
[18] Kacimi, N.; Idir, A.; Grouni, S.; Boucherit, M. S. Improved MPPT Control Strategy for PV Connected to Grid Using IncCond-PSO-MPC Approach. CSEE J. Power Energy Syst. 2023, 9 (3), 1008–1020.

[19] Renaudineau, H.; Martin, J.-P.; Nahid-Mobarakeh, B.; Pierfederici, S. DC–DC Converters Dynamic Modeling With State Observer-Based Parameter Estimation. IEEE Trans. Power Electron. 2015, 30 (6), 3356–3363.

Techno-Economic Assessment of Grid-Connected and Stand-Alone Hybrid Renewable Energy Systems with Battery and Hydrogen Storages: A Case Study of Southern Thailand

Atikan Junnunto[1], Jompob Waewsak[1,2*], Jerawat Sopajarn[1], Ruamporn Nikhom[1], Weerasak Chaichan[3]

[1] Faculty of Engineering, Thaksin University (Phatthalung Campus), Phatthalung 93210, Thailand
[2] Solar and Wind Energy Research Laboratory (SWERL), Research Center in Energy and Environment (RCEE), Thaksin University (Phatthalung Campus), Phatthalung 93210, Thailand
[3] Faculty of Engineering and Technology, Rajamangala University of Technology Srivijaya (Trang Campus), Trang, Thailand
*Correspondence: jompob@tsu.ac.th

Abstract

This study conducts a comprehensive techno-economic evaluation of grid-connected (on-grid) and standalone (off-grid) hybrid renewable energy systems (HRES) designed for a large-scale electricity demand site in Songkhla Province, southern Thailand, using the HOMER Pro simulation software. Both configurations include photovoltaic (PV) generation, battery energy storage systems (BESS) with sonnenBatterie units, a hydrogen fuel cell (FC) generator fueled by electrolytically produced and stored hydrogen, and a power converter. The on-grid configuration also incorporates bidirectional grid interaction. Key performance indicators such as net present cost (NPC), levelized cost of energy (LCOE), PV penetration, surplus electricity, CO_2 emissions, and system reliability (unmet load) were evaluated and compared across four simulation scenarios using HOMER Pro. The on-grid system achieves an LCOE of \$0.117/kWh with a total NPC of \$4.50 billion, whereas the standalone system results in an LCOE of \$0.232/kWh and an NPC of \$6.42 billion, underscoring the significant economic cost of complete energy independence. However, the standalone system achieved nearly zero CO_2 emissions owing to its lack of grid dependence. These findings provide valuable insights for microgrid planners, policymakers, and renewable energy investors in tropical regions with high solar irradiance.

Keywords: renewable energy; hydrogen fuel cell; battery energy storage; techno-economic assessment

1. Introduction

The global energy transition from fossil-fuel-dependent infrastructure to sustainable, low-carbon alternatives is accelerating owing to climate commitments, energy security concerns, and the rapidly falling costs of renewable technologies [1]. In Southeast Asia, Thailand has emerged as one of the region's leaders in renewable energy deployment, driven by the Alternative Energy Development Plan (AEDP), which targets 30% renewable energy in its final energy consumption by 2037 [2]. The southern provinces of Thailand, including Songkhla, benefit from high annual solar irradiance, making photovoltaic systems particularly attractive for both utility-scale and distributed energy applications [3].

Hybrid renewable energy systems (HRES), which combine multiple generation sources with energy storage, offer significant advantages over single-source systems, including improved reliability, reduced dependence on fossil fuels, and enhanced economic performance [4]. When integrated with battery energy storage systems (BESS) and hydrogen-based long-duration storage, HRES can address the inherent variability of solar power and provide dispatchable capacity during periods of low irradiance [5]. The integration of electrolyzer, hydrogen storage tanks, and fuel cells—collectively termed the power-to-hydrogen-to-power (P2H2P) pathway—enables the conversion of surplus renewable electricity to hydrogen, which can be stored and reconverted to electricity on demand [6].

The choice between grid-connected and standalone microgrid operations involves significant trade-offs. Grid-connected systems benefit from the ability to purchase deficit power and sell surplus generation, thereby reducing the required storage capacity and capital investment [7]. Standalone systems, while requiring larger storage and generation capacity, offer complete energy independence, eliminate exposure to grid electricity prices, and in the case of purely renewable operation, achieve near-zero lifecycle emissions [8]. This trade-off is particularly relevant for large industrial and commercial sites, remote communities, and critical infrastructure in developing economies [9].

HOMER Pro (Hybrid Optimization of Multiple Energy Resources) is widely recognized as an industry-standard tool for simulating and optimizing distributed energy systems [8]. Originally developed at the US National Renewable Energy Laboratory (NREL), HOMER Pro uses a time-step simulation approach to evaluate system performance across an entire year, enabling an accurate techno-economic analysis of complex hybrid configurations [9]. Its ability to handle sensitivity analyses, multi-year cash flow projections, and diverse component libraries makes it the tool of choice for both academic research and commercial feasibility studies [12].

This study evaluated four simulation scenarios generated by HOMER Pro for a site in Taling Chan, Chana District, Songkhla, Thailand: two on-grid scenarios and two standalone scenarios, each representing distinct system sizing configurations. The primary contributions of this study are as follows: (1) a detailed comparative techno-economic analysis of on-grid versus standalone HRES incorporating hydrogen storage at scale; (2) quantification of the economic and emissions trade-offs specific to the Thai southern region solar resource; and (3) practical insights for system designers and policymakers on the viability of hydrogen-integrated microgrids in tropical climates.

Prior HOMER-based studies have demonstrated that renewable hybrid systems reduce LCOE significantly versus diesel alternatives [10,11,13]. The P2H2P pathway provides long-duration storage flexibility but remains economically challenged by current electrolyzer and fuel cell costs [14], a finding corroborated by this study.

2. Materials and Methods

2.1 Study Area and Resource

The study site was located at Taling Chan, Chana District, Songkhla Province, Thailand (coordinates: 6°57.7'N, 100°46.1'E; Figure 1). The site is situated in the southern peninsula of Thailand, a region characterized by a tropical monsoon climate with distinct wet and dry seasons [21]. The solar resource was evaluated using NASA Surface Meteorology and Solar Energy (SSE) data imported into HOMER Pro, yielding a capacity factor of 16.1% for fixed-tilt Canadian Solar PV modules, consistent with the measured data for this latitude and climate zone [22].

The electrical load profile represents a large-scale demand node requiring 8,345,450 kWh/day (on-grid scenarios) with a peak demand of 749,969 kW and 4,841,273 kWh/day (standalone scenarios) with a peak of 519,714 kW. The difference in load profiles between the on-grid and standalone scenarios reflects the different demand nodes analyzed in the respective simulations. The dispatch strategy employed is the HOMER Cycle Charging, a widely used strategy for systems with fossil fuel or fuel cell backup that prioritizes charging storage from surplus renewable production before satisfying loads [8].

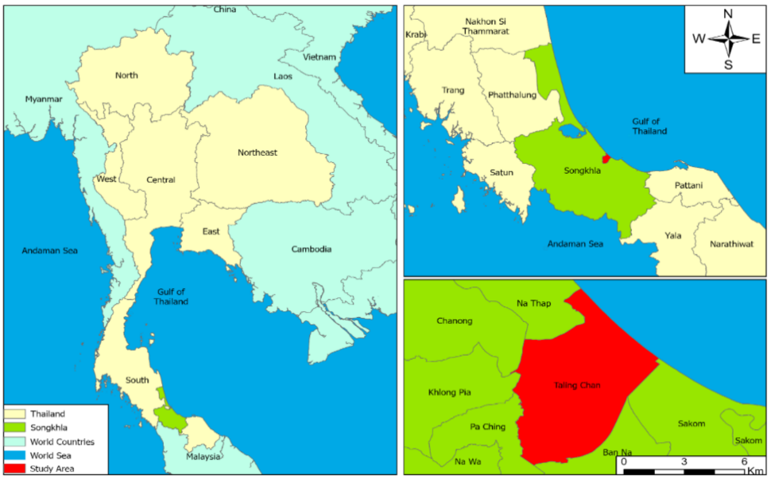

Figure 1. Study area map.

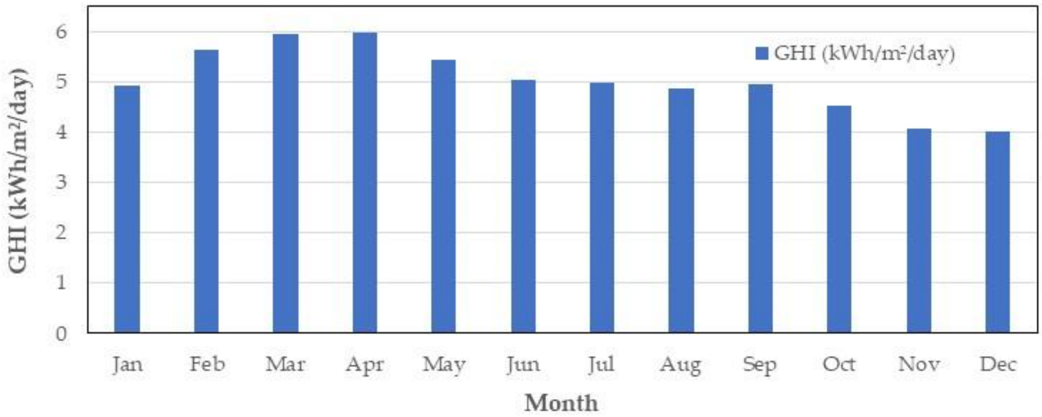

Figure 2. Global horizontal irradiation profile of study area.

Figure 3. Temperature profile of study area.

2.2 System Architecture

Both system types share a common component architecture consisting of the following elements: (1) a Canadian Solar photovoltaic array, (2) a sonnenBatterie 8 kW-12 kWh eco 12 battery energy storage system, (3) a hydrogen fuel cell (FC) generator rated at 200,000 kW, (4) a 200,000 kW PEM electrolyzer for hydrogen production, (5) a 100,000 kg hydrogen storage tank, and (6) a generic large-scale DC-AC power converter. The on-grid configuration additionally includes a grid connection with a capacity of 999,999 kW, enabling a bidirectional energy exchange at prevailing tariff rates. Figure 4 illustrates the system schematic generated by the HOMER Pro. The standalone system excludes grid connectivity, requiring the system to meet all load demands through internal generation and storage.

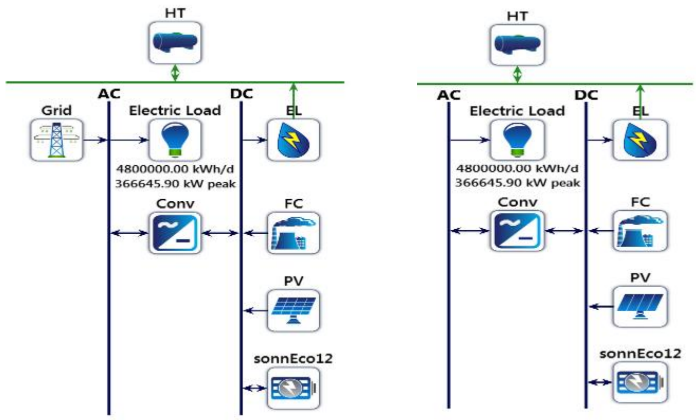

Figure 4. HOMER Pro system schematic for the on-grid configuration and standalone configuration.

Table 1. System architecture comparison: on-grid vs. stand-alone configurations.

Component	On-Grid System	Standalone System	Unit
PV Array (Canadian Solar)	1,600,000	3,831,933	kW
Fuel Cell Generator (FC)	200,000	200,000	kW
Battery Storage (sonnenBatterie eco 12)	148,148 strings (1,777,776 kWh)	423,819 strings (5,085,828 kWh)	strings / kWh
System Converter	549,969	373,806	kW
Grid Connection	999,999	N/A	kW
Electrolyzer	200,000	200,000	kW
Hydrogen Tank	100,000	100,000	kg
Dispatch Strategy	HOMER Cycle Charging	HOMER Cycle Charging	-

2.3 Component Specifications

The PV system uses Canadian Solar modules with a specific yield of 1,406 kWh/kW/year and LCOE of $0.0414/kWh. The capital costs are $0.70/W (on-grid: $1.12 billion for 1.6 GW; standalone: $2.68 billion for 3.83 GW). The fuel cell system operates at a mean electrical efficiency of 50 % with a specific hydrogen consumption of 0.06 kg/kWh. The electrolyzer achieved a specific consumption of 46.4 kWh/kg of hydrogen produced. The sonnenBatterie system operates at a bus voltage of 240 V with an expected life of 15 years and a storage wear cost of $0.0162/kWh. The hydrogen tank provides 16.7 hrs of autonomy at the rated capacity. The financial parameters include a 25-year project lifetime, 7% nominal discount rate, 3% expected inflation rate, and a resulting 3.9% real interest rate.

Table 2. Component capital and operating cost parameters.

Component	Capital Cost	O&M Cost ($/yr)	Replacement Cost
PV (per kW)	$0.70/W	~$14/kW/yr	None (25-yr life)
Fuel Cell (200 MW)	$600M	$5.18M (on-grid) $124,000 (standalone)	None within 25 yr (on-grid)
sonnenBatterie eco 12	$267M (on-grid) $763M (standalone)	$5.33M / $15.3M	Year 15
Converter	$412M (on-grid) $280M (standalone)	$8.25M / $5.61M	Year 15
Electrolyzer (200 MW)	$400M	$4.00M	Year 15 ($364M)
Hydrogen Tank (100,000 kg)	$41.0M	$410,000	None

3. Results and Discussion

3.1 On-Grid System Results

The on-grid system (Scenario OG-1, detailed simulation report) achieves a total NPC of $4.503 billion with an LCOE of $0.117/kWh over the 25-year project lifetime. The total annual electrical production reached 3,437,424,497 kWh/yr, with PV contributing 65.5%, grid purchases 28.2%, and the fuel cell supplying the remaining 6.37%. The annual electrical consumption is 1,752,000,000 kWh/yr for the primary AC load, with 609,544,578 kWh/yr consumed by the electrolyzer for hydrogen production and 685,908,574 kWh/yr sold back to the grid [35].

The excess electricity amounts to 312,050,382 kWh/yr, and there is zero unmet load, confirming full system reliability. The PV penetration was 128%, indicating that PV alone produced more energy than required by the primary load on an annual basis, with the surplus directed to the electrolyzer and grid [36]. The fuel cell operates at a capacity factor of 12.5%, running for 1,296 h per year with 753 starts. The battery system achieved 0.800 equivalent full cycles per year, reflecting very light utilization owing to heavy grid dependence.

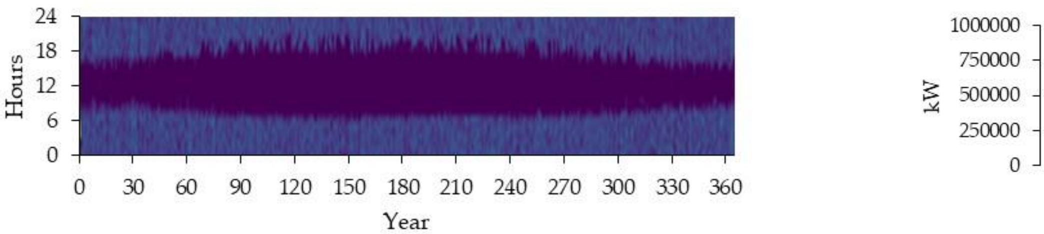

Figure 5. PV output profile (kW) over the year

Table 3. On-grid system: net present cost summary by component.

Component	Capital ($)	Operating ($)	Replacement ($)	Salvage ($)	Total NPC ($)
Electrolyzer	$400M	$63.3M	$203M	-$46.3M	$620M
Fuel Cell (FC)	$600M	$82.0M	$0	-$95.8M	$586M
Converter	$412M	$130M	$233M	-$53.0M	$723M
Grid	$0	$586M	$0	$0	$586M
Hydrogen Tank	$41.0M	$6.48M	$0	$0	$47.5M
PV	$1.12B	$354M	$0	$0	$1.47B
Battery (sonnen)	$267M	$84.4M	$151M	-$34.3M	$467M
System Total	$2.84B	$1.31B	$587M	-$229M	$4.503B

3.2 Standalone System Results

The standalone system (Scenario SA-1) results in a substantially higher NPC of $6.423 billion and LCOE of $0.232/kWh, representing a 99% increase in LCOE compared with the on-grid configuration. This increase is primarily driven by the need for a much larger PV array (3,831,933 versus 1,600,000 kW) and battery storage system (5,085,828 versus 1,777,776 kWh) to ensure supply reliability without a grid backup. The system capital expenditure (CAPEX) is $4.77 billion compared to $2.84 billion for the on-grid case.

The total annual production was 5,394,307,919 kWh/yr, of which PV contributed 99.9% (5,388,617,995 kWh/yr), and the fuel cell supplied only 0.105% (5,689,923 kWh/yr). The dramatically reduced fuel cell utilization in the standalone case—only 31 h of operation per year versus 1,296 h in the on-grid case—reflects the much larger PV array's ability to meet nearly all demand directly and via battery storage [37]. The excess electricity generation is 3,371,432,371 kWh/yr, representing a massive oversizing that is economically necessary to ensure winter-month and night-time reliability without grid backup.

A minor unmet load of 534,252 kWh/yr (0.030% of the annual demand) and a capacity shortage of 1,126,318 kWh/yr were observed in the standalone system, indicating near but imperfect reliability. This trade-off between the system size and perfect reliability is a fundamental challenge in off-grid system design [38]. The battery system in the standalone case operates at 215 equivalent full cycles per year (0.588 cycles/day), far more intensively than that in the on-grid case, which impacts the battery lifetime and replacement costs.

Notably, the standalone system achieved zero CO2 emissions from grid electricity, as it drew no power from the national grid. Minor emissions from the fuel cell (19,801 kg/yr NOx from 341,395 kg of hydrogen consumption) are negligible compared to the on-grid system's grid-attributable emissions of 178,609,602 kg CO_2/yr [39].

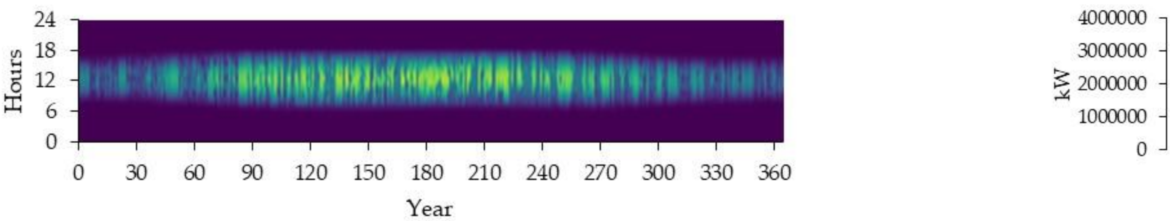

Figure 6. PV output profile for standalone system.

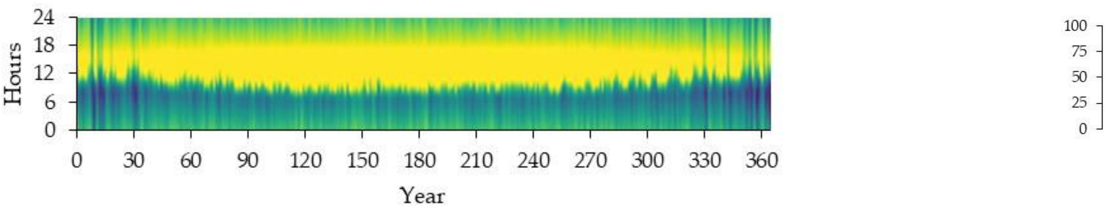

Figure 7. Battery state of charge (%) over the simulation year, standalone system.

Table 4. Standalone system: annual energy production and consumption summary.

Component	Annual Value (kWh/yr)	Percentage (%)
PV Production	5,388,617,995	99.9
Fuel Cell Production	5,689,923	0.105
Total Production	5,394,307,919	100
AC Primary Load	1,751,465,748	99.1 of consumption
Electrolyzer Consumption	15,842,531	0.896 of consumption

Excess Electricity	3,371,432,371	-
Unmet Load	534,252	0.030
Capacity Shortage	1,126,318	-

Table 5. Standalone system: net present cost summary by component.

Component	Capital ($)	Operating ($)	Replacement ($)	Salvage ($)	Total NPC ($)
Electrolyzer	$400M	$63.3M	$203M	-$46.3M	$620M
Fuel Cell (FC)	$600M	$1.96M	$0	-$206M	$396M
Converter	$280M	$88.7M	$158M	-$36.1M	$491M
Hydrogen Tank	$41.0M	$6.48M	$0	$0	$47.5M
PV	$2.68B	$848M	$0	$0	$3.53B
Battery (sonnen)	$763M	$241M	$431M	-$98.1M	$1.34B
System Total	$4.77B	$1.25B	$792M	-$386M	$6.423B

3.3 Comparative Analysis

3.3.1 Economic Performance

Table 6 summarizes key economic indicators. The on-grid LCOE ($0.117/kWh) is 98% lower than the standalone ($0.232/kWh), consistent with the literature [40]. The standalone CAPEX ($4.77B) is 68% higher, driven by a 2.4× larger PV array and 2.9× more battery storage. Seasonal grid exports (April–July) provide an economic lever unavailable to standalone systems [41].

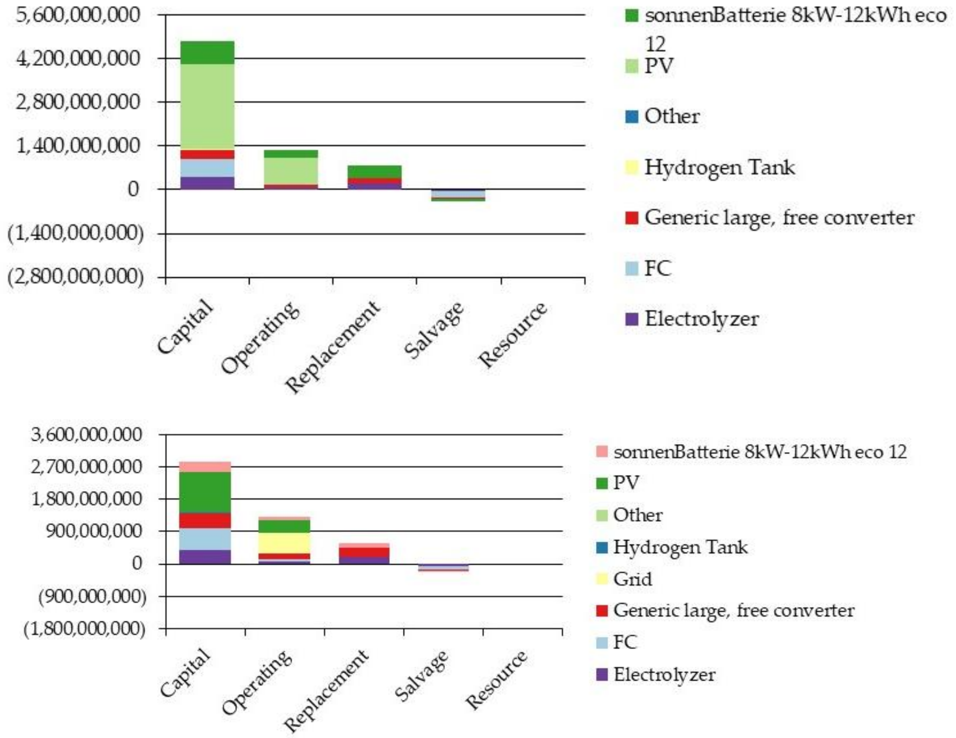

Figure 8. Comparative bar chart of annualized costs by component for on-grid vs off-grid.

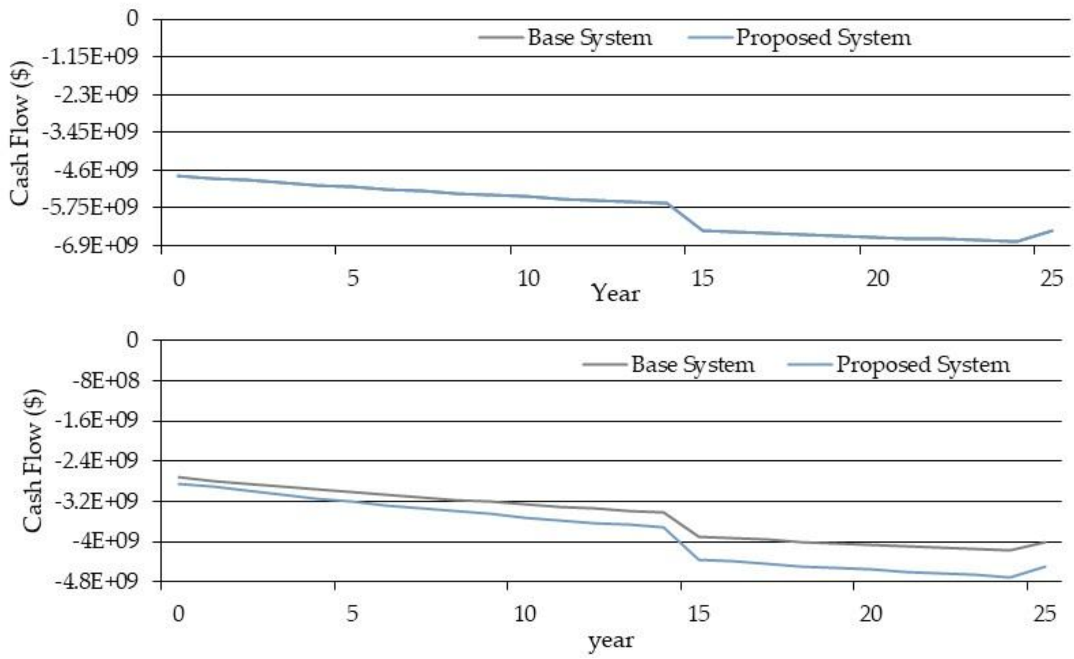

Figure 9. Cumulative discounted cash flow comparison.

Table 6. Comparative summary: on-grid vs. standalone system key metrics.

Metric	On-Grid System	Standalone System	Unit
Total Net Present Cost (NPC)	$4.503B	$6.423B	USD
Levelized Cost of Energy (LCOE)	$0.117	$0.232	$/kWh
CAPEX	$2.84B	$4.77B	USD
Annual OPEX	$105M	$105M	USD/yr
PV Array Capacity	1,600,000	3,831,933	kW
Battery Storage Capacity	1,777,776	5,085,828	kWh
PV Penetration	128%	308%	-
Annual PV Production	2,249,984,853	5,388,617,995	kWh/yr
Fuel Cell Hours of Operation	1,296	31.0	hrs/yr
Excess Electricity	312,050,382	3,371,432,371	kWh/yr
Unmet Load	0	534,252	kWh/yr
CO2 Emissions (grid-attributed)	178,609,602	0	kg/yr
H2 Fuel Consumption	13,135,256	341,395	kg/yr
Battery Annual EFCs	0.800	215	cycles/yr
Battery Autonomy	8.00	22.9	hr
Simple Payback	N/A	N/A	yr
Return on Investment (ROI)	-24.6%	N/A	-

3.3.2 Environmental Performance

The environmental implications of these two configurations differ substantially. The on-grid system, while economically superior, relies on grid purchases of 968,518,704 kWh/year. Using Thailand's average grid emission factor of approximately 0.5163 kg CO_2/kWh [23], these grid purchases resulted in attributed CO2 emissions of 178,609,602 kg/yr. Additionally, the grid-connected system consumes 13,135,256 kg of hydrogen annually through the fuel cell, which, although internally produced via electrolysis, involves conversion losses.

The standalone system achieved near-zero lifecycle CO_2 emissions, with zero grid-attributed emissions and only minor NOx emissions from the fuel cell (19,801 kg/yr). This is a critical advantage for projects with sustainability mandates, carbon neutrality targets or emissions-based regulatory compliance requirements. The standalone configuration is particularly relevant for Thailand's commitments under the Paris Agreement, which targets a 40% reduction in greenhouse gas emissions below 2005 levels by 2030 [24].

Table 7. Annual emissions comparison: on-grid vs. standalone system.

Pollutant	On-Grid System (kg/yr)	Standalone System (kg/yr)
Carbon Dioxide (CO_2)	178,609,602	0
Carbon Monoxide (CO)	85,379	2,219
Unburned Hydrocarbons (UHC)	9,457	246
Particulate Matter (PM)	6,436	167
Sulfur Dioxide (SO_2)	774,352	0
Nitrogen Oxides (NOx)	1,140,542	19,801

3.3.3 System Reliability and Storage Analysis

The system reliability, measured by the unmet load fraction, was 100% for the on-grid system and 99.97% for the standalone system. While both configurations achieve high reliability, the zero unmet load of the on-grid system does not require the massive oversizing required in the standalone case. The standalone system's 3,371,432,371 kWh/yr of excess electricity—approximately 190% of the total annual consumption—represents a significant resource that could potentially be monetized through hydrogen export, district heating, or industrial processes if such offtake arrangements were available [44].

The negative ROI of -24.6% for the on-grid system (as computed from the base case comparison) reflects that the proposed battery addition in the HOMER proposal framework does not improve the base case operating cost, a finding consistent with the high capital intensity of large-scale BESS at current prices. However, the simulation demonstrated that the hydrogen-integrated system provides a technically robust and emissions-conscious solution. As hydrogen production costs continue to decline with electrolyzer scale-up and green hydrogen policy support, the economic case for P2H2P integration will be strengthened [49].

The near-zero emissions profile of the standalone system is its most compelling attribute. For applications where carbon neutrality is a prerequisite, such as international corporate sustainability requirements, green bond financing, or regulatory compliance, an emissions-free standalone configuration may justify its higher cost. The 178,609,602 kg/yr CO_2 attributed to the on-grid system's grid purchases represents a significant carbon liability that may carry increasing financial consequences under evolving carbon pricing mechanisms in Thailand and internationally [50].

Several limitations of this analysis merit acknowledgment. First, the load profile assumptions were based on representative demand curves and may not perfectly reflect the actual site conditions. Second, the cycle charging dispatch strategy of HOMER Pro, while standard, may not represent the optimal dispatch for this specific configuration; other strategies, such as load-following or predictive control, could yield different results. Third, the hydrogen subsystem costs used reflect current market prices; with ongoing reductions in electrolyzer costs projected at 5–10% annually [25], the long-term economics of hydrogen integration will improve. Finally, the land area requirements for a 3.8 GW PV array were not analyzed here but would be a critical constraint in practice.

4. Conclusion

This study presents a techno-economic and environmental comparison of grid-connected and standalone hybrid renewable energy systems incorporating PV, battery storage, and hydrogen fuel cell technology for a large-scale site in Songkhla Province, Thailand, using HOMER Pro. The on-grid configuration achieves an LCOE of \$0.117/kWh and NPC of \$4.503 billion, significantly outperforming the standalone system (\$0.232/kWh, \$6.423B NPC), enabled by grid energy arbitrage and reduced storage requirements. The standalone system achieves near-zero CO_2 emissions versus 178,609,602 kg/yr for the on-grid system, making it preferred for carbon-neutral requirements. The hydrogen subsystem fulfills fundamentally different roles in each configuration—routine dispatch on-grid versus emergency backup off-grid—suggesting standalone designs can reduce hydrogen investment. Battery utilization differences (215 versus 0.800 EFC/yr) highlight the critical importance of accurate dispatch simulation. Both configurations confirm the technical viability of large-scale PV-BESS-hydrogen microgrids in southern Thailand's tropical climate. Future work should address hydrogen subsystem cost sensitivity, dynamic tariff scenarios, and green hydrogen export potential.

Acknowledgment

The authors acknowledge the support of the Faculty of Engineering, Thaksin University (Phatthalung Campus), for providing the institutional facilities and research environment necessary to conduct this work.

References

[1] International Renewable Energy Agency. World Energy Transitions Outlook: 1.5°C Pathway; IRENA: Abu Dhabi, 2022.
[2] Energy Regulatory Commission of Thailand. Alternative Energy Development Plan (AEDP) 2018–2037; Ministry of Energy: Bangkok, Thailand, 2019.
[3] Denruechaidej, P.; Sukchan, S. Solar Energy Potential in Southern Thailand: Assessment and Mapping Using Satellite Data. Renewable Energy 2020, 150, 1–12.
[4] Lund, H. Renewable Energy Strategies for Sustainable Development. Energy 2007, 32, 912–919.
[5] Kousksou, T.; Bruel, P.; Jamil, A.; El Rhafiki, T.; Zeraouli, Y. Energy Storage: Applications and Challenges. Sol. Energy Mater. Sol. Cells 2014, 120, 59–80.
[6] Buttler, A.; Spliethoff, H. Current Status of Water Electrolysis for Energy Storage, Grid Balancing and Sector Coupling via Power-to-Gas and Power-to-Liquids: A Review. Renew. Sustainable Energy Rev. 2018, 82, 2440–2454.
[7] Stadler, M.; Cardoso, G.; Mashayekh, S.; Forget, T.; DeForest, N.; Agarwal, A.; Schönbein, A. Value Streams in Microgrids: A Literature Review. Appl. Energy 2016, 162, 980–989.
[8] HOMER Energy by UL. HOMER Pro® Microgrid Software Version 3.16: User Manual; HOMER Energy LLC: Boulder, CO, USA, 2022.
[9] Lilienthal, P.; Lambert, T.; Gilman, P. Computer Modeling of Renewable Power Systems. Encyclopedia of Energy; New York, NY, USA, 2004; 1, 633–647.
[10] Dursun, B.; Kilic, B. Comparative Evaluation of Different Power Management Strategies of a Stand-Alone PV/Wind/PEMFC Hybrid Power System. Int. J. Electr. Power Energy Syst. 2012, 34, 81–89.

[11] Ngan, M. S.; Tan, C. W. Assessment of Economic Viability for PV/Wind/Diesel Hybrid Energy Systems in Southern Peninsular Malaysia. Renew. Sustainable Energy Rev. 2012, 16, 634–647.
[12] Connolly, D.; Lund, H.; Mathiesen, B. V.; Leahy, M. The First Step towards a 100% Renewable Energy-System for Ireland. Appl. Energy 2011, 88, 502–507.
[13] Fathabadi, H. Techno-Economic Optimization of Hybrid Photovoltaic–Wind–Hydrogen Systems for Island Electrification. Appl. Energy 2020, 259, 114194.
[14] Shabani, B.; Andrews, J. An Experimental Investigation of a PEM Fuel Cell to Supply Both Heat and Power in a Solar-Hydrogen RAPS System. Int. J. Hydrogen Energy 2011, 36, 5442–5452.
[15] Khamharnphol, R.; Kamdar, I.; Waewsak, J.; Chaichan, W.; Khunpetch, S.; Chiwamongkhonkarn, S.; Kongruang, C.; Gagnon, Y. Microgrid Hybrid Solar/Wind/Diesel and Battery Energy Storage Power Generation System: Application to Koh Samui, Southern Thailand. Int. J. Renew. Energy Dev. 2023, 12, 216–226.
[16] NASA. Surface Meteorology and Solar Energy (SSE) Release 6.0 Methodology; NASA Langley Research Center: Hampton, VA, USA, 2020.
[17] Sonnen GmbH. Sonnen Batterie Eco 8.0/8kW-12kWh Technical Specifications; Sonnen GmbH: Wildpoldsried, Germany, 2021.
[18] Lambert, T.; Gilman, P.; Lilienthal, P. Micropower System Modeling with HOMER. In Integration of Alternative Sources of Energy; Farret, F. A.; Simões, M. G., Eds.; Wiley: Hoboken, NJ, USA, 2006; 379–418.
[19] Görgün, H. Dynamic Modelling of a Proton Exchange Membrane (PEM) Electrolyzer. Int. J. Hydrogen Energy 2006, 31, 29–38.
[20] International Energy Agency. Net Zero by 2050: A Roadmap for the Global Energy Sector; IEA: Paris, France, 2021.
[21] Sathyanarayana, P.; Ballal, R.; Sagar, P. L.; Kumar, G. Climate Characterization of Southern Thailand for Solar Energy Assessment. Sol. Energy 2019, 180, 289–302.
[22] Canadian Solar Inc. HiKu6 CS6W-550|555|560|565|570MS Module Datasheet; Canadian Solar Inc.: Guelph, ON, Canada, 2022.
[23] Electricity Generating Authority of Thailand. Grid Emission Factor 2022; EGAT Environmental Division: Bangkok, Thailand, 2022.
[24] Office of Natural Resources and Environmental Policy and Planning. Thailand's Nationally Determined Contribution (NDC); Ministry of Natural Resources and Environment: Bangkok, Thailand, 2022.
[25] International Renewable Energy Agency. Green Hydrogen Cost Reduction: Scaling Up Electrolysers to Meet the 1.5°C Climate Goal; IRENA: Abu Dhabi, 2020.

III. Environmental Engineering and Climate Solutions

Assessment of the Carbon Offset Requirements for International Routes of Thai-Registered Cargo Airlines

Wachira Pamornniyom[1*], Jakapong Pongthanaisawan[2]

[1] Energy Technology and Management, College of Interdisciplinary and Integrative Studies, Chulalongkorn University
[2] Energy Research Institute, Chulalongkorn University
*Correspondence: 6682022820@student.chula.ac.th

Abstract

Air Transportation is one of the most popular global logistics, yet the industry accounts for approximately 2.5% of global carbon dioxide (CO_2) emissions. Particularly, the air cargo sector is rapidly growing driven by the expansion of e-commerce and geopolitical factors. The data from the Civil Aviation Authority of Thailand (CAAT) indicates that air cargo volime in 2024 reached 1.51 million tons, marking a 22% year-on-year increase. The numbers have raised an awareness of CO2 emissions on Thai-registered cargo carriers due to their fleets often consist of older aircraft that are less fuel-efficient and emit higher CO2. The research is to focus on the implementation of the Carbon Offsetting and Reduction Scheme for International Aviation (CORSIA) for Thai cargo carriers. The study analyzes greenhouse gas (GHG) emissions from Thai cargo carriers using actual flight data from 2023-2025 to determine the offset demand using the CORSIA Fuel Use Monitoring method and determine the domestic supply of carbon credits that certified under the Premium T-VER standard. The research findings indicate that while Thai-registered cargo carriers remain within CORSIA baseline, the trends have shown a steady rising in GHG emissions due to the growth of the E-Commerce Market increasing the needs for offset. The research also identified a significant supply gap in the domestic carbon market, Premium T-VER credits certified by the Thailand Greenhouse Gas Management Organization (TGO). The research concluded with data-driven policy recommendations for the policy makers and industry stakeholders to align domestic credit supply with international aviation offset demands.

Keywords: Aviation Industries; Carbon Offsetting; Carbon Credits; Thai-Registered Cargo Airlines; CORSIA

1. Introduction

Among various modes of transportation, air travel is one of the most popular worldwide because it is widely recognized for enabling long-distance travel in the shortest time when compared to other forms of transportation. Despite its popularity, the Intergovernmental Panel on Climate Change (IPCC) has estimated that the aviation industry is responsible for about 2.5%—or approximately 1 billion tons—of global carbon dioxide (CO_2) emissions. The International Air Transport Association (IATA) predicts that cargo volume in 2025 will reach 72.5 million tons, which would represent a 5.8% increase from 2024[1]. This growth is driven by the expansion of e-commerce and geopolitical factors affecting maritime transport.

Based on these issues, airlines and various aviation regulatory organizations from many countries have become increasingly aware of the significant CO_2 emissions produced by the aviation industry. Therefore, the International Civil Aviation Organization (ICAO) launched the Carbon Offsetting and Reduction Scheme for International Aviation (CORSIA) in which ICAO member states set a target to achieve net-zero CO_2 emissions by the year 2050[2].

Thailand is one of the members in the ICAO[3] and is therefore required to comply with CORSIA implementation, which currently requires to begin submitting data on the amount of CO_2 emissions from international flights. However, most cargo carriers may face difficulty in reducing CO_2 emission due to the age of the aircraft in-service. Based on IATA research, it was found that the average age of dedicated cargo is significantly higher than passenger aircraft, at 25 years. Older aircraft are less fuel efficient and emit more CO_2 per revenue ton kilometer (RTK) than newer aircraft[4]. Therefore, this study focuses on the challenges faced by Thai-registered cargo airlines by preliminary analyzing their air traffic statistics and actual fuel consumption data. These informations will be calculated and assessed using a CO_2 emissions assessment tool based on Fuel Use Monitoring Method approved by ICAO. This analysis leads to the evaluation of their carbon offsetting requirements in accordance with the given timelines from the CORSIA program. As Thai-registered cargo airlines face increasing pressure to meet CORSIA requirements, once annual CO_2 emissions surpass individual baseline, cargo carriers must mitigate or purchase eligible carbon credits to offset their emissions when the mandatory phase begins 2027.

Consequently, the reliance on domestic offsetting mechanisms via local carbon market named “Thailand Voluntary Emission Reduction – T-VER” may require urgent evaluation whether the current carbon market can effectively support the rising demand for Thai aviation sector. The T-VER is a voluntary carbon market managed Thailand Greenhouse Gas Management Organization (TGO), a public organization under the Ministry of Natural Resources and Environment, which serves as the primary national mechanism for greenhouse gas reduction[5]. In addition, TGO has also introduced the Premium T-VER scheme for a high-quality carbon credit complying international standards such as CORSIA. However, the availability of Premium T-VER credits remain uncertain and require further assessment. Therefore, this study identifies critical market gaps and finding a data-driven framework for general policies and economic sustainability of Thailand’s air cargo carriers.

2. Literature Review

2.1 Overview of Air Cargo in ASEAN

According to the IATA report, as show in Error! Reference source not found., the Air Cargo S ector within the ASEAN for the 2023 year has shown the leading country of air cargo transport is Singapore, which handling a total of 1.8 million metric tons of air cargo[6]. The second and third places held for Indonesia[7] and Vietnam[8], each handled approximately 1.3 million tonnes for air cargo. These two countries' air traffic are mainly domestic, with only 19% and 29% of international air traffic respectively. The fourth place is Thailand[9] which has air cargo transported slightly less than Indonesia and Vietnam at about 1.2 million tonnes, but with a higher international air traffic accounted for 51% . In addition, the data from the CAAT indicates that air cargo volume in 2024 reached 1.51 million tons, an increase of over 22% in 2023 involving all high-value or time-sensitive goods such as Jewelry, premium fruits and fresh seafood, Pharmaceuticals, Electronics, IT equipment, garments, automotive components, etc[10]. Lastly, Malaysia[11] came in fifth place handling 941,400 tonnes of air cargo and the Philippines[12] handled an estimated 830,000 tonnes of air cargo in 2023. Therefore, Thailand considers a significant hub for international air cargo in ASEAN region. This aslo highlights that the increasing volume of international air cargo operations is expected to result in higher fuel consumption for Thai-registered cargo airlines’ operations.

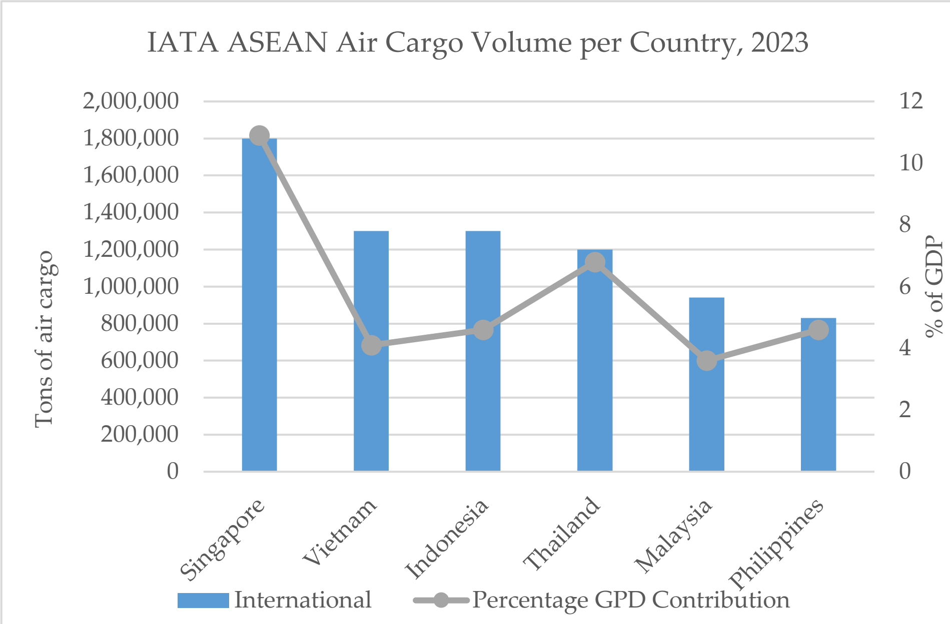

Figure 1. ASEAN Air Cargo Volume by Country, 2023

2.2 Strategic Approaches for CO_2 Reuction in Aviation Industry

In cooperation with ICAO, IATA outlines approaches to help airlines achieve net-zero emission for airlines operation by 2050. Those strategic approaches have been set into four plans and have been evaluated as the potential for aviation emission reduction, as shown in Figure 2.

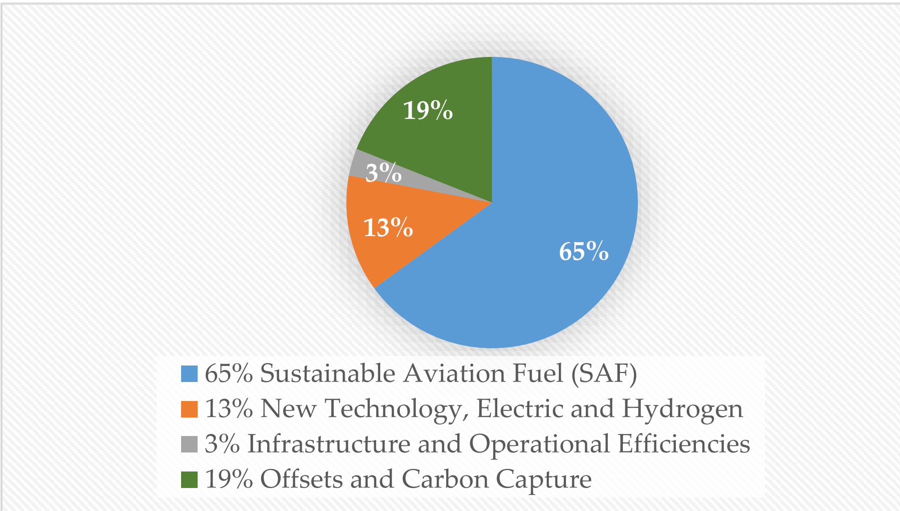

Figure 2 The proportions that the International Air Transport Association's (IATA) assessment suggests will enable airlines to achieve net-zero carbon dioxide emissions by 2025[13].

Based on the illustration, it is evident that there is no single measure that can fully decarbonize for the aviation sector. The first and the most effective approach is the Sustainable Aviation Fuel (SAF), which is considered the primary solution containing potential to deliver up to 65% of the emissions reductions needed by 2050. The second significant approach is carbon offsetting and carbon capture which holds 19% of the emission reductions needed. Moreover, the upcoming implementation of the second phase of the Carbon Offsetting and Reduction Scheme for International

Aviation (CORSIA), which will begin in 2027 and mandate offsetting requirements, is expected to impose a significant cost burden on Thai airlines — particularly in terms of sourcing high-quality, certified carbon credits at a premium price**.**

2..2.1. Sustainable Aviation Fuel (SAF)

Sustainable Aviation Fuel (SAF) is a low-carbon fuel derived from waste materials such as animal fats, used cooking oil, or biological resources, such as animal fats, used cooking oil, etc. It is a highly effective method in reducing greenhouse gas emissions in the aviation industry[14]. The SAF has been expected by the aviation industry to be producing as a "Drop-in" replacement to conventional jet fuel.

According to the Sustainable Aviation Fuel Fact Sheet published by IATA, there are currently 9 (nine) approved technology pathways capable of producing drop-in SAFs in Table 1[15].

Table 1. 9 Approved Technology Pathways for Sustainable Aviation Fuel

Pathway	**Approved Name**	**Blending Limitation**
Fischer-Tropsch (FT) Synthetic Paraffinic Kerosene (SPK)	FT-SPK	50%
Hydroprocessed Esters and Fatty Acids	HEFA-SPK	50%
Hydroprocessed Fermented Sugars to Synthetic Isoparaffins	HFS-SIP	10%
FT-SPK with Aromatics	FT-SPK	50%
Alcohol-to-Jet Synthetic Paraffinic Kerosene	ATJ-SPK	50%
Catalytic Hydrothermolysis Synthesized Kerosene	CH-SK	50%
Hydrocarbon-Hydroprocessed Esters and Fatty Acids	HC-HEFA-SPK	10%
Fats, Oils, and Greases (FOG) Co-Processing	FOG Co-Processing	5%
FT Co-Processing	FT Co-Processing	5%

Despite its environmental benefits, SAF still faces several limitations that challenge its widespread adoption in Thailand. One major limitation is the restricted availability of SAF feedstock and production capacity, which is influenced by stringent international certification and sustainability requirements imposed by organizations such as IATA and ASTM. These regulatory standards increase the complexity of SAF production and procurement processes, resulting in significantly higher production costs compared to conventional jet fuel. Consequently, SAF has not yet become a commercially viable large-scale replacement for traditional aviation fuel in many countries, including Thailand.

2..2.2. New Technologies, Hydrogen, and Electric Aeroplane

Hydrogen-powered aeroplanes have attracted significant attention due to its exceptionally high energy density, approximately three times than the conventional jet fuel (33kWh/kg). Also, once compared to SAFs, hydrogen is likely to be more popular in other industries which could fasten the development process of hydrogen production. However, despite its potential, hydrogen also comes with several major limitations, such as the readiness of airport infrastructures, the size and weight of hydrogen fuel cells etc. The HFC systems are relatively large and bulky, particularly when designed to power large commercial aircraft carrying over 200 passengers or flying distances greater than 1,600 kilometers. The current technology still struggles to meet the energy demands of long-haul flights without significantly compromising aircraft weight and design efficiency[16].

Electric-powered aircraft are often the subject of much discussion as a promising alternative energy solution in aviation. However, electric aircraft still face significant technical challenges that must be addressed before they can be considered commercially viable. Key limitations include Battery energy density, Aircraft and engine design, Thermal management, and Charging infrastructure and turnaround time.

The comparison as shown in Table 2 conventional jet fuel has an energy density of approximately 12,700 Wh/kg, while lithium-ion batteries offer only about 250 Wh/kg—a stark difference of nearly 48 times. Due to this limitation, electric-powered aircraft must carry much heavier batteries to achieve flight ranges comparable to those of traditional fuel-powered aircraft. This added weight not only reduces the overall payload capacity (limiting the ability to carry cargo or passengers) but also shortens the maximum flight distance, making such aircraft less suitable for commercial operations, especially for long-haul or cargo-intensive flights [17].

Table 2. A comparison of energy density between batteries and conventional fuel

Battery Type	Energy Density
Lead acid	123 Wh/kg
Lithium ion	250 Wh/kg
Zinc-oxygen	1,084 Wh/kg
Sodium-oxygen	1,605 Wh/kg
Magnesium-oxygen	6,800 Wh/kg
Aluminum-oxygen	8,100 Wh/kg
Lithium-sulfur	2,600 Wh/kg
Lithium-air	11,140 Wh/kg
Gasoline	12,700 Wh/kg

2.2.3. Infrastructure and operational efficiencies

One of the contributing factors to reducing greenhouse gas emissions in the aviation industry comes from the development of supporting infrastructure and enhancing operational efficiency. Unlike other long-term solutions—such as designing new aircraft models or developing green propulsion technologies, these improvements can typically be implemented more quickly and deliver results in the short term[18] .

Measurements and practices from aeroplane operators that could support operations efficiency:

- Reducing unnecessary onboard weight: This involves removing non-essential items that do not affect flight safety, such as excess in-flight amenities, or carrying less surplus food and water than needed for the number of passengers onboard.
- Using lighter materials: Replacing existing onboard items with lightweight alternatives, such as switching from ceramic or metal cups to paper or plastic cups for in-flight services. Replacing aluminium Unit load device (ULD) to the lightweight ULDs for carrying baggage, mail, cargo instead.
- Improving air traffic management systems (ATM): Enhancing ATM systems at airports to reduce ground traffic congestion, minimizing taxi times, and optimizing flight paths to lower fuel consumption.
- Enforcing single-engine taxiing during ground movement to reduce fuel burns.

- Minimizing the use of the Auxiliary Power Unit (APU), which generates electricity while the aircraft is on the ground, and instead using Ground Power Units (GPU), which are more energy-efficient and often powered by cleaner sources.

Although many of these initiatives can be implemented relatively quickly and with immediate impact, their contribution to overall emission reductions is limited in scale. According to estimates from the International Air Transport Association (IATA), improvements in infrastructure and operational efficiency measures will contribute only about 3% toward the aviation industry's Net Zero emissions target.

2.2.4. Carbon Offsetting

As illustrated in Figure 2 that mentioned contribution of Carbon Offsetting, which accounts for approximately 19% of the aviation sector's path to Net Zero emissions, carbon offsetting has been established as one of the key mechanisms for reducing carbon dioxide (CO_2) emissions in aviation. As of October 2025, ICAO has announced the Emission Unit Programs that has been approved by the ICAO Council (Table 3) to be supplied to CORSIA Eligible Emissions Units during the 2024 – 2026 compliance period (First Phase)[19].

Table 3. List of CORSIA Eligible Emissions Units for the 2024-2026 Compliance Period.

Emissions Unit Program	**Program-Designated Registry**	**Origin Country**
American Carbon Registry (ACR)	ACR Registry https://acrcarbon.org/acr-registry/	United States of America
Architecture for REDD+ Transactions (ART)	ART Registry https://www.artredd.org/art-registry/	United States of America
Climate Action Reserve (CAR)	Climate Action Reserve Voluntary Offset Project Registry https://thereserve2.apx.com/mymodule/mypage.asp	United States of America
Global Carbon Council (GCC)	Global Carbon Council Registry https://mer.markit.com/br-reg/public/public-view/#/account	Qatar
Gold Standard (GS)	GSF Impact Registry https://registry.goldstandard.org/projects?q=&page=1	Switzerland
Isometric	Isometric Registry https://registry.isometric.com/	United Kingdom
Verified Carbon Standard (VCS)	Verra Registry https://verra.org/registry/overview/	United States of America
Premium Thailand Voluntary Emission Reduction Program (Premium T-VER)	Premium T-VER Registry https://ghgreduction.tgo.or.th/en/premium-t-ver.html	Thailand

As detailed in Table 3, CORSIA eligibility is currently restricted to eight specific emission unit programs. The inclusion of the Premium T-VER standard within this framework represents a critical milestone, validating Thailand's domestic market as a viable instrument for meeting international aviation offsetting requirements for Thai Aviation Industry. Despite this progress, the limited number of accredited programs for the first phase highlights a potential supply-side bottleneck.

2.3 Carbon Offsetting and Reduction Scheme for International Aviation (CORSIA)

The Carbon Offsetting and Reduction Scheme for International Aviation (CORSIA) has been established by the International Civil Aviation Organization (ICAO) from the 39th Assembly in October 2016, which was adopted from the Paris Agreement at UN Climate Charge Conference (COP21) in 2015. From 2020, the aviation sector will have to neutralize its international CO_2 emissions above this level. However, a critical adaptation to the scheme occurred in response to the COVID-19 pandemic; in June 2020, the ICAO Council agreed that the COVID-19 situation has influenced the emissions baseline, originally tied to 2019-2020 levels, was ultimately set at 85% of 2019 emissions for the period from 2024 onward, a move that significantly increased its environmental ambition [20].

CORSIA requires all aircraft operators that produce an annual CO_2 emission on their international flights of more than 10,000 tons with aircraft with a Maximum Take Off Mass (MTOM) greater than 5,700 kg whether or not their country is in the accession stages CORSIA or not, will be required to monitor, report, verify (MRV) their CO_2 emissions to their national authority which was started since 1st January 2019 (**Figure 3**). In addition, if any operator's emissions decrease below 10,000 tons, the operator will fall outside the requirement of CORSIA and will no longer report its emissions[21]. CORISA, governed by timelines and compliance periods starting with two voluntary phases (a Pilot Phase from 2021-2023 and a First Phase from 2024-2026) to build capacity and political momentum, before transitioning to a mandatory phase for most states from 2027 to 2035 [22].

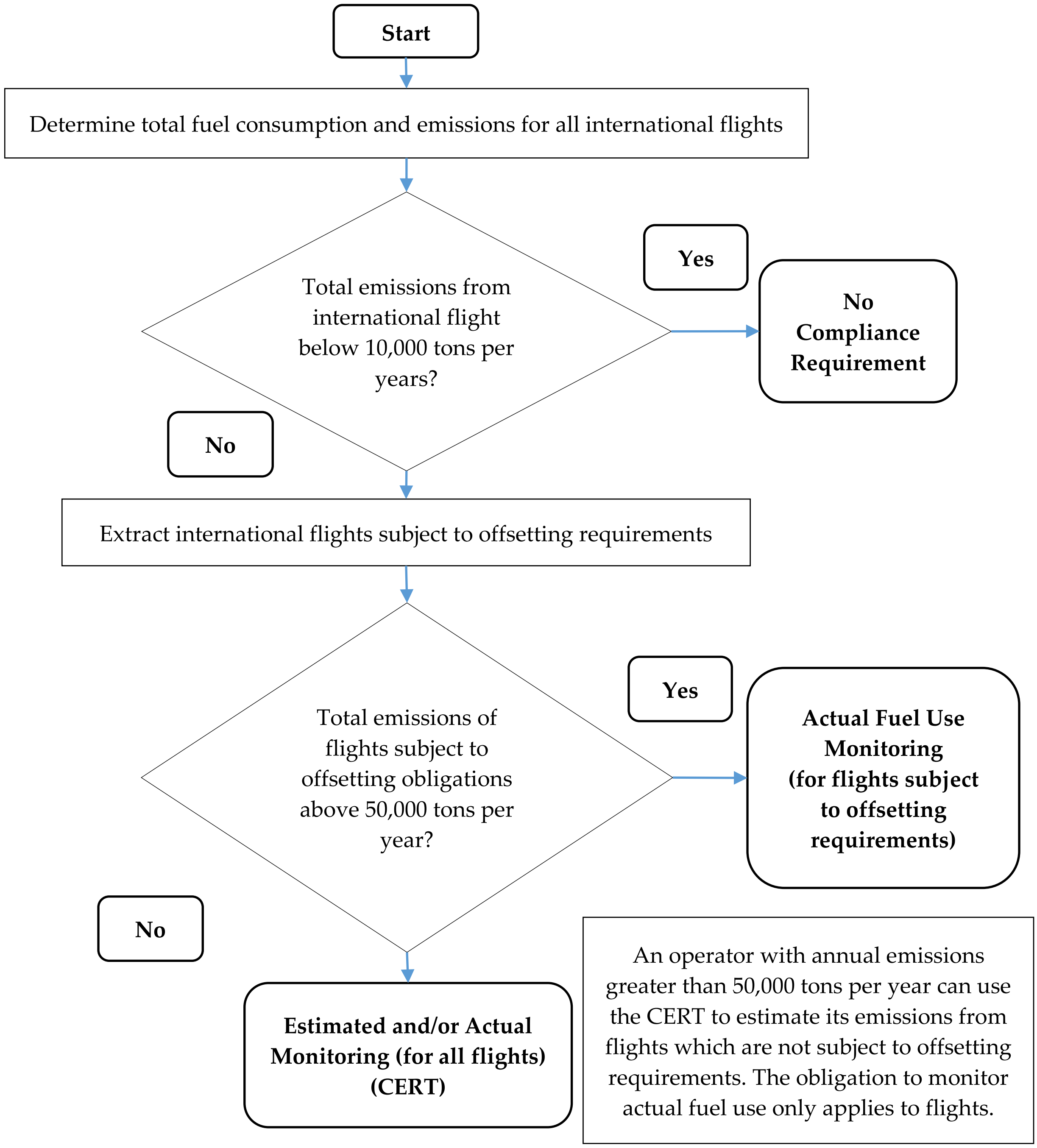

Figure 3. Decision Flowchart for Monitoring, Reporting and Verification under CORSIA

However, there are several exemptions from CORSIA which are not subject to any of its MRV or offsetting requirements such as:

- Operations with aeroplanes with a MTOM below or equal to 5,700 Kg;
- Any humanitarian, medical, and firefighting flights;
- Operators whose total annual CO_2 emissions from international aviation are below or equal to 10,000 tons.

The ICAO CORSIA CO_2 Estimation and Reporting Tool or CERT was developed by the ICAO to be a tool (an Excel-based application) supporting aeroplane operators to comply with the simplified monitoring, reporting, and verification (MRV) requirement under CORSIA. It allows aeroplane operators to import or manually input the required information to generate emission estimations. The ICAO also developed the ICAO CO_2 Estimation Models (CEMs) which is the CO_2 estimation model using a collection of statistical models to simplify for aeroplane operators to determine the CO_2 emission. The CEM calculation is based on a liner or non-linear regression model that relates the inputs (GCD or Block Time) to estimate fuel consumption (kg) for a specific aircraft type. The models are based on actual historical fuel burn data and calculate estimated CO_2 emissions by requiring either the Block Time or Great Circle Distance (GCD) between the origin and destination airports[21] .

2.4 Thai Domestic Carbon Credits and Market

Thailand's market has established a voluntary carbon credit trading market under the Thailand Voluntary Emission Reduction Project (T-VER), managed by the Thailand Greenhouse Gas Management Organization (TGO), since 2012. In order for credits to be issued and traded, each project must undergo validation and verification by an accredited Validation and Verification Body (VVB) registered with TGO. Nevertheless, the carbon credits under the T-VER Standard may not be able to offset under the ICAO standard. TGO has been actively working to make T-VER carbon credit eligible for use under CORSIA standards, thus, TGO has developed "Premium T-VER" standard and submitted to ICAO for their approval[23]. If the Premium T-VER credits are approved and eligible for ICAO, this could potentially be the domestic carbon credit for offsetting for Thai airlines, especially, freighters and will create a direct link between Thailand's voluntary carbon market and the global carbon market.

The Premium T-VER has been designed to align with international standards and to be accepted by a CORSIA eligible Emission Unit Program. In 2025, ICAO has now approved the Premium T-VER as a first batch of eligible units for a Compliance Period (First Phase) during 2024 - 2026 and the carbon unit must be from the emission reduction project during 2021 -2026[24] .

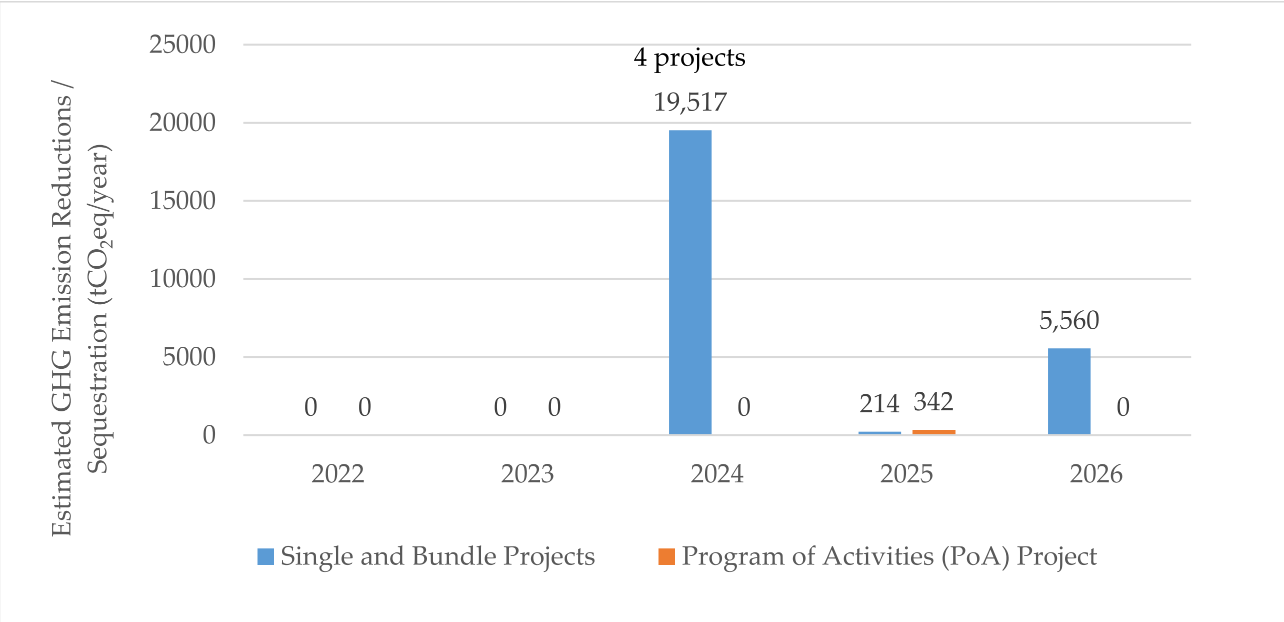

Figure 4. Statistics on the Registration of Premium T-VER projects (Single, Bunding, and T-VER PoA) [25]

To assess the viability of the local compliance, the emissions data generated in this study was aggregated against the official TGO Premium T-VER registry. Figure 4 has shown the number of projects that registered under Premium T-VER from 2022 to 2026. Based on the research findings of the current Premium T-VER market, there are 9 project participants who are registered in Single and Bundling Projects and only 1 project participant registered in a Program of Activities (PoA) project. As of the end of March 2026, the estimated GHG Emission reductions/sequestration are expected to be around 25,633 tCO_2eq/year, but only 1 project from the Program of Activities (PoA) that has been certified and amount of Carbon Credits Certified is only 60 tCO_2eq/year. If all the current registered projects are validated and certified, the maximum domestic carbon credit supply is estimated at approximately 25,633 tCO_2eq/year.

3. Materials and Methods

3.1 Scope of Study

The study focuses on analyzing the demand for carbon offet requirements withim Thailand's international air cargo transporatation, particularly for Thai-registered cargo airlines, in the context of the international climate complaince frameworks like the Carbon Offsetting and Reduction Scheme for International Aviation (CORSIA) by ICAO. The scope of this research includes:

- Data collection of the actual fuel consumption and operational data from two Thai-registered cargo airlines which are K-Mile Air (8K) and Pattaya Airways (VV).
- The evaluation of carbon emissions produced by the airlines between 2023-2025 using the standard of ICAO CORSIA Fuel Use Monitoring Method. This analysis extends to the projecting future demand of carbon offsetting requirements in alignment with the timeline of CORSIA implementation.
- The study evaluates the availability of the domestic carbon market, Thailand Voluntary Emissions Reduction (T-VER), developed by Thailand Greenhouse Gas Management Organization (TGO), as a primary supply of the credit. Particularly, the Premium T-VER program which is designed to align with international standards to determine its capacity whether the program is capable to meet the projected offsetting demand from Thai-registered cargo airlines.

3.2 Fuel Use Monitoring Methods

Regarding to the Figure 3, once operators has total emissions exceed 50,000 tons per year from flights subject to offsetting obligations, the operator directs to use Fuel Use Monitoring Method, the CO_2 emission can be followed the following equation:

$$\mathrm{CO_2} = \sum Mf * FCF\ f \tag{1}$$

where CO_2 = CO_2 emission (in tons)
Mf = Mass of fuel f used (in tons)
FCF f = Fuel conversion factor of given fuel f, equal to 3.16 (in kg CO_2/kg fuel) for Jet-A fuel

Emission factor: CO_2 emissions are calculated using the Emission Factor of 3.16 kilograms of CO_2 per Kilogram of Jet A/A1[21]. (Also, the same Emission Factor should be applied to fuels equivalent to Jet A/A1 such as TS-1, etc.) and the Emission Factor used for Jet-B and AvGas is 3.10 kilograms of CO_2 per kilogram of fuel.
CORSIA provides five eligible Fuel Use Monitoring Methods. An operator can choose from one of these methods based on the available information and details of them in the Emission Monitoring Plan (EMP). Based on the ICAO Handbooks[21], the five Fuel Use Monitoring Methods are:
Method A is the estimation of fuel used based on measurements after the completion of fuel uplifts (for the flight under consideration and the subsequent flight) and the fuel uplift for the subsequent flight.

Method B, which is based on measurements at block-on times (preceding flight and flight under consideration) and the fuel uplift for the flight consideration which also break down to the following sectors.
Block-off/Block-on, which is based on the fuel consumed between block-off and block-on.
Fuel uplift, which is based on the fuel uplift before each flight, measured in volume and multiplied by a density value.
Fuel allocation with block hours, which applies the average fuel burn ratio by aircraft type and during the reporting year in question to the block hours of each flight as shown in equation (2)

$$Fuel\ used = BH\ x\ AFBR \quad (2)$$

Where BH is the block hour for the international flight under consideration for the operator type (in hours);
AFBR is the average fuel burn ratios for the operator and aeroplane type (in tonnes per hour);
To compute the average fuel burn ratios (AFBR),

$$AFBR = \frac{\sum U}{\sum BH} \quad (3)$$

Where U is the fuel uplifted for the international flight for the operator and aeroplane type (in tons);
BH is the block hour for the international flight and aeroplane type (in hours);

4. Results and Discussion

4.1 Emissions Assessment of Thai-registered Cargo Carriers

The assessment of greenhouse gas emissions for the Thai-registered cargo airlines was executed using “Total Fuel Consumed from International Route” data provided by the airlines and the flight’s history data retrieved from Flight Radar 24 via the website from 2023-2025. In accordance with ICAO-standard Fuel Use Monitoring Methods, the “Fuel Allocation with Block Hour” methodology was selected to analyze the information.

The calculation for the CO_2 emissions using the mentioned methodology requires the actual annual fuel consumption data which can represent the total fuel uplift for each type of aircraft. The second information is the “Block Hour” for the specific international flight which is measured from the moment the aircraft first moves from its parking for the purpose of taking off (Block-Off) until the moment it comes to rest at the designated parking at the destination (Block-On). Therefore, the Average Fuel Burn Ratio (AFBR) can be calculated from the cumulative sum of total fuel uplift divided by the sum of total block hours in each specific year.

4.1.1 Operational Profiles and Fleet Characteristics of K-Mile Air (IATA: 8K)

The calculation annual emissions for K-Mile Air from 2023 to 2025 ae summarized in Table 4. The data revealed a significant upward in carbon output.

Table 4. Annual CO_2 Emissions Profile of K-Mile Air (8K) Fleet (2023-2025)

Type of Aircraft	Number of Aircraft in the fleet	Avg. Age of Aircraft	Year 2023		Year 2024		Year 2025	
			Total CO_2 Emission in each year (Tons)	Ton-kilometers performed (thousand)	Total CO_2 Emission in each year (Tons)	Ton-kilometers performed (thousand)	Total CO_2 Emission in each year (Tons)	Ton-kilometers performed (thousand)
B737-400SF	3	28	27,640	21,500	28,780	24,600	23,970	20,400
B737-800BCF	2	22	34,240	39,200	29,100	34,700	27,270	32,300
B 767-300BCF	2	23	-	-	14,540	19,200	75,340	104,150
Total	7	24.3	61,880	60,700	72,420	78,500	126,580	156,850

The calculated annual CO_2 emissions and transport activity for K-Mile Air (8K) was analyzed throughout 2023-2025 are summarized in Table 4 using the primary operational data provided by the airlines. As of 2025, the airlines' fleet consists of 7 (seven) dedicated freighter aircraft including 3 (three) Boeing B737-400SF (B734), 2 (two) B737-800BCF (B738) and 2 (two) B767-300BCF (B763). However, the fleet has a significant transition that directly influenced the annual carbon footprint. 2 (two) wide-body B767-300BCF were integrated into operations at the beginning of Q3 2024, while 1 (one) B737-400SF was decommissioned at the end of Q3 of 2025. After the calculations, consolidated in Figure 5, reveal an increase in annual CO_2 emissions together with traffic volume over the three-year period.

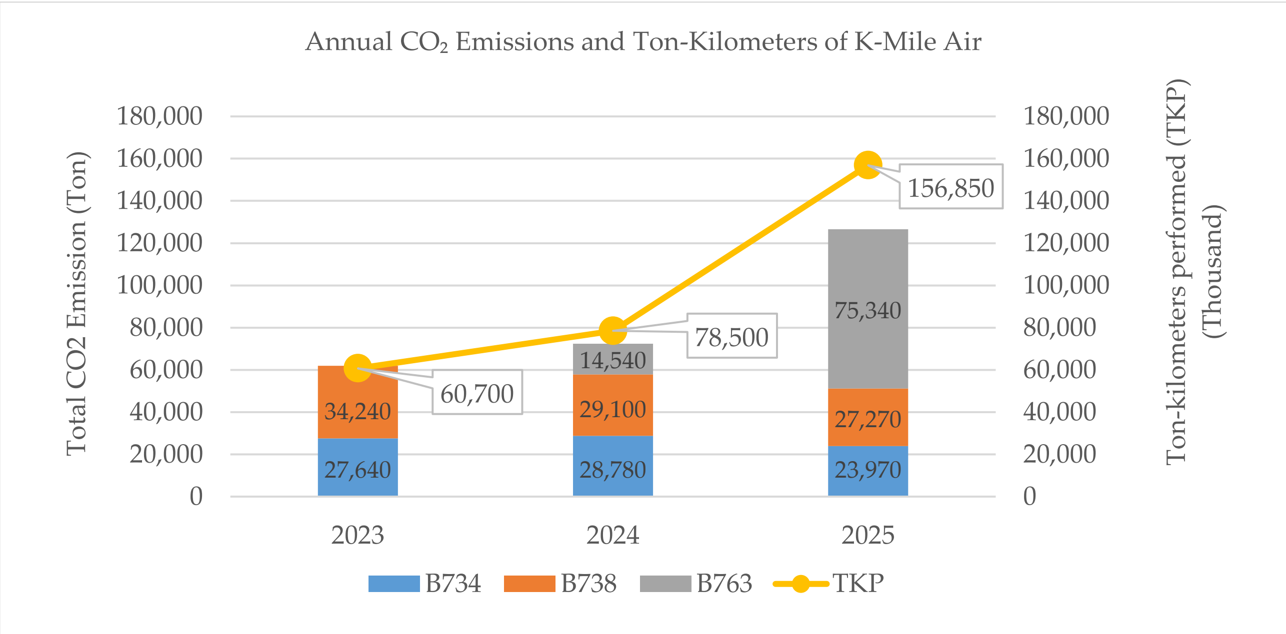

Figure 5. Growth Trend of Annual CO_2 Emissions for K-Mile Air (2023-2025)

The findings also revealed that K-Mile Air's emissions have moderately increased approximately 17 percent between 2023 and 2024, coinciding with the induction of the B767-300BCF fleet in the third quarter of 2024. This growth pattern aligned with a 29 percent increase in total Ton-Kilometer Performed (TKP) during the same period. Consequently, the sharp increase in 2025, representing a 74.7 percent increase of CO_2 emissions along with the double volume of TKP from

2024, is primarily driven by the full-year operational cycle of the wide-body B763 aircraft totaling 126,580 tCO_2 which offsets a slight reduction of CO_2 emissions from B734 and B738 fleets. Furthermore, the study determined that the K-Mile fleet has an average age of 24.3 years. This number is similar with the global industry benchmark for dedicated cargo aircraft, approximately 25 years, which indicated that the older aircraft are less fuel-efficient and have higher emitters. These results confirm that K-Mile Air has consistently exceeded the 50,000-ton CORSIA threshold, requiring a rigorous monitoring requirement as the industry moves toward mandatory compliance phases within 2027.

4.1.2 Operational Profiles and Fleet Characteristics of Pattaya Airways (IATA: VV)

Pattaya Airways representing the regional segment of the Thai-dedicated cargo market. The calculation of annual emissions for turboprop fleet and operational activities from 2024 to 2025 are detailed in Table 5. The data revealed a significant upward in carbon output.

Table 5. Annual CO_2 Emissions Profile of Pattaya Airways (VV) Fleet (2024-2025)

Type of Aircraft	Number of Aircraft in the fleet	Avg. Age of Aircraft	Year 2024		Year 2025	
			Total CO_2 Emission in each year (Tons)	Ton-kilometers performed (thousand)	Total CO_2 Emission in each year (Tons)	Ton-kilometers performed (thousand)
ATR 72-500F	2	22	460	441	5,050	26,700
Total	2	22	460	441	5,050	26,700

Pattaya Airways operates 2 (two) converted ATR 72-500 freighters, starting operation in the second quarter of 2024. Since operation in 2024, the airline's fleet has been operating 2 (two) dedicated turboprop freighter aircraft. The table above has shown a significant difference between 2024 and 2025 due to airlines was initially operated in the second quarter of 2024. After the calculations, consolidated in Figure 6, reveal an increase in annual CO_2 emissions over the study period.

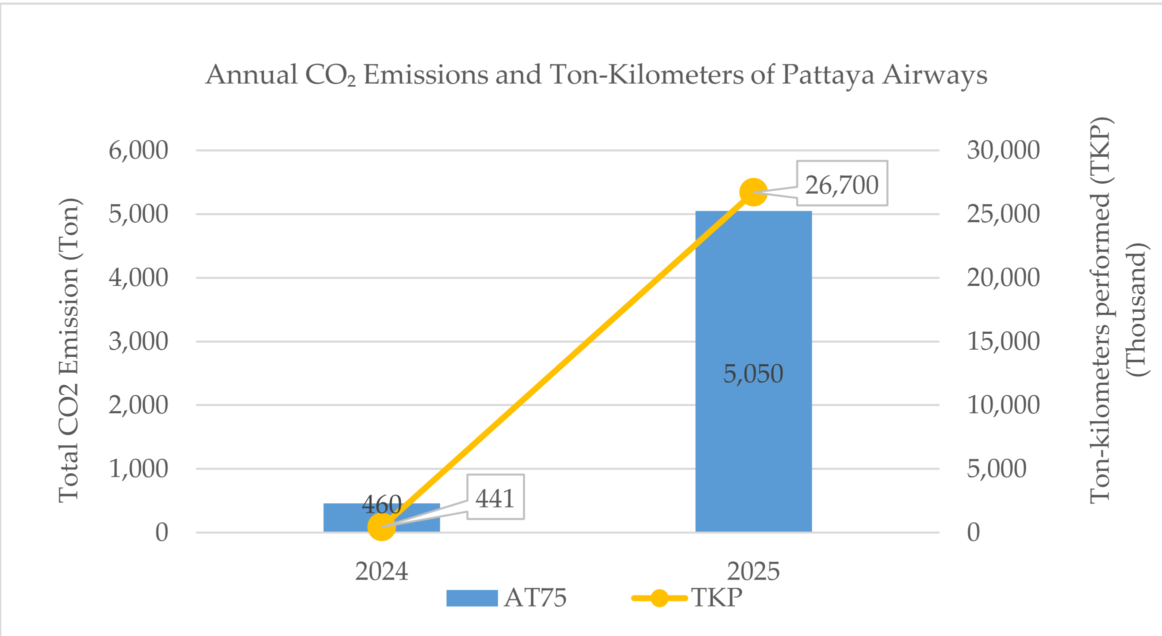

Figure 6. Growth Trend of Annual CO_2 Emissions for Pattaya Airywas (2024-2025)

While the airlines only emitted 460 tCO_2 and performed 441 thousand Ton-Kilometers (TKP) in 2024, but 2025 emitted 5,050 tCO_2 which is nearly 11 times larger from a full-year operation of 2 (two) ATR72-500 F in 2025. While the fleet's configurations emitted lower fuel consumption compared to jet engines, the study found that Pattaya's fleet has an average age of 22 years which may degraded fuel consumption. Pattaya Airway's current emissions remain below the reporting threshold of CORSIA beneficially from the turboprop aircraft.

4.2 Projected Cargo Volume and Future Emssions Trends

4.2.1 National Cargo Volume History and Future Forecast

When looking at the Figure 7 - Thai air freight history data since 2018 to 2024 reveals a distinct V-shaped recovery following the severe disruption during the COVID-19 pandemic. However, after 2020, the air freight volume steadily increased up to 1.51 million tons in 2024, outnumbering the volume in 2019 and which is 58.8 percent increase from 2020.

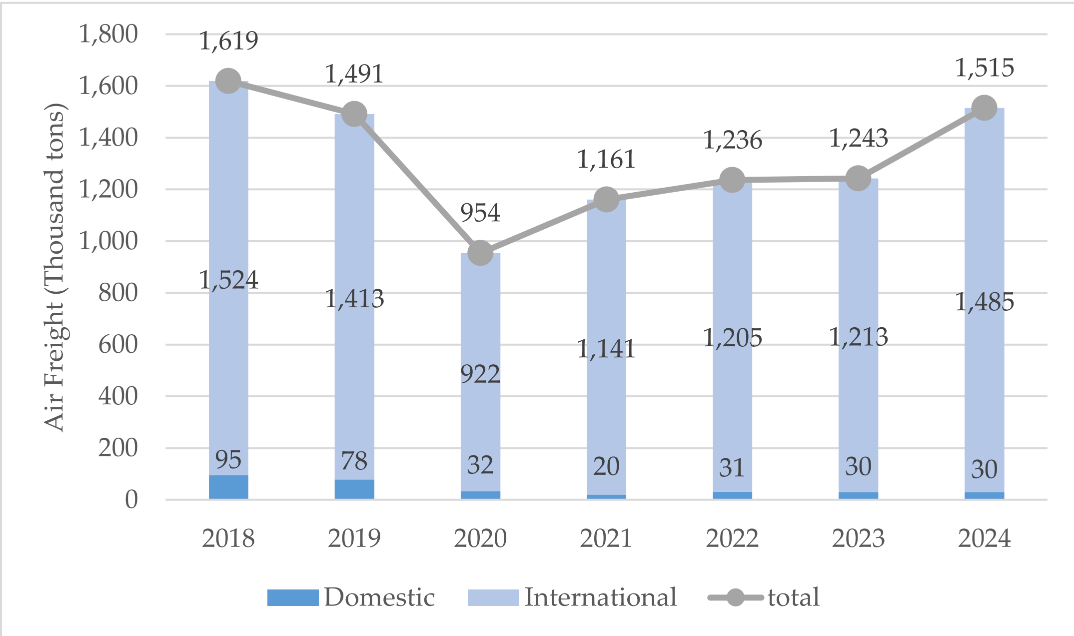

Figure 7. Thailand Air Freight Volume Statistics (2018-2024)[26]

When correlating with the calculation data from K-Mile Air and Pattaya Airways, it was found that an increase in CO_2 emission during the study years for both airlines is also attributed to the CAAT National Overall Cargo Volume Forecast in Table 6. The baseline cargo volumes at approximately 1.51 million tons in 2024 and are expected to escalate the volume to 1.86 million tons in 2027 and 2.55 million tons in 2035. This escalation is reflected to a 68% expansion over the eleven-year forecast. Even the Low Growth Scenario has also shown an increase of cargo volume each year which can be represented a sustained growth may be driven from the ongoing surge in e-commerce and changing global maritime logistics.

Table 6. CAAT National Overall Cargo Volume Forecast[27]

Year	Low Growth Scenario		Base Case Scenario		High Growth Scenario	
	Cargo Volume (Kilograms)	**Growth Rate**	**Cargo Volume (Kilograms)**	**Growth Rate**	**Cargo Volume (Kilograms)**	**Growth Rate**
2024	1,515,245,412	21.90%	1,515,245,412	21.90%	1,515,245,412	21.90%
2025	1,601,965,235	5.70%	1,631,993,881	7.70%	1,655,435,062	9.30%
2026	1,688,115,013	5.40%	1,748,171,933	7.10%	1,795,053,848	8.40%
2027	1,774,264,067	5.10%	1,864,348,890	6.60%	1,934,671,091	7.80%
2028	1,860,412,400	4.90%	1,980,524,755	6.20%	2,074,286,798	7.20%
2029	1,946,560,014	4.60%	2,096,699,533	5.90%	2,213,900,975	6.70%
2030	2,018,723,026	3.70%	2,176,206,142	3.80%	2,321,127,131	4.80%
2031	2,090,885,550	3.60%	2,255,712,008	3.70%	2,428,352,357	4.60%
2032	2,163,047,589	3.50%	2,335,217,134	3.50%	2,535,576,656	4.40%
2033	2,235,209,144	3.30%	2,414,721,521	3.40%	2,642,800,031	4.20%
2034	2,307,370,216	3.20%	2,494,225,174	3.30%	2,750,022,487	4.10%
2035	2,355,110,448	2.10%	2,550,284,392	2.20%	2,837,793,521	3.20%

To isolate the direct impact of this cargo demand forecast modeled from the growth rate percentage of baseline scenario, assuming that both K-Mile Air (8K) and Pattaya Airways (VV) maintain their current operational fleet sizes and present flight frequencies as per year 2025. Under this scenario, the transport activities measured in Ton-Kilometers Performed (TKP) climb in direct proportion to the national demand rate as illustrated in Figure 8**.** Pattaya Airways's TKP is projected to grow to 30,483 thousand TKP in 2027 and reaching 41,729 thousand TKP in 2035 which is represented 36.89% increase over the eight-year CORSIA mandatory framwork. Concurrently, a larger operator, K-Mile Air is projected to generate its transport output in 2027 at 179,073 thousand TKP and grows up to 244,928 thousand TKP by 2035, a 36.77% expansion of projected cargo demand.

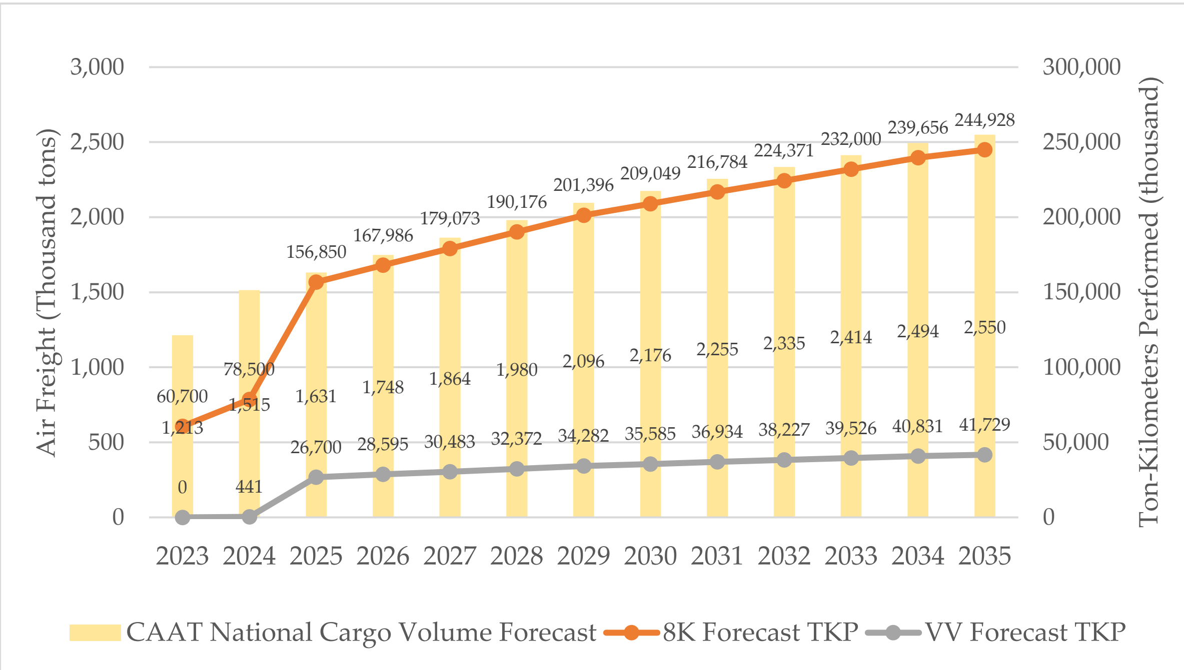

Figure 8. Comparison of CAAT National Cargo Volume Forecast and Projected of Ton-Kilometer Performed (TKP) for K-Mile Air and Pattaya Airways through 2023-203

4.2.2 Future Emissions Trends

Since the proportion of the Cargo Volume can result to an increase of CO_2 emission, the future trend of CO_2 emission can also be predictively risen from the CAAT National Cargo Volume Forecast. The projected inflation in transport activity (TKP) for both carriers has shown a potential increase in total greenhouse gas emissions profiles. Because cargo weight serves as the primary indicator of aircraft fuel consumption, which can also be directly triggerred higher total jet fuel consumption and carbon output. To show the correlation between projected TKP and future Greenhouse gas emissions, an operational Carbon Intensity (CI) factor has selected to elaborate the projected TKP and future CO_2 emissions using the formula as follows:

$$CI = \frac{\sum Total\ CO2\ Emissions}{\sum TKP} \tag{4}$$

where CI = the operational carbon intensity of the airline (in tons CO_2 / thousand TKP)
TKP = Total annual Ton-Kilometers Performed by the airline

Using the most recent available data in year 2025 recorded in Table 4 and Table 5 with the similar assumption for both airlines to maintain the current operational fleet sizes and present flight frequencies for calculating the carbon intensity, the calculated as follows:

- K-Mile Air (2025): $\frac{126{,}580}{156{,}850}$ = 0.807 tons of CO_2 / thousand TKP
- Pattaya Airways (2025): $\frac{5{,}050}{26{,}700}$ = 0.189 tons of CO_2 / thousand TKP

Based on the calculation above, K-Mile Air generated 0.807 tons of CO_2 / thousand TKP, whereas Pattaya Airways generated at a lower factor of 0.189 tons of CO_2 / thousand TKP in 2025 due to its turboprop configuration benefit. By projecting these 2025 carbon intensity factors across the CAAT "Base Case" cargo volume forecast, the future CO_2 emission for both airlines is mapped out through 2035 in Table 7.

Table 7. Projections of TKP and CO_2 Emissions (2025-2035)

Year	K-Mile Air		Pattaya Airways	
	Forecast TKP (Thousand)	Projected CO_2 Emission (Tons)	Forecast TKP (Thousand)	Projected CO_2 Emission (Tons)
2025	156,850	126,580	26,700	5,046
2026	167,986	135,565	28,595	5,404
2027	179,073	144,512	30,483	5,761
2028	190,176	153,472	32,372	6,118
2029	201,396	162,527	34,282	6,479
2030	209,049	168,703	35,585	6,726
2031	216,784	174,945	36,934	6,980
2032	224,371	181,067	38,227	7,225
2033	232,000	187,224	39,526	7,470
2034	239,656	193,402	40,831	7,717
2035	244,928	197,657	41,729	7,887

The data in Table 7 demonstrates an escalation of emissions for both airlines driven by the expansion of Forecast TKP. It was found that due to the weight of the cargo is a primary determinant of fuel burn, the more throughput will drive up total jet fuel consumption and, consequently, CO_2 output.

K-Mile Air's annual emissions are projected to rise from 126,578 tons in 2025 to 144,512 tons by the 2027 CORSIA mandatory transition point, and peaking to almost 200,000 tons by 2035. In contrast, Pattaya Airways's projected CO_2 emissions in 2035 still under 10,000 ton.

4.3 The Carbon Offset Demand and Domestic Carbon Market Supply

To evaluate the fesibility of local compliance for Thai-registered cargo airlines, the projected tansport demand from the airlines shall be compared against the capacity of Premium T-VER market. With the transition to the CORSIA mandatory phase in 2027, airlines are legally obligated to offset their emissions if their emissions exceed 10,000 Tons threshold. It is required to offset a portion of their emission amount calculated by applying with the Sector's Growth Factor (SGF) published annually by ICAO, to the airline's total eligible emissions.

Based on the projected CO_2 emission calculation in the Table 7, K-Mile Air's annual emission in 2027 is approximately 144,512 tCO_2. The determine carrier's offset liability under various global conditions, the three scenarios were set utilizing the most available official 2024 CORSIA Annual Sector's Growth Factor (SGF) equals to 0.15948315 [28] as a baseline, the offsetting amount required is calculated based on the formula below:

Offsetting Requirement (2024) = 2024 emissions x Global SGF 2024 (5)

Offsetting Requirement (2024) = 72,420 x 0.15948315 = 11,549.77 Tons

The number of offsetting requirements in year 2024 for K-Mile Air is 11,549.77 Tons. Therefore, this number is used as a base year for K-Mile Air and to be calcuated for future three predictive scenarios which are described below:

- Worst Case Scenario: assumming the global aviation sector struggles to reduce overall emissions, making the SGF to linearly increase by 0.5 percent annually.
- Base Case Scenario: assumming the SGF remains constant at the level of year 2024 throughout 2035.
- Best Case Scenario: assumning the global aviation sector able to decarbonize, resulting in the SGF linearly decreasing by 0.5 percent annually.

With all the conditions given for each scenario, the result of calculation are shown in Table 8.

Table 8. Projected Annual Carbon Offset Requirements for K-Mile Air by scenarios (2024-2035)

Year	Projected CO_2 Emission (Tons)	Worst Case Scenario		Base Case Scenario		Best Case Scenario	
		SGF (increase 0.5% / year)	Offseting Requirement (tCO_2 eq)	SGF (constant)	Offset Requirement (tCO_2 eq)	SGF (decrease 0.5% / year)	Offset Requirement (tCO_2 eq)
2024	72,420	0.15948315	11,549.77	0.15948315	11,549.77	0.15948315	11,549.77
2025	126,580	0.16448315	20,820.277	0.15948315	20,187.377	0.15948315	20,942.508
2026	135,565	0.16948315	22,975.983	0.15948315	21,620.333	0.15448315	21,602.109
2027	144,512	0.17448315	25,214.909	0.15948315	23,047.229	0.14948315	22,174.118
2028	153,472	0.17948315	27,545.638	0.15948315	24,476.198	0.14448315	22,669.778
2029	162,527	0.18448315	29,983.493	0.15948315	25,920.318	0.13948315	22,687.711
2030	168,703	0.18948315	31,966.376	0.15948315	26,905.286	0.13448315	22,652.430
2031	174,945	0.19448315	34,023.855	0.15948315	27,900.780	0.12948315	22,539.791
2032	181,067	0.19948315	36,119.816	0.15948315	28,877.136	0.12448315	22,370.113
2033	187,224	0.20448315	38,284.153	0.15948315	29,859.073	0.11948315	22,141.270
2034	193,402	0.20948315	40,514.460	0.15948315	30,844.360	0.11448315	21,640.111
2035	197,657	0.21448315	42,394.096	0.15948315	31,522.961	0.10948315	20,942.508

The projected value of Carbon Offsetting Requirements for K-Miles Air for each scenarios are visually illustrated in Figure 9.

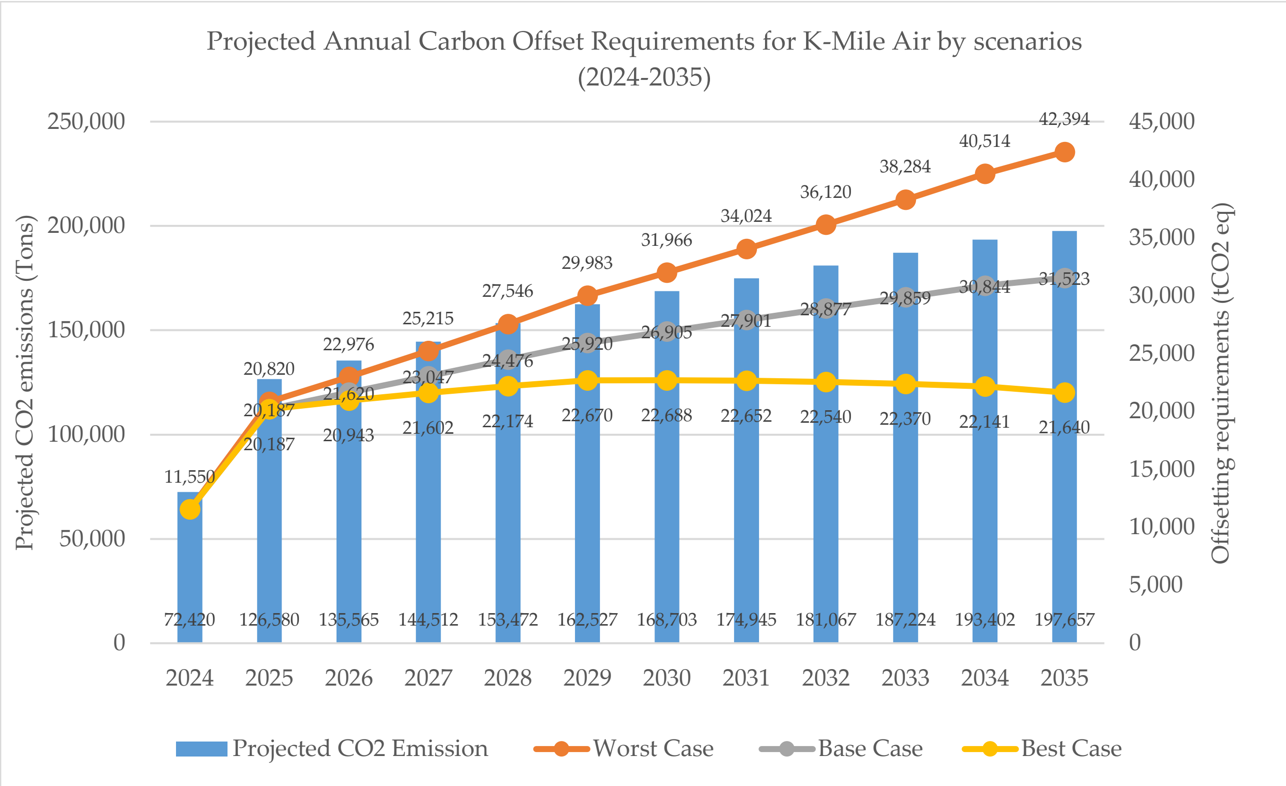

Figure 9. Projected Annual Carbon Offset Requirements for K-Mile Air by scenarios (2024-2035)

Under the Base Case, K-Mile Air would face a mandatory offset obligation of 23,047 tCO_2 in 2027 which is approximately equivalent to almost 90% of the total current projected supply for the Thai domestic carbon market (Premium T-VER) as per the Figure 4. However, under the Worst Case scenario, the SGF rises 0.17448315 by 2027, pushing the airlines's offset requirement up to 25,214.9 tCO_2. This number significantly showns the higher demand of offsetting which is about 98.5% of the total current projected supply in the market. Moreover, in Figure 9, by the end of 2035, K-Mile potentailly faces the offetting requirement up to 31,523 tCO_2 in base case, highlighting a critical bottleneck for supplying certified carbon credit from domestic market.

In contrast, Pattaya Airways' emissions in Table 7 recorded in 2027 are 5,761 tCO_2. As this figure falls below the 10,000-ton of the CORSIA threshold, Pattaya Airways is currently exempt from CORSIA mandatory offset obligations. Consequently, the airline is not required to apply to the SGF or submit annual carbon emissions verification report (MRV) to the regulator. However, given the rapid growth of Pattaya Airways, the airline remains a careful ongoing monitoring of their emission to ensure any potential exceeding emission in the future.

These finding demonstrate that the Premium T-VER which meet the criteria for CORSIA compliance, presents a severe bottleneck of supplying the credits. In Figure 8, it was identified a profound qualitative imbalance between the carbon credit within the domestic market because of only 1 Program of Activities (PoA) project that has been certified with the amount of 60 tCO_2eq/year. This means that the current certified supply of carbon credits represent less than 0.3% of the demand for just one major Thai cargo carrier. Addressing this concern requires proactive from the concern stakeholders, including CAAT and TGO. An immediate policy integration to scale the domestic supply of high-integrity credits, otherwise, Thai-registered cargo carriers will be forced to seek offsets in volatile international markets, resulting in a capital investment and international regulatory complication risks.

5. Conclusions

The research evaluated the carbon offset demand of Thai-registered cargo airlines within the ICAO CORSIA framework. Utilizing actual fuel consumption records from the Thai-registered cargo airlines through the "Fuel Allocation with Block Hour" methodology for the period of 2023 – 2025 successfully revealed that both K-Mile Air and Pattaya Airways exhibited a significant upward of the greenhouse gas (GHG) emissions from their operations which could lead to the future opreational risks for the airlines. The findings confirm that the rise of carbon output is primarily driven by an expanding regional e-commerce market and geopolitical conflicts from maritime logistics. When evaluated against Long-Term national demand forecast through 2035, the study demonstrates that the projected escalation in payload transport activities (TKP) could directly translates into a substaintial increase in CO_2 emissions.

- The GHG emissions from K-Mile Air, which mainly operates jet-engine aircraft, have significantly increased due to the fleet expansion and increased flight frequencies to meet e-commerce demand which led to the airline's performance at a high carbon intensity of 0.807 tons of CO_2 / thousand TKP in 2025. By 2027, the projected of K-Mile Air's annual emissions has reached to 144,512 tCO_2 exceeding the 10,000-tons CORSIA threshold for mandatory offsetting phase in 2027. Even the best case scenario, the offsetting requirements once utilizing CORSIA Annual Sector's Growth Factor (SGF) in 2027, the offsetting amount that K-Mile Air would be forced to offset 21,602 tCO_2 / year regardless of their own operational efficiencies.
- The GHG emissions from Pattaya Airways, which operates a turboprop aircraft, achieves a lower carbon intensity of 0.189 tons of CO_2 / thousand TKP than K-Mile Air. Nevertheless, the airline also has a major upward trend, rising from 460 tCO_2 in 2024 to 5,050 tCO_2 in 2025. This is due to the full-year operations of 2 (two) AT75 turboprop aircraft and could potentially led to 5,761 tCO_2 in 2027. Fortunately, the number still remains below the 10,000-ton exemption threshold for the entire CO_2 emission forecast, benefiting from the fuel efficiency of turboprop technology.

The study also identified K-Mile Air has the average age of the fleets at 24.3 years, while Pattaya Airways' fleet has an average age of 22 years. These numbers are closely aligned with the global industry benchmark of 25 years for dedicated cargo aircraft, supporting the fact that older aircraft are less fuel-efficient technology and generating more CO_2 emissions.

A critical finding of this study lies in the domestic carbon credit market constraints. The current and projected supply of eligible carbon credits from Premium T-VERs in Figure 4 possesses a total capacity of 25,633 tCO_2 eq/year. Under the Base Case scenario in 2027, K-Mile Air' offet demand alone would deplete nearly 90% of this entire domestic carbon supply and the Worst Case scenario, it would consume over 98%. It can be concluded that the current situation of market is insufficient to support Thai-registered cargo airlines' demand, especially, the national cargo volume forecast that would likely require Thai cargo airlines to increase their operations. With the regulatory transition, the upcoming CORSIA mandatory phase in 2027 would force all Thai airlines to offset their emission. Without an immediate policy support from TGO and CAAT to support this transition, the airlines would significantly experience a sharp increase of operational costs, and reduced financial profitability of the Thai cargo sector in the future. The airlines also will be forced to find eligible carbon credit from international market, which could lead to the regulatory complexity and compliance risks.

6. Acknowledgements

The authors would like to express their sincere gratitude to the operations and management teams of K-Mile Air and Pattaya Airways for their invaluable cooperation, and for providing the data in CAAT Form M – Aircraft Fuel Consumption and Traffic – Commercial Air Carriers unitl 2025 for this research. The authors acknowledge the College of Interdisciplinary and Integrative Studies and the Energy Research Institute at Chulalongkorn University for providing the academic facilities, resources, and technical support. The author also extend gratitude to his academic advsior, Dr. Jakapong Pongthanaisawan, for his guidance, continous encouragement, and invaluable technical assistance thorughout the development of this study.

References

[1] International Air Transport Association. 2025 Vision for the Future of Air Cargo Facilities: Reimagining Logistics Through Technology and Innovation; International Air Transport Association, 2025. https://www.iata.org/contentassets/ea370e43f1e84cf6835650c2bec61885/2025-vision-for-the-future-of-air-cargo-facilities---reimagining-logistics-through-technology-and-innovation.pdf.

[2] International Air Transport Association. Fact sheet: CORSIA; 2025. www.iata.org/en/iata-repository/pressroom/fact-sheets/fact-sheet-corsia/.

[3] International Civil Aviation Organization. ICAO Member States. International Civil Aviation Organization,, 2026. https://www.icao.int/about-icao/member-states (accessed).

[4] International Air Transport Association. The older cargo fleet hampers emissions reductions. International Air Transport Association, 2024. https://www.iata.org/en/iata-repository/publications/economic-reports/the-older-cargo-fleet-hampers-emissions-reductions/ (accessed).

[5] Thailand Greenhouse Gas Management Organization. What is T-VER? Thailand Greenhouse Gas Management Organization, 2016. https://ghgreduction.tgo.or.th/en/what-is-t-ver/what-is-t-ver.html (accessed).

[6] International Air Transport Association. The Value of Air Transport to Singapore; 2024. https://www.iata.org/en/iata-repository/publications/economic-reports/the-value-of-air-transport-to-singapore/.

[7] International Air Transport Association. The Value of Air Transport to Indonesia; 2024. https://www.iata.org/en/iata-repository/publications/economic-reports/the-value-of-air-transport-to-indonesia/.

[8] International Air Transport Association. The Value of Air Transport to Vietnam; 2024. https://www.iata.org/en/iata-repository/publications/economic-reports/the-value-of-air-transport-to-vietnam/.

[9] International Air Transport Association. The Value of Air Transport to Thailand; 2024. https://www.iata.org/en/iata-repository/publications/economic-reports/the-value-of-air-transport-to-thailand/.

[10] Nation Thailand. Thai Air Transport Set for Take-Off as Post-Pandemic Demand Soars. 2025. https://www.nationthailand.com/business/economy/40049260?utm_source=chatgpt.com.

[11] International Air Transport Association. The Value of Air Transport to Malaysia; International Air Transport Association,, 2024. https://www.iata.org/en/iata-repository/publications/economic-reports/the-value-of-air-transport-to-malaysia/.

[12] International Air Transport Association. The Value of Air Transport to the Philippines; International Air Transport Association, 2024. https://www.iata.org/en/iata-repository/publications/economic-reports/the-value-of-air-transport-to-the-philippines/.

[13] International Air Transport Association. Our Commitment to Fly Net Zero by 2050. 2021. https://www.iata.org/en/programs/sustainability/flynetzero/ (accessed).

[14] International Air Transport Association. Net zero 2050: sustainable aviation fuels (SAF); International Air Transport Association, 2025. https://www.iata.org/en/iata-repository/pressroom/fact-sheets/fact-sheet-sustainable-aviation-fuels/.

[15] International Civil Aviation Organization. SAF Conversion Processes. International Civil Aviation Organization,, 2023. https://www.icao.int/SAF/saf-conversion-processes (accessed).
[16] Roland Berger. Hydrogen: A future fuel for aviation?; 2020.
[17] Naqvi, A. A.; Zahoor, A.; Shaikh, A. A.; Butt, F. A.; Raza, F.; Ahad, I. U. Aprotic lithium air batteries with oxygen-selective membranes. Materials for Renewable and Sustainable Energy 2022, 11 (1), 33–46.
[18] International Air Transport Association. Net zero 2050: operational & infrastructure improvements; 2025. https://www.iata.org/en/iata-repository/pressroom/fact-sheets/fact-sheet-netzero-operations-infrastructure/.
[19] International Civil Aviation Organization. CORSIA Eligible Emissions Units; 2025. https://www.icao.int/sites/default/files/environmental-protection/CORSIA/Documents/CORSIA-Eligible-Emissions-Units_Oct2025.pdf.
[20] Zhang, J.; Zhang, S.; Wu, R.; Duan, M.; Zhang, D.; Wu, Y.; Hao, J. The new CORSIA baseline has limited motivation to promote the green recovery of global aviation. Environmental pollution 2021, 289, 117833.
[21] International Air Transport Association. CORSIA Handbook; 2024.
[22] Strouhal, M. CORSIA-carbon offsetting and reduction scheme for international aviation. MAD-Magazine of Aviation Development 2020, 8 (1), 23–28.
[23] Thailand Greenhouse Gas Management Organization. Guideline for Premium Thailand Voluntary Emission Reduction Program (Premium T-VER); TGO, 2025.
[24] International Civil Aviation Organization. CORSIA Newletter: October 2025; International Civil Aviation Organization,, 2025. https://www.icao.int/sites/default/files/environmental-protection/CORSIA/Newsletter/CORSIAnewsletter_OCT2025.pdf?fbclid=IwY2xjawOIF0NleHRuA2FlbQIxMABicmlkETFtdkYzaThyNUx0a1A0WVcyc3J0YwZhcHBfaWQQMjIyMDM5MTc4ODIwMDg5MghjYWxsc2l0ZQEyAAEeUNkwFKS5FCMWIh6niw-0KgRhvqIbeHP5DiwjDPwdFzeeB7p-IxHcRzq42Dk_aem_cOVS1EsOzX8Ir7II74Kprw.
[25] Thailand Greenhouse Gas Management Organization. Premium T-VER Statistics of Registered Projects. Thailand Greenhouse Gas Management Organization,, 2026. https://ghgreduction.tgo.or.th/th/database-and-statistics/statistics-of-registered-projects.html (accessed).
[26] The Civil Aviation Authority of Thailand. State of Thai Aviation Industry 2024; The Civil Aviation Authority of Thailand (CAAT), 2024.
[27] Working Group for National Air Travel Demand Forecasting. CAAT Report on National Air Travel Demand Forecasting 2025; 2025.
[28] International Civil Aviation Organization. CORSIA Annual Sector's Growth Factor (SGF); 2025.https://www.icao.int/sites/default/files/environmentalprotection/CORSIA/Documents/CORSIA%20Central%20Registry/CORSIA-Annual-SGF-4ed-2025-web.pdf.

Effect of Variable Flow Rates on PET Microplastic Filtration Efficiency Using Quartz Gravel Media in Synthetic Stormwater Runoff

Tianchai Mungkhalad[1], Jenyuk Lohwacharin[2,3*]

[1] Department of Environmental and Sustainable Engineering, Faculty of Engineering, Chulalongkorn University, 254 Phayathai Road, Pathumwan, Bangkok 10330, Thailand
[2] Department of Environmental and Sustainable Engineering, Faculty of Engineering, Chulalongkorn University254 Phayathai Road, Pathumwan, Bangkok 10330, Thailand
[3] Professor Aroon Sorathesn Center of Excellence in Environmental Engineering, Department of Environmental and Sustainable Engineering, Faculty of Engineering, Chulalongkorn University, Bangkok, 10330, Thailand
* Correspondence: Jenyuk.L@chula.ac.th

Abstract

The contamination of aquatic environments by microplastics (MPs) via urban stormwater runoff has gained increasing attention. Granular filter media is considered as a potential mitigation measure. However, the influence of hydraulic variability on the MP retention remains insufficiently characterized. We examined relations between stormwater runoff flow regimes and the breakthrough of polyethylene terephthalate (PET) MPs with an average size of 53.72 ± 12.13 µm through a quartz gravel filter medium with a grain size of 1–2 mm. To simulate a 2-hour stormwater runoff event, each flow condition is divided into four consecutive 30-minute intervals, yielding four flow rate values per condition; i.e., constant low-flow (5-5-5-5 mL/min), initial high-flow (25-5-5-5 mL/min), and intermittent flow (5-25-5-25 mL/min). Effluent samples were collected at the end of each interval to evaluate MP breakthrough over time. The results show that stable low flow conditions produced the lowest breakthrough, while sudden increases in flow rate significantly enhanced particle passage. The initial high-flow condition generated the highest breakthrough during the first interval, whereas intermittent flow conditions resulted in repeated breakthrough peaks. The findings suggest that hydraulic disturbances strongly influence MPs transport and retention in granular filtration systems. This study provides insights into the performance of quartz gravel filters under dynamic stormwater conditions, demonstrating that hydraulic fluctuations significantly compromise the retention capacity of granular filter media. Besides, controlling an influent flow rate is mandatory for the stabilization of filtration system.

Keywords: microplastics, polyethylene terephthalate, stormwater runoff, quartz gravel, filtration

1. Introduction

The large-scale buildup of plastic waste in the environment has been a major scientific and public concern in recent decades. Microplastics (MPs), defined as plastic particles smaller than 5 mm, are among the plastic pollution types and the most ubiquitous pollutants in terrestrial, freshwater, and marine environments[1]. Their small size, chemical persistence, and capacity to adsorb toxic pollutants make them especially dangerous for aquatic organisms and thus to human health throughout the food chain[2]. PET is among the most commonly detected MP polymer types in environmental samples due to the widespread use of PET in single-use beverage bottles, textile fibers, and packaging materials[3]

Urban stormwater runoff has become one of the emerging routes through which MPs are moved from Earth's terrestrial areas to the receiving water bodies[4]. On the one hand, surface runoff contributes to the accumulation of MPs deposited on impervious surfaces like roads, parking lots, and rooftops during rainfall events, while the particles are discharged into the drainage systems and natural aquatic water systems in various ways[5]. It has been shown that substantial MP load is borne by the stormwater discharges. The rates of MP load levels of discharge differ greatly depending on land use, rainfall intensity, and antecedent dry period[6]. E.g., MP content (1.1–24.6 particles/L) detected in 12 urban streams was linked to PET being among the most abundant polymer kinds, and watershed imperviousness predicted MP loading considerably. This means of transport accentuates the need for efficient stormwater treatment approaches to sequester MPs before the waterway[7]. This transport mechanism highlights the urgent requirement of effective stormwater treatment strategies capable of capturing MPs prior to their entry into aquatic environments.

Based on these issues, granular filtration technology provides economical means for the removal of MPs as a practical measure for stormwater treatment system in the form of bioretention systems and sand filters, as well as permeable pavement[8]. Quartz gravel is one of the filter media used in water treatment on account of its chemical inertness, mechanical durability, and wide availability. Laboratory-scale studies have confirmed that granular media can achieve measurable retention of MPs through physical mechanisms including mechanical straining, interception, and gravitational sedimentation[9]. However, the retention efficiency of granular filters is not constant and is known to be influenced by particle size, shape, surface properties, and the hydraulic conditions under which filtration occurs [10].

The hydraulic loading rate is a crucial operating parameter in granular filtration systems, because it controls the hydrodynamic forces on particles within the filter bed. With high flow, the shearing forces may overcome the adhesive interactions between MPs and filter grains, leading to increased breakthrough[11]. In the context of stormwater management, flow rates are inherently variable and subject to episodic surges corresponding to rainfall events of differing intensity and duration. This study, hence, was to examine the effect of synthetic stormwater runoff flow rate patterns on the breakthrough behavior of PET (~50 μm) through a quartz gravel filter medium. Three hydraulic loading scenarios were implemented to reflect constant low-flow, initial high-flow, and intermittent flow conditions, reflecting the various hydrological phenomena present in urban catchments. Therefore, the results of this study will provide a better understanding of the hydraulic drivers of MP retention present in granular filter systems and directly inform stormwater treatment system design and optimization.

2. Materials and Methods.

2.1 Materials

PET MPs, with approximate size ~50 μm, were purchased from Cheung Muk Tau Hengli New Materials (China). Quartz gravel, with sieve size 1-2 mm, were purchased from an online retailer and supplied by Herosign Marketing Co., Ltd (Thailand)

2.2 Filtration media

1–2 mm quartz gravel was used as the filtration media in this study. The gravel was washed with tap water followed by deionized water to remove the fine particles and impurities. The cleaned media was dried in an oven at 105 °C for 4 h before being packed into the filtration column.

2.3 Synthetic Stormwater and MPs

PET MPs with an average size of 53.72 ± 12.13 μm were used in this study. Prior to the experiment, PET MPs were washed with a 75% ethanol solution to remove potential contaminants and impurities on the particle surfaces. The washed MPs were then dried in an oven at 45 °C for 24 h.

Synthetic stormwater runoff was prepared using deionized water as the base solution. The composition of the synthetic stormwater consisted of glucose at 0.047 g/L, NH_4Cl at 0.019 g/L, KNO_3 at 0.050 g/L, and KH_2PO_4 at 0.0035 g/L. After preparation, the dried PET MPs were added to the synthetic stormwater and continuously mixed using a magnetic stirrer to maintain a homogeneous suspension and minimize particle sedimentation during the filtration experiment.

2.4 Experimental setup

The experiment was conducted using a laboratory-scale vertical glass column with an inner diameter of 1.9 cm. The column was packed with quartz gravel media to a bed height of 10 cm. A stainless-steel mesh with an opening size of 0.2 mm was installed at the bottom section of the column to support and retain the media while allowing water to pass through the system. Deionized water was continuously pumped into the experimental column for 24 hours. This pre-conditioning step was conducted to ensure full saturation of the porous media, eliminate any entrapped air bubbles, and stabilize the hydraulic structure of the filter bed.

The influent synthetic stormwater containing PET MPs was introduced into the column through silicone tubing connected to a peristaltic pump, which was used to control the flow rate during the experiment. The influent was introduced from the upper part of the column, and the flow passed downward through the quartz gravel media under gravitational force. The effluent was collected from the outlet at the bottom of the column using glass collection bottles. Effluent samples were collected at 30-minute intervals to evaluate the breakthrough behavior of PET MPs under different flow patterns. A schematic of the experimental setup is shown in Figure 1.

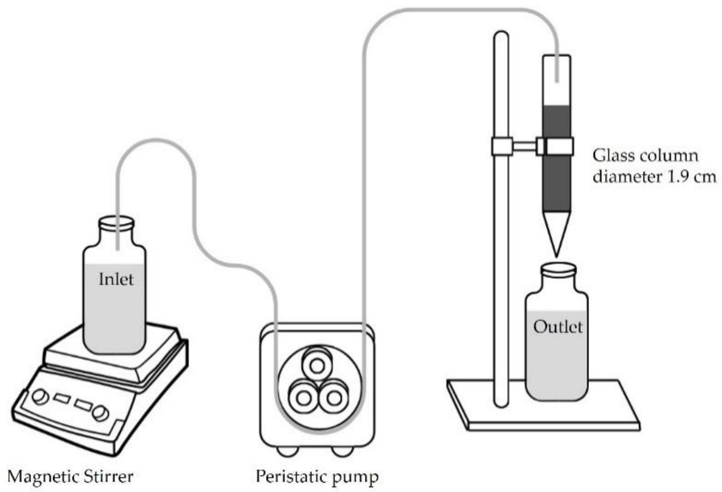

Figure 1. Schematic diagram of the glass column experimental setup

2.5 MPs analysis

Effluent samples collected at each interval were stored in glass bottles. Each sample was subsequently filtered through a Whatman cellulose ester membrane filter with grid markings using a vacuum pump. The filters were then transferred onto petri dishes and allowed to dry at room temperature. Once dried, MP particles retained on the filter surface were enumerated under a FT-IR microscope spectrometer (Bruker Lumos II, Bruker Optik GmbH, Germany).

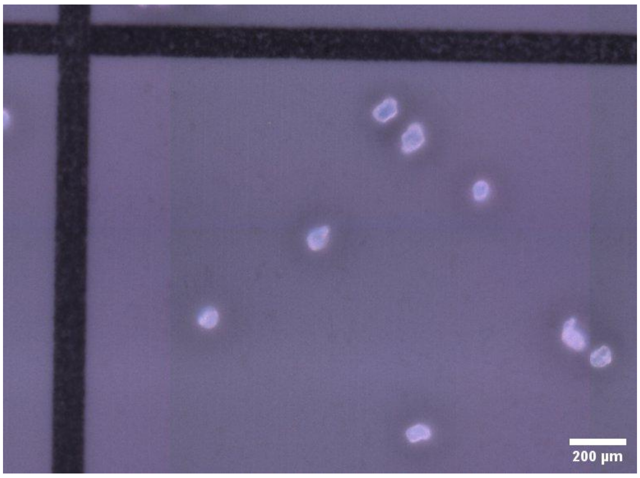

Figure 2. Representative microscopy image of PET MPs

MPs identification was not performed in this study, as the MP type was predefined as PET. PET MPs used in this study were distinguishable from naturally occurring particulate matter by their characteristic size, morphology, and color, enabling unambiguous visual enumeration without spectroscopic confirmation. Representative microscopic images of the PET used in this study are presented in Figure 2.

2.6 Contamination prevention

To minimize the risk of undesirable MP contamination during the experimental process, all tools that came into direct contact with samples, such as filtration systems, collection containers, and transfer instruments, were made of glass or stainless steel; plastic laboratory equipment was avoided whenever feasible. The experimental setup was also covered with aluminum foil during column operations to prevent airborne particles from settling on exposed areas. Blanks were performed for each sampling interval across all experimental conditions.

Blank samples were created and treated using the same methods applied to the experimental samples. A microscopic analysis of all blank filters showed no detectable PET MPs, indicating that background contamination from lab procedures or airborne sources did not influence the MP counts reported in this research.

3. Results and Discussion

3.1 Filter media analysis

Filter media analysis includes both sieve analysis and the examination of filter media distribution. The sieve analysis was performed using a mechanical sieve analyzer, with the results represented in the accumulation curve of the filter media distribution. From this graph, values for effective size (ES = D_{10}) and uniformity coefficient (UC = D_{60}/D_{10}) of the filter media were determined. The values of porosity and density were determined using equations (1) and (2), respectively. The outcomes of the filter media analysis are presented in Table 1.

$$\text{porosity } (\varepsilon) = \frac{\text{void volume}}{\text{filter media volume}} \quad (1)$$

$$\text{density } (\rho) = \frac{\text{filter media mass}}{\text{filter media volume}} \quad (2)$$

Table 1. Properties of the filter media

Property	Value	Unit	Method
Effective size (ES)	1.22	mm	Sieve analysis
Uniformity coefficient (UC)	1.28	mm	Sieve analysis
Bed porosity (ε)	0.36	-	Calculated
Density (ρ)	1.53	g/cm^3	Calculated

3.2 MPs characterization

The MPs used in this study were characterized based on size, morphology, color, and polymer identity before the filtration experiments. Particle size was determined by microscopic analysis using the particle size measurement tool in OPUS software (version 8.5.29), measurement of 100 randomly selected particles yielded a mean particle diameter of 53.72 ± 12.13 µm, confirming that the particles were within the target size range of approximately 50 µm. The particles exhibited a predominantly sub-spherical morphology with translucent to white coloration, properties that are visually distinct from naturally occurring particulate matter, thereby facilitating unambiguous identification during microscopic enumeration.

Polymer identity was verified by FTIR spectroscopy using a Bruker Lumos II FTIR microscope spectrometer. The obtained spectra were compared to a reference spectral library, and the resulting matches confirmed the particles to be PET. The FTIR spectrum of the PET MPs exhibited characteristic absorption bands consistent with the known spectral signature of polyethylene terephthalate. Prominent absorption peaks were observed at 1707 cm^{-1}, corresponding to the C=O stretching vibration of the ester carbonyl group, which is the most diagnostic band for PET identification. Additional characteristic bands were identified at 1236 cm^{-1} and 1094 cm^{-1}, attributed to the asymmetric and symmetric C–O–C stretching vibrations of the ester linkage, respectively. Furthermore, a C–H stretching absorption was detected at 2969 cm^{-1}, attributed to the aliphatic C–H stretching vibration of the ethylene glycol unit within the PET backbone. The corresponding FTIR spectra of the MPs are presented in Figure 3.

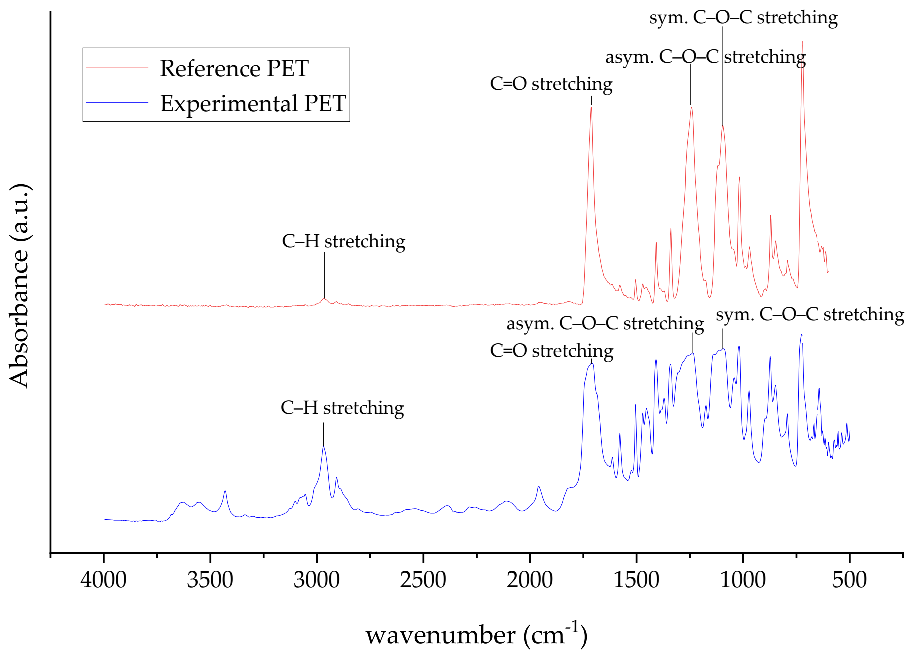

Figure 3. Comparison of FTIR spectra between experimental PET and the reference PET

3.3 Retention and release of MPs

The quartz gravel filter demonstrated high MP retention for all three hydraulic loading scenarios, with cumulative breakthroughs of 37, 52, and 69 particles recorded for the constant low-flow scenario, initial high-flow scenario and intermittent flow scenario, respectively, out of a total input of 2,417 particles/L. Despite these differences in absolute breakthrough counts, the overall removal efficiency throughout all scenarios exceeded 99%, as shown in Table 2, calculated according to equation (3), indicating that quartz gravel with a grain size of 1–2 mm is an effective physical barrier against PET MPs of approximately 50 µm under the flow conditions tested. The primary retention mechanism is attributed to mechanical straining, whereby particles smaller than the pore throat diameter are nevertheless captured through a combination of interception, gravitational sedimentation within pore spaces, and surface adhesion between MPs and grain surfaces [12]. The sub-spherical morphology and relatively uniform size of the MPs used in this study (~53.72 ± 12.13 µm) likely contributed to their consistent retention behavior, as near-spherical particles have been reported to exhibit more predictable transport and deposition patterns in granular media compared to irregularly shaped or fibrous MPs [13]. The quantities of MPs found in the effluent are reported in Table 3.

$$\%\ \text{Removal effiviency} = \frac{\text{initial MPs concentration - final MPs concentration}}{\text{initial MPs concentration}} \text{ x } 100 \qquad (3)$$

Table 2. Calculation results of MP removal efficiency

Condition	Total No. of MPs in the effluent (particles)	Total volume in effluent (L)	removal efficiency (%)
constant low-flow	37	18	99.91
initial high-flow	52	36	99.94
intermittent flow	69	54	99.95

Table 3. Number of MPs collected from the effluent

Time	0-30 min		31-60 min		61-90 min		91-120 min	
Condition	flow rate (mL/min)	number of MPs	flow rate (mL/min)	number of MPs	flow rate (mL/min)	number of MPs	flow rate (mL/min)	number of MPs
constant low-flow	5	3.67 ± 0.58	5	3.00	5	2.67 ± 0.58	5	3.00
initial high-flow	25	9.67 ± 1.15	5	2.67 ± 0.58	5	2.33 ± 0.58	5	2.67 ± 1.53
intermittent flow	5	2.67 ± 1.15	25	8.00 ± 1.00	5	2.33 ± 0.58	25	10.00 ± 1.00

Although overall removal efficiency was high across all scenarios, a clear and systematic relationship between hydraulic loading rate and MP breakthrough was observed. The low-flow scenario, representing constant low-flow conditions (5–5–5–5 mL/min), yielded the lowest cumulative breakthrough of 37 particles and the most temporally uniform release pattern, indicative of a system operating under stable hydrodynamic equilibrium. Under these conditions, the low pore-water velocity generates minimal fluid shear forces within the filter bed, allowing MPs to settle and adhere to grain surfaces without significant mobilization. This observation is consistent with the findings of Xu et al. [11], who demonstrated that lower flow rates promote stable retention of MPs in saturated porous media by maintaining the trapping efficiency of transition pores, and that the consistency between flow field and particle flux field is highest under low-flow conditions.

In the initial high-flow scenario, characterized by an initial high flow rate of 25 mL/min followed by sustained low flow (25–5–5–5 mL/min), breakthrough was markedly elevated during the first sampling interval (9.67 ± 1.15 particles), before declining to a low and stable level in subsequent intervals (2.67 ± 0.58 – 2.33 ± 0.58 – 2.67 ± 1.53 particles). The disproportionately high initial breakthrough suggests that the sudden application of high hydraulic loading at the onset of the experiment generated sufficient hydrodynamic shear to mobilize MP particles that would otherwise have been retained under low-flow conditions. This phenomenon is analogous to the first flush effect widely documented in stormwater quality research, wherein the initial pulse of runoff mobilizes accumulated contaminants from catchment surfaces and conveyance infrastructure [7], and aligns with findings by Ahmad et al. [14], who reported elevated MP concentrations in filter effluents immediately following hydraulic surge events in green infrastructure systems. In the context of granular filtration, the initial surge may also have disturbed the equilibrium state of newly deposited particles within transition pores before stable retention could be established, resulting in elevated particle's local flux through the filter bed. Following the reduction in flow rate from the second interval onward, breakthrough returned to levels comparable to those observed in low-flow scenario, suggesting that the filter recovered its retention capacity once hydrodynamic shear forces were reduced.

Intermittent flow scenario, involving intermittent flow (5–25–5–25 mL/min), produced the highest cumulative breakthrough of 69 particles and the most variable temporal pattern, with breakthrough counts of 2.67 ± 1.15, 8.00 ± 1.00, 2.33 ± 0.58, and 10.00 ± 1.00 particles at the first through fourth intervals, respectively. Importantly, the elevated breakthrough values at the second and fourth intervals corresponded directly to the high-flow intervals of the experimental sequence, while the low-flow intervals (first and third) were associated with markedly lower breakthrough. A bar chart comparing the three scenarios is shown in Figure 4. This strong temporal correspondence between hydraulic surge and MP release provides compelling evidence that repeated increases in flow velocity induce re-mobilization of previously retained MPs from within the filter bed. Xu et al. [11] documented analogous re-migration events in saturated porous media using two-dimensional flow cell experiments, providing direct visual evidence that retained MPs detach from pore throats and resume transport when pore water velocity exceeds a critical threshold, resulting in abrupt changes in

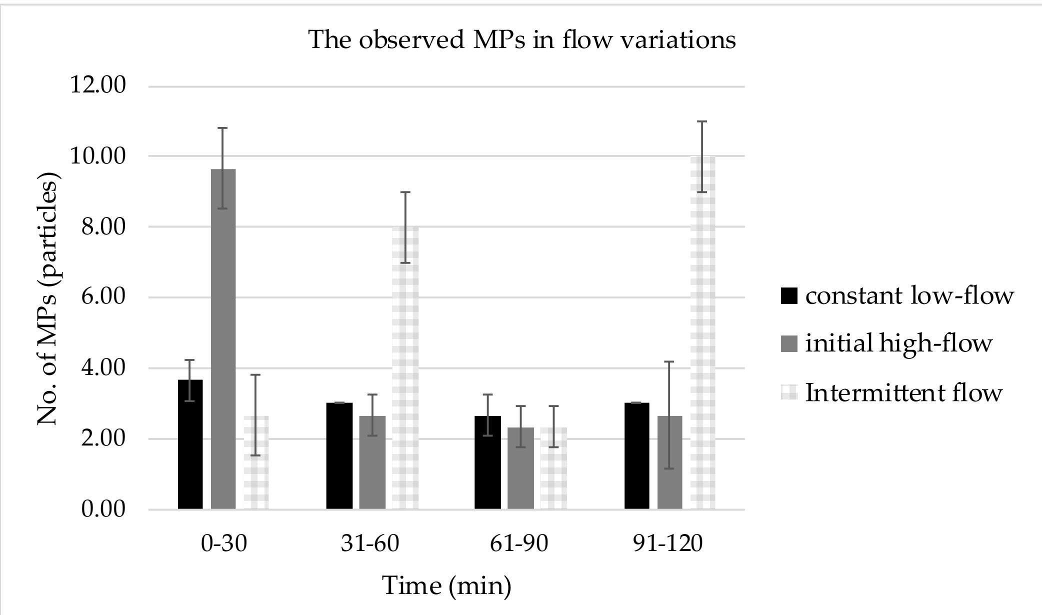

Figure 4. Microplastic release into the effluent under different scenarios

both flow rate and particle flux within the porous matrix. The recurrence of elevated breakthrough at the fourth interval, despite prior exposure to a surge at the second interval, further indicates that the filter continued to accumulate and re-mobilize MPs with each successive hydraulic pulse, rather than reaching a depleted retention state.

The difference between the initial high-flow scenario and the Intermittent flow scenario is particularly instructive. While both scenarios involved a flow rate of 25 mL/min, the single initial surge in initial high-flow scenario resulted in lower total breakthrough (52 particles) compared to the repeated surges in intermittent flow scenario (69 particles). This suggests that the cumulative effect of intermittent high-flow events is may adversely affect to filter retention performance than a single surge of equivalent magnitude, likely because each hydraulic pulse re-engages a new population of loosely retained particles that had been deposited during the preceding low-flow interval. This finding has practical implications for the design of stormwater filtration systems in urban catchments, where rainfall events of varying intensity produce intermittent and episodic hydraulic loading patterns rather than steady-state conditions [7]. The results suggest that filter systems designed solely on the basis of steady-state hydraulic performance may underestimate MP breakthrough under realistic stormwater loading conditions.

From a pore-scale perspective, the observed breakthrough patterns are consistent with the conceptual framework proposed by Xu et al. [11] , wherein MP retention in granular media is governed by the balance between particle flux and pore flow velocity within transition pores, in which retention is conditional rather than absolute. Under low-flow conditions, the flux-to-velocity ratio favors stable retention, whereas under high-flow conditions, elevated pore velocity reduces the residence time of MPs on grain surfaces and promotes detachment, as reflected by the increased spatial heterogeneity of particle distribution observed at higher flow rates. The significance of particle morphology is pertinent in this context, as it has been shown that retention mechanisms within porous media vary fundamentally between spherical and fibrous MPs. Specifically, the retention of fibers is more significantly influenced by size-exclusion effects and the geometry of pores [13]. Consequently, the predominantly sub-spherical PET MPs utilized in this study are anticipated to be more vulnerable to hydrodynamic re-mobilization compared to their fibrous counterparts. This increased susceptibility arises from their smooth surfaces and compact form, which reduces mechanical interlocking with adjacent grain surfaces.

In summary, the results of this study demonstrate that while quartz gravel filtration achieves high MP retention under all tested hydraulic conditions, the magnitude and temporal pattern of breakthrough are significantly influenced by the flow rate regime. Constant low-flow conditions optimize filter retention performance, whereas intermittent surge conditions representative of urban stormwater events increase cumulative breakthrough through repeated re-mobilization of retained particles. These findings underscore the importance of incorporating hydraulic variability into the evaluation and design of granular filter systems intended for MP removal in stormwater management applications.

4. Conclusions

This study investigated the effect of synthetic stormwater runoff flow rate on the retention and breakthrough behavior of PET MPs through a quartz gravel filter medium under three distinct hydraulic loading scenarios. All three scenarios demonstrated consistently high MP retention, with cumulative breakthrough of 37, 52, and 69 particles recorded for low-flow condition (5–5–5–5 mL/min), initial high-flow condition (25–5–5–5 mL/min), and intermittent flow condition (5–25–5–25 mL/min), respectively, against a total input concentration of 2,417 particles/L. These results confirm that quartz gravel is capable of functioning as an effective physical barrier against PET MPs under all tested conditions. However, the magnitude and temporal distribution of breakthroughs were significantly governed by the hydraulic loading pattern. Constant low-flow conditions yielded the lowest and most uniform breakthrough, while initial high-flow and intermittent flow conditions produced progressively elevated and temporally variable breakthrough, attributable to hydraulic shear-induced mobilization and repeated re-mobilization of previously retained particles within the filter bed.

Overall, this study lies in demonstrating that granular filter performance under variable hydraulic loading, representative of real urban stormwater conditions, cannot be reliably predicted from steady-state assessments alone. Intermittent flow conditions, in particular, were shown to be the most detrimental to filter retention efficiency, a finding with direct implications for the hydraulic design of granular filtration components within Low Impact Development (LID) stormwater management infrastructure.

5. Acknowledgements

The corresponding author thanks to Chulalongkorn University Office of International Affairs and Global Network Scholarship for International Research Collaboration for financial support for “Chula International Research & Innovation Visibility: Chula International Research Trip” fund.

References

[1] Thompson, R. C.; Swan, S. H.; Moore, C. J.; vom Saal, F. S. Our plastic age. Philos. Trans. R. Soc. Lond. B Biol. Sci. 2009, 364 (1526), 1973-1976. DOI: 10.1098/rstb.2009.0054 From NLM Medline.

[2] Eerkes-Medrano, D.; Thompson, R. C.; Aldridge, D. C. MPs in freshwater systems: a review of the emerging threats, identification of knowledge gaps and prioritisation of research needs. Water Res 2015, 75, 63-82. DOI: 10.1016/j.watres.2015.02.012 From NLM Medline.

[3] Geyer, R.; Jambeck, R. J.; Law, L. K. Production, use, and fate of all plastics ever made. Science Advances 2017, 3 (7). DOI: 10.1126/sciadv.1700782.

[4] Carr, S. A.; Liu, J.; Tesoro, A. G. Transport and fate of MP particles in wastewater treatment plants. Water Res 2016, 91, 174-182. DOI: 10.1016/j.watres.2016.01.002 From NLM Medline.

[5] Dris, R.; Gasperi, J.; Rocher, V.; Tassin, B. Synthetic and non-synthetic anthropogenic fibers in a river under the impact of Paris Megacity: Sampling methodological aspects and flux estimations. Sci Total Environ 2018, 618, 157-164. DOI: 10.1016/j.scitotenv.2017.11.009 From NLM PubMed-not-MEDLINE.

[6] Liu, F.; Olesen, K. B.; Borregaard, A. R.; Vollertsen, J. MPs in urban and highway stormwater retention ponds. Science of The Total Environment 2019, 671, 992-1000. DOI: 10.1016/j.scitotenv.2019.03.416.

[7] Werbowski, L. M.; Gilbreath, A. N.; Munno, K.; Zhu, X.; Grbic, J.; Wu, T.; Sutton, R.; Sedlak, M. D.; Deshpande, A. D.; Rochman, C. M. Urban Stormwater Runoff: A Major Pathway for Anthropogenic Particles, Black Rubbery Fragments, and Other Types of MPs to Urban Receiving Waters. ACS ES&T Water 2021, 1 (6), 1420-1428. DOI: 10.1021/acsestwater.1c00017.

[8] Lapointe, M.; Farner, J. M.; Hernandez, L. M.; Tufenkji, N. Understanding and Improving MP Removal during Water Treatment: Impact of Coagulation and Flocculation. Environ Sci Technol 2020, 54 (14), 8719-8727. DOI: 10.1021/acs.est.0c00712 From NLM Medline.

[9] Bayo, J.; Olmos, S.; Lopez-Castellanos, J. MPs in an urban wastewater treatment plant: The influence of physicochemical parameters and environmental factors. Chemosphere 2020, 238, 124593. DOI: 10.1016/j.chemosphere.2019.124593 From NLM Medline.

[10] He, D.; Zhang, X.; Hu, J. Methods for separating MPs from complex solid matrices: Comparative analysis. J Hazard Mater 2021, 409, 124640. DOI: 10.1016/j.jhazmat.2020.124640 From NLM PubMed-not-MEDLINE.

[11] Xu, H.; Tang, P.; Zhou, Y.; Zhang, Y.; Zhang, T. Effects of pore water flow rate on MPs transport in saturated porous media: Spatial distribution analysis. J Hazard Mater 2025, 489, 137511. DOI: 10.1016/j.jhazmat.2025.137511 From NLM PubMed-not-MEDLINE.
[12] Puteri, M. N.; Gew, L. T.; Ong, H. C.; Ming, L. C. Technologies to eliminate MP from water: Current approaches and future prospects. Environ Int 2025, 199, 109397. DOI: 10.1016/j.envint.2025.109397 From NLM Medline.
[13] Cohen, N.; Edery, Y.; Radian, A. Pore-Scale Insights into MP Fiber Transport and Retention in Porous Media. Environ Sci Technol 2025, 59 (50), 27657-27667. DOI: 10.1021/acs.est.5c12359 From NLM Medline.
[14] Ahmad, T.; Gul, S.; Peng, L.; Mehmood, T.; Huang, Q.; Ahmad, A.; Ali, H.; Ali, W.; Souissi, S.; Zinck, P. MP mitigation in urban stormwater using green infrastructure: a review. Environmental Chemistry Letters 2025, 23 (4), 999-1024. DOI: 10.1007/s10311-025-01833-8.

Performance and Energy Saving Analysis of a Chiller after Variable Speed Drive Installation

Yanin Sinphai[1], Sirima Panyametheekul[2*]

[1] Energy Technology and Management, College of Interdisciplinary and Integrative Studies, Chulalongkorn University
[2] Department of Environmental and Sustainable Engineering
*Correspondence: 6682009720@student.chula.ac.th

Abstract

This research aims to evaluate the energy-saving potential, economic feasibility, and environmental impacts of installing a Variable Frequency Drive (VFD) in a water-cooled chiller system used in a commercial building. A Carrier 19XR water-cooled chiller with a cooling capacity of 500 refrigeration tons was selected as the case study. Actual operating data were collected from the Chiller Plant Management System (CPMS) over a one-year period. The data included operating load, operating hours, electric current, and electricity consumption. These data were analyzed to examine the energy consumption pattern, chiller performance, and the effects of VFD installation. The results showed that the chiller frequently operated under partial-load conditions. Therefore, the installation of a VFD enabled the motor speed to be adjusted in accordance with the actual cooling load. This resulted in a tendency toward reduced electric current and electricity consumption. In addition, the reduction in energy consumption contributed to lower electricity costs, improved economic feasibility, and reduced greenhouse gas emissions associated with electricity use. The findings indicate that VFD installation is an appropriate approach for improving the efficiency of air-conditioning systems in large buildings and supporting sustainable energy management in the long term.

Keywords: Variable Frequency Drive; Water-cooled Chiller; Energy Saving; Economic Feasibility; Greenhouse Gas Emission Reduction

1. Introduction

Air-conditioning systems play a highly important role in creating suitable indoor environmental conditions for living and working, particularly in medium- to large-sized office buildings, hospitals, industrial facilities, and shopping centers. These air-conditioning systems generally consist of chilled water systems, commonly known as "chillers," which serve as the core equipment for producing cooling and distributing it through piping systems and coils to different zones within the building. Chillers are available in various capacities depending on the usable area of the building, typically ranging from 15–25 refrigeration tons to more than 1,000 refrigeration tons in large buildings or areas requiring precise temperature control 24 hours a day.

In the context of Thailand, a country with a hot and humid climate throughout the year, air-conditioning systems are used frequently and intensively. This is especially true during the summer season, when outdoor temperatures exceed 35°C, causing chiller systems to operate continuously for long periods and resulting in high electricity consumption. According to data from the Electricity Generating Authority of Thailand (EGAT) [1], air-conditioning systems account for approximately 40–65% of the total energy consumption in commercial buildings [2]. Among these systems, chillers are considered the highest energy-consuming equipment within the HVAC (Heating, Ventilation, and Air Conditioning) system.

In general, chillers have a service life of approximately 15–25 years, depending on several factors such as equipment quality, regular maintenance, the environment within the machine room, and operating conditions. If chillers are operated continuously without efficiency improvements or proper maintenance, their performance gradually deteriorates. As a result, the equipment requires more electrical energy to produce the same amount of cooling. This leads to a noticeable reduction in energy efficiency, expressed in terms of the Energy Efficiency Ratio (EER) or Coefficient of Performance (COP), which subsequently increases electricity costs and affects the overall energy management of the building.

Since chillers are large pieces of equipment with piping and control systems integrated into the building, replacement or removal is difficult and costly. Therefore, improving or enhancing the efficiency of the existing system by installing additional equipment, such as a Variable Frequency Drive (VFD), has become a popular approach with strong potential to effectively reduce energy consumption without the need to replace the entire chiller system.

A VFD, or variable frequency drive, plays an important role in controlling the speed of electric motors so that equipment operation corresponds to the actual cooling load. In other words, during periods when the building cooling load decreases, such as at night or on weekends, a chiller equipped with a VFD can reduce the compressor speed as required. This can significantly reduce overall energy consumption. Research conducted by ASHRAE and several field studies in both international and Thai contexts have found that VFD installation can reduce electricity consumption in chiller systems by as much as 15–35%, depending on the load characteristics and control strategy [3].

Although VFD technology is widely recognized for its ability to clearly improve the energy efficiency of chiller systems, the evaluation of energy savings from VFD installation should not be based solely on estimates or theoretical data. This is because the actual savings may vary depending on the building's operating characteristics, cooling load, operating hours, environmental conditions, and system control strategy. Therefore, Measurement and Verification (M&V) is an important process for confirming whether VFD installation can actually reduce energy consumption according to the intended target.

This research therefore focuses on studying the impacts of installing a VFD on a water-cooled chiller under actual operating conditions in a commercial building. Emphasis is placed on data collection, comparison of energy consumption before and after installation, and analysis of actual energy savings based on the Measurement and Verification (M&V) approach. The study aims to evaluate energy performance, cost savings, return on investment, and environmental impacts in terms of reducing greenhouse gas emissions, particularly carbon dioxide (CO_2).

For these reasons, this study is important from both academic and practical perspectives. It not only demonstrates the potential of using VFD technology to improve chiller system efficiency, but also emphasizes the importance of measurement and verification of actual energy savings. The results can be used by building owners, engineers, and system designers as supporting information for making accurate, appropriate, and cost-effective decisions regarding long-term improvements to air-conditioning systems.

2. Materials and Methods

This study aims to evaluate the energy-saving potential and economic feasibility of installing a Variable Frequency Drive (VFD) in a water-cooled chiller air-conditioning system.

The evaluation of this study covers three main aspects as follows:

-Energy consumption and system performance

-Economic feasibility and investment worthiness

-Environmental impact from the reduction of greenhouse gas emissions

The study analyzes the impact of VFD installation on electrical energy consumption, the operating performance of the air-conditioning system, as well as the economic returns and environmental benefits.

The economic feasibility assessment considers key indicators, including the Payback Period, Return on Investment (ROI), and the total energy cost savings achieved throughout the installation period of the equipment. Meanwhile, the environmental assessment converts the amount of electrical energy saved into the reduction of carbon dioxide equivalent emissions (tCO_2e), based on the Emission Factor announced by the Department of Alternative Energy Development and Efficiency.

2.1 Data Collection

In this study, one water-cooled chiller installed in a high-rise building was selected as the case study. The chiller is a main component of the air-conditioning system and represents a significant proportion of the building’s electrical energy consumption.

The chiller selected for this study is a Carrier 19XR [4]water-cooled chiller with a cooling capacity of 500 refrigeration tons. It is equipped with a centrifugal compressor, which is suitable for large-scale air-conditioning systems. The technical data and important operating parameters of the chiller were used to analyze energy consumption and evaluate the effect of installing a Variable Frequency Drive (VFD).

Actual energy consumption data of the chiller system within the building were collected retrospectively over a period of one year.

The collected data included electrical energy consumption, operating hours, and system load levels during different operating periods. These data were used to analyze the energy consumption characteristics and load profile of the system on both a daily and monthly basis.

In this study, the operating data of the chiller were collected through the Chiller Plant Management System (CPMS). The data used for the analysis included the operating load profile of the chiller, date and operating time, electrical energy consumption (kWh), and electrical current. These data were recorded from the actual daily operation of the chiller.

The data used in this study represent the actual operating behavior of the chiller, obtained from the CPMS program. The collected data were organized in tabular form for use in analyzing the energy consumption of the system.

Therefore, the data presented in the following table were used as the basis for analyzing energy consumption, comparing the operating behavior of the chiller, and evaluating the energy performance of the cooling system. This ensures that the analysis results are consistent with the actual operating conditions of the building.

2.2 Analysis of Electrical Energy Consumption Data

After collecting the operating data of the water-cooled chiller, the electrical energy consumption data were studied and analyzed to understand the energy consumption behavior of the system during different operating periods. The analysis considered actual electrical energy consumption, operating hours, and the operating characteristics of the chiller. The collected data were organized in the form of tables and graphs in order to compare energy consumption trends on both a daily and monthly basis. This analysis provides an overview of energy consumption before the installation of the VFD and serves as fundamental data for evaluating energy savings in the subsequent stage.

2.3 Analysis of the Chiller Load Profile

The analysis of the chiller load profile was conducted to study the operating characteristics of the chiller during different time periods. This was carried out by considering the actual load level or percentage of chiller operation. The load data were categorized to determine the proportion of operation under low-load, medium-load, and high-load conditions. This analysis is important because the benefits of VFD installation are more clearly observed when the chiller operates under part-load conditions. Therefore, the study of the load profile enables an appropriate evaluation of the energy-saving potential of the chiller in accordance with the actual operating conditions of the building.

2.4 Analysis of the Coefficient of Performance (COP) of the Chiller

The analysis of the Coefficient of Performance (COP) of the chiller was conducted to evaluate the operating efficiency of the water-cooled chiller. The COP was determined by considering the relationship between the cooling capacity produced and the electrical energy consumed during operation. A higher COP indicates better operating efficiency, as the chiller is able to produce more cooling output relative to the amount of electrical energy consumed. In this study, the load profile and electrical energy consumption data were used to analyze the performance trend of the chiller before and after the installation of the VFD. The results of the COP analysis help demonstrate the impact of VFD installation on the overall efficiency of the air-conditioning system.

2.5 Economic Feasibility Assessment and Economic Analysis

The economic feasibility assessment was conducted by comparing the electrical energy costs before and after the installation of the Variable Speed Drive (VSD) in order to evaluate the value of energy savings generated over a one-year period. The annual energy savings were then used to calculate the payback period and the return on investment.

The assessment of energy savings after VFD installation in this study was based on the reduction in electrical power consumption of the water-cooled chiller according to its operating load level. This is because the VFD is capable of controlling the motor speed to suit the load demand during each operating period, particularly under part-load conditions. Therefore, the analysis compared the actual electrical energy consumption before installation with the estimated electrical energy consumption after VFD installation under the same operating conditions.

2.5.1 Analysis of Return on Investment and Payback Period

The economic feasibility analysis of VFD installation was carried out by considering the investment cost required for the installation and the value of electricity cost savings obtained after the VFD was installed. This analysis aimed to evaluate whether the investment was appropriate and to determine the period required for the project to recover its initial investment.

The data used in the analysis consisted of the VFD installation cost, electricity cost before VFD installation, electricity cost after VFD installation, and annual electricity cost savings. These data were then used to calculate the return on investment and the payback period, which served as key indicators for evaluating the economic feasibility of the project.

The objective of this analysis was to evaluate the number of years required for the investment cost of the VFD installation to be recovered through the reduction in electrical energy costs, as well as to determine the percentage return on investment. The calculations were performed using the equations presented in Equations 1 and 2.

$$Payback\ Period = \frac{Investment\ Cost}{Annual\ Saving} \tag{1}$$

$$\mathrm{ROI} = \frac{\text{Annual Saving}}{\text{Investment Cost}} \times 100 \tag{2}$$

2.6 Environmental Assessment from the Reduction of Greenhouse Gas Emissions

The environmental assessment was conducted by comparing the electrical energy consumption before and after the installation of the VFD over a one-year period. The amount of electrical energy saved was then multiplied by the greenhouse gas emission factor associated with electricity consumption, or the Emission Factor of the power system. The reference value was obtained from the Thailand Greenhouse Gas Management Organization or other relevant sources used for carbon footprint assessment in Thailand.

3. Results and Discussion

The analysis of the effects of installing a Variable Frequency Drive (VFD) in a water-cooled chiller was conducted based on the operating data of the chiller system recorded through the Chiller Plant Management System (CPMS). The analysis focused on comparing the operating behavior of the chiller before and after the installation of the VFD in terms of operating load, electrical current, electrical energy consumption, economic feasibility, and environmental impact from the reduction of greenhouse gas emissions. The results and discussion are presented in the following sections.

3.1 Analysis of the Chiller Load after VFD Installation

Based on the analysis of the chiller load data, it was found that the chiller did not operate at full-load conditions at all times. Instead, the operating load varied according to the cooling demand of the building during different periods. In particular, during periods when the cooling demand of the building decreased, the chiller operated under part-load conditions rather than full-load conditions.

After the installation of the VFD, the system was able to adjust the motor speed more appropriately according to the actual load demand of the chiller. When the load decreased, the motor speed was reduced in accordance with the system demand. As a result, the operation of the chiller became more flexible, and unnecessary motor operation was reduced.

These results indicate that the VFD plays an important role in improving the control of chiller operation, particularly under part-load conditions. This is the operating range in which the system has greater potential to reduce energy consumption compared with constant-speed operation.

3.2 Analysis of the Electrical Current of the Chiller

Electrical current is an important parameter that reflects the operating load of the compressor motor in the chiller. Based on the comparison before and after the installation of the VFD, it was found that the electrical current after VFD installation tended to decrease in relation to the chiller load, especially when the chiller operated under part-load conditions.

Before the installation of the VFD, the motor tended to consume a relatively high level of electrical current because the motor speed could not be appropriately reduced in response to changes in load demand. After the VFD was installed, however, the system was able to control the motor speed in accordance with the actual load demand, resulting in a reduction in the electrical current required for operation.

The reduction in electrical current after VFD installation indicates that the operating load of the motor decreased, which also contributed to a reduction in the overall electrical energy consumption of the system. In addition, this may help reduce both electrical and mechanical stress on the equipment, which is beneficial for long-term operation.

3.3 Analysis of Electrical Energy Consumption after VFD Installation

Based on the analysis of the electrical energy consumption behavior of the chiller, it was found that energy consumption after VFD installation tended to decrease compared with the condition before installation, under similar building operating conditions. The reduction in electrical energy consumption resulted from the ability of the VFD to adjust the motor speed according to the actual load demand.

During periods when the building load decreased, the chiller no longer needed to consume electrical power at a high level as before. Consequently, the electrical energy consumption also decreased. This finding indicates that VFD installation can effectively reduce the energy consumption of the chiller, particularly in air-conditioning systems where the load varies continuously throughout the operating period.

The results of this study therefore support the application of VFD as an appropriate energy conservation measure for chillers in large buildings, as it can reduce energy consumption without negatively affecting the overall cooling production of the system.

3.4 Analysis of Chiller Performance

The performance analysis of the chiller was considered based on the relationship among operating load, electrical energy consumption, and the cooling production capability of the system. After the installation of the VFD, the chiller tended to operate more consistently with the actual load demand, as the system was able to adjust the motor speed according to the cooling demand of the building.

When the chiller was able to reduce electrical energy consumption during periods of lower load, the overall operating efficiency of the system tended to improve. This was particularly evident under part-load conditions, where VFD control is more suitable than conventional control methods.

However, the performance of the chiller may also be affected by other factors, such as chilled water supply temperature, condenser water temperature, outdoor weather conditions, operating hours, and the condition of auxiliary system components. Therefore, the performance evaluation of the system should consider actual operating data together with energy consumption data in order to ensure that the analysis accurately reflects the real operating conditions.

3.5 Economic Analysis

The economic analysis of VFD installation was conducted by comparing the electrical energy costs before and after installation. The results indicated that the reduction in electrical energy consumption after the installation of the VFD led to a corresponding tendency for the energy cost of the chiller to decrease.

The electricity cost savings obtained from the reduction in energy consumption can be used to evaluate the feasibility of the project in terms of payback period and return on investment. If the annual electricity cost savings are high compared with the investment cost, the project will have a shorter payback period and become more attractive from an economic perspective.

Based on the trend of the analysis, it can be explained that VFD installation has the potential to reduce the long-term energy cost of the building, particularly for buildings where the air-conditioning system operates continuously and the load varies over time. After the project reaches its payback point, the electricity cost savings generated will become a net return that helps reduce the building’s operating expenses.

3.6 Environmental Assessment from the Reduction of Greenhouse Gas Emissions

The reduction in electrical energy consumption after VFD installation has a direct effect on reducing greenhouse gas emissions associated with electricity generation. This is because the amount of electricity saved can be converted into the reduction of carbon dioxide equivalent emissions by referring to the greenhouse gas emission factor of the electricity system.

Therefore, VFD installation provides benefits not only in terms of reducing energy costs but also in reducing the environmental impact of the building. This is particularly significant for large buildings where the air-conditioning system accounts for a major proportion of total energy consumption. Reducing the energy consumption of the chiller is therefore an important measure that supports the reduction of greenhouse gas emissions at the organizational level.

In addition, the reduction of greenhouse gas emissions resulting from VFD installation can be used as supporting information for energy management, organizational carbon footprint assessment, and the development of long-term sustainability strategies for buildings.

3.7 Overall Discussion

Based on the overall analysis, it can be concluded that the installation of a VFD in a water-cooled chiller enables the system to operate more appropriately according to the actual load demand of the building. This is particularly beneficial under part-load conditions, where the chiller does not need to operate at full capacity at all times.

After VFD installation, the electrical current and electrical energy consumption tended to decrease because the motor speed could be adjusted according to the system demand. As a result, the chiller operated more efficiently and unnecessary energy consumption was reduced.

From an economic perspective, the reduction in electrical energy consumption helps decrease the building's operating costs. The resulting cost savings can be used to evaluate the investment feasibility through indicators such as payback period and return on investment. From an environmental perspective, the reduction in electricity consumption helps reduce greenhouse gas emissions from the electricity system. These findings indicate that VFD installation provides benefits in terms of energy performance, economic feasibility, and environmental impact.

Therefore, VFD installation in a chiller is an appropriate approach for improving the efficiency of air-conditioning systems in large buildings, particularly buildings where chillers operate continuously and the cooling load varies over time. However, further quantitative analysis should be conducted once complete numerical data are available in order to clearly confirm the energy savings, economic returns, and environmental benefits.

4. Conclusions

Based on the study of the installation of a Variable Frequency Drive (VFD) in a water-cooled chiller, it was found that the VFD contributes to improving the chiller operation by enabling the system to respond more appropriately to the actual load demand of the building, particularly under part-load conditions. As a result, the electrical current and electrical energy consumption tended to decrease compared with the condition before installation. In addition, the reduction in electrical energy consumption also led to a decrease in the building's energy costs, which can be further used to evaluate the economic feasibility of the project through the payback period and return on investment. From an environmental perspective, the reduction in electrical energy consumption also contributes to lower greenhouse gas emissions associated with electricity use, thereby supporting energy management and long-term building sustainability. Therefore, VFD installation is considered an appropriate approach for improving the efficiency of air-conditioning systems in large buildings in terms of energy performance, economic feasibility, and environmental impact.

5. Acknowledgements

The authors would like to express their sincere gratitude to the College of Interdisciplinary and Integrative Studies and the Energy Research Institute, Chulalongkorn University, for providing academic facilities, resources, and technical support.

The author would also like to express sincere appreciation to the academic advisor, Assoc. Prof. Dr. Sirima Panyametheekul, for her guidance, continuous encouragement, and invaluable technical assistance throughout the development of this research.

References

[1] Komchadluek. *The Truth from MEA: Test Results Reveal That the Hotter the Weather, the More Electricity Air Conditioners Consume*, 2021, https://www.komchadluek.net/pr/462671.
[2] Department of Alternative Energy Development and Efficiency. *Guidelines for Energy Conservation Building Design* , 2017, Energy Conservation Building Design Coordination Center.
[3] Ashrae Journal. *VFDs for large chillers*, 2010, https://www.researchgate.net/publication/283253645_VFDs_for_large_chillers
[4] Carrier Corporation.(n.d.). AquaEdge 19XR/XRV Centrifugal Liquid Chiller: Product Data, Carrier Corporation.
[5] Thailand Greenhouse Gas Management Organization. (n.d.). Emission Factor for Carbon Footprint for Organization, Thailand Greenhouse Gas Management Organization.
[6] ASHRAE . ASHRAE Guideline 14: Measurement of Energy, Demand, and Water Savings. 2014, American Society of Heating, Refrigerating and Air-Conditioning Engineers.
[7] Efficiency Valuation Organization.International Performance Measurement and Verification Protocol: Core Concepts, 2022, Efficiency Valuation Organization.
[8] Department of Alternative Energy Development and Efficiency, Ministry of Energy. Training Manual on the Assessment of Energy Conservation Potential, Chapter 6: Central Air-Conditioning Systems. http://energyauditorthai.com/download/

IV. Sustainable Materials and Green Manufacturing

Injection-Based Self-Healing Repair Using *Bacillus sp.* for Impact-Damaged High-Strength Reinforced Concrete Slabs

Arivandi[1], Teuku Budi Aulia[2,*], Rijalul Fikri[2]

[1] Student Master of Civil Engineering Department, Faculty of Engineering, Universitas Syiah Kuala, Aceh, Indonesia
[2] Department of Civil Engineering, Faculty of Engineering, Universitas Syiah Kuala, Banda Aceh, Indonesia
* Correspondence: aulia@usk.ac.id

Abstract

High-strength reinforced concrete slabs may suffer progressive cracking and localized failure under repeated impact loading, making repair strategies important for resilient and sustainable infrastructure. This study evaluates *Bacillus sp.* as an injection-based self-healing agent for repairing 85 MPa reinforced concrete slabs previously damaged by impact. Reinforced square slabs with dimensions of 40 x 40 x 4 cm, 60 x 60 x 6 cm, and 80 x 80 x 8 cm were prepared using a high-strength concrete mixture containing cement, silica fume, superplasticizer, fine aggregate, coarse aggregate, and water. *Bacillus sp.* was applied at 0.6% of cement weight with urea, CaCl2, and nutrient broth, and injected into cracks after initial damage at approximately 70% of ultimate impact capacity. The specimens were immersed for 28 days and then retested under repeated drop-weight impact loading using a 3 kg steel ball dropped from 1 m. The control P8-N slab failed at 1003 blows with absorbed energy of 29,518.29 J, while the injected P8-I specimen reached 1239 blows and 36,463.77 J in the cumulative comparison. Relative cumulative impact-capacity ratios after the injection sequence were 123.53%, 151.80%, and 137.50% for P8-I, P6-I, and P4-I, respectively. The P6 and P4 benchmarks were taken from comparable previous data, while the P8 comparison used the tested P8-N control. The results indicate that *Bacillus sp.* injection contributed to residual-capacity restoration, but the response should not be interpreted as full recovery to an undamaged state. The findings extend Bacillus-based self-healing research from mainly static crack closure to impact-damaged high-strength slab repair; however, the evidence remains limited by single dosage, limited replication, and the absence of direct microstructural confirmation of $CaCO_3$.

Keywords: *Bacillus sp.*; self-healing concrete; high-strength concrete; impact loading; crack injection

1. Introduction

Impact loading is a critical dynamic action for reinforced concrete components because the applied energy is transferred within a very short duration and can produce localized crushing, flexural cracking, radial cracking, and eventual punching-type failure. For transport, port, industrial, and bridge facilities, repeated accidental impacts may not immediately collapse a member, but they can reduce stiffness and accelerate crack propagation, which underscores the need for reliable post-damage assessment and repair. Dynamic response under such loads is commonly interpreted through energy absorption, deformation, and damage progression rather than through static strength alone [1]. Conventional crack repair generally relies on external resin, grout, or replacement. These approaches may restore serviceability, but they also require access, labor, inspection cycles, and materials that may not be optimal for long-term sustainability. Microbially induced calcium carbonate precipitation has therefore attracted attention as a biological repair mechanism. In this approach, bacteria support the formation of calcium carbonate deposits that can fill cracks and pores, reduce permeability, and improve durability-related performance [2,3]. Recent reviews also position bacterial concrete as a strategy that can contribute to lower maintenance demand and potentially improve the environmental profile of concrete infrastructure over its service life [4].

The mechanism depends strongly on bacterial activity, nutrient availability, calcium source, moisture, and the ability of the organism to remain viable in the alkaline concrete environment. Ureolytic bacteria can hydrolyze urea, increase local alkalinity, and promote carbonate formation; calcium ions then react with carbonate ions to form calcium carbonate deposits [5,6]. Bacillus species are frequently selected because spores can survive harsh alkaline conditions and re-activate when moisture and nutrients become available. Previous studies have reported the use of Bacillus-based systems for crack healing and strength recovery in cementitious materials [7-9].

Despite this growing body of work, fewer experimental data are available for injection-based biological repair of high-strength reinforced concrete slabs after repeated impact damage. This gap matters because a repair material that performs well in static cracks may not necessarily improve a member whose cracking and deformation were produced by dynamic impact. The present paper condenses a master thesis experimental program into a proceeding manuscript for the International Conference 2026 theme on sustainable science and engineering. The objective is to evaluate the capacity of *Bacillus sp.* injection to restore residual impact resistance, reduce crack propagation, and improve cumulative absorbed energy of high-strength reinforced concrete slabs with a nominal compressive strength of 85 MPa.

2. Materials and Methods

2.1. Materials and concrete mixture

The experimental program used Portland Composite Cement, fine aggregate, coarse aggregate, water, silica fume, and a superplasticizer. The coarse aggregate was crushed stone with a 2.38-4.76 mm particle size range, while the fine aggregate was sand with a 0-2.38 mm range. Silica fume was incorporated to improve microstructure density and high-strength performance, while superplasticizer was used to maintain workability at a low water-to-cement ratio. The concrete was designed for a target compressive strength of 85 MPa and used a water-to-cement ratio of 0.20.
The mix proportion for 1 m3 of concrete is presented in Table 1. This proportion was adopted from the thesis trial mix and is reported here to make the experimental procedure reproducible and to allow comparison with future studies.

Table 1. Mix proportion of high-strength concrete for 1 m3.

Material	Quantity	Unit
Cement	550.00	kg
Crushed stone, 2.38-4.76 mm	300.00	kg
Sand, 0-2.38 mm	1150.00	kg
Water	110.00	kg
Superplasticizer (Viscocrete-1003)	16.50	kg
Silica fume	44.00	kg

2.2. *Bacillus sp.* isolation and injection medium

Bacillus sp. was isolated from soil collected at the Gampong Jawa final disposal site in Banda Aceh and developed at the Microbiology Laboratory, Faculty of Mathematics and Natural Sciences, Universitas Syiah Kuala. Soil samples were collected aseptically, serially diluted in sterile NaCl solution, cultured on nutrient agar, purified using quadrant streaking, and stored on slant agar at 4 degrees C before use. Morphological and physiological characterization indicated consistency with the Bacillus genus.

The bacterial injection medium contained *Bacillus sp.* at 0.6% of cement weight, combined with urea, $CaCl_2$, and nutrient broth. The injection proportions are shown in Table 2. Urea and nutrient broth were provided as metabolic and nutrient sources, while $CaCl_2$ was supplied as the calcium source for calcium carbonate precipitation. The total additional bacterial system corresponded to 1.53% of cement weight.

Table 2. Composition of Bacillus sp. injection medium.

Component	Dosage by cement weight (%)	Function
Bacillus sp.	0.60	Biological self-healing agent
Nutrient broth	0.13	Nutrient source
Urea	0.53	Carbonate-generating substrate
$CaCl_2$	0.27	Calcium source

2.3. Specimen preparation and repair protocol

The test specimens were reinforced square slabs with three dimensions: 40 x 40 x 4 cm, 60 x 60 x 6 cm, and 80 x 80 x 8 cm. Reinforcement was prepared using P8 steel bars arranged in a square grid, with a concrete cover of 25 mm. The specimen code P8-N denotes the 80 x 80 x 8 cm normal slab without injection, while P8-I, P6-I, and P4-I denote injected slabs with thicknesses of 8 cm, 6 cm, and 4 cm, respectively.

Fresh concrete was placed in plywood molds and compacted. After demolding at 24 hours, slab specimens were cured for 28 days. For injected specimens, the first impact stage was conducted until the slab reached approximately 70% of its ultimate impact damage condition. The cracks were then marked and injected using a syringe so that the bacterial suspension could penetrate the crack paths. After injection, the slabs were immersed in water for 28 days to activate the biological repair process before the second impact test was conducted to failure.

2.4. Impact and compressive strength testing

The impact test was adapted from ASTM D2794-93 [10]. Each slab was placed on supports, and a 3 kg steel ball was repeatedly dropped from a height of 1 m onto the top surface of the slab. The number of blows was recorded at initial cracking and at failure. Failure was defined visually when crack propagation and concrete damage progressed to a critical state, including exposed reinforcement or severe local damage. Impact energy absorption was computed using Equation (1), where Ep is the absorbed potential energy, m is the impact mass, g is gravitational acceleration, h is drop height, and n is the number of blows.

$$Ep = m \times g \times h \times n, \quad (1)$$

With m = 3 kg, g = 9.81 m/s^2, and h = 1 m, each blow corresponded to approximately 29.43 J. Additional observations included impact indentation depth, crack pattern development, concrete strain, and steel strain from the data logger. Compressive strength was tested using 150 x 300 mm cylinders at 28 days according to the standard cylinder test principle [11].

2.5. Data analysis

The analysis focused on three response levels. First, the normal P8-N slab was used as the reference capacity for un-repaired high-strength reinforced concrete under repeated impact. Second, the injected slabs were evaluated before repair at approximately 70% damage to identify residual cracking conditions. Third, post-injection performance was assessed after 28 days of immersion. All impact energies were revalidated against the thesis tables and the energy equation Ep = m x g x h x n, where one blow corresponds to 29.43 J. Recovery was interpreted from the additional impact capacity after injection, the ratio between the final reported injected capacity and the normal reference capacity, and the observed changes in crack propagation. The interpretation emphasizes residual structural capacity; it does not assume complete restoration of the original undamaged slab.

3. Results and Discussion

3.1. Physical properties and compressive strength

The aggregate properties satisfied the acceptance ranges used in the thesis program. The coarse aggregate had a bulk density of 1.458 kg/L, SSD specific gravity of 2.680, oven-dry specific gravity of 2.665, absorption of 1.024%, and fineness modulus of 5.000. The fine aggregate had a bulk density of 1.549 kg/L, SSD specific gravity of 2.589, oven-dry specific gravity of 2.549, absorption of 1.593%, and fineness modulus of 2.091. These values indicate that the aggregates were suitable for high-strength concrete production.

The 28-day compressive strength results are summarized in Table 3. The average strength reached 88.17 MPa, exceeding the target strength of 85 MPa. The small difference among the three cylinders indicates acceptable uniformity in the mixture and curing process.

Table 3. Compressive strength of high-strength concrete cylinders at 28 days.

Specimen	Compressive strength (MPa)
BMT-1	89.0
BMT-2	87.0
BMT-3	88.5

3.2. Impact behavior of the normal slab and pre-injection damage

The normal slab P8-N was tested without bacterial injection to establish the reference impact capacity. As shown in Table 4, the first visible crack occurred at 543 blows, equivalent to 15,980.49 J of absorbed energy, with an indentation depth of 0.13 cm. Failure occurred at 1003 blows, equivalent to 29,518.29 J, with a final indentation depth of 2.40 cm. The increase in energy was accompanied by greater crack propagation and local damage around the impact point.

Table 4. Impact response of normal slab without injection.

Specimen	Blows at initial crack	Blows at failure	Energy at initial crack (J)	Energy at failure (J)	Indentation at initial crack (cm)	Indentation at failure (cm)
P8-N	543	1003	15,980.49	29,518.29	0.13	2.40

For the injected series, the first impact stage was stopped at the predefined 70% damage condition before the crack injection treatment. Table 5 shows that the 8 cm slab P8-I had the highest pre-injection resistance, reaching 702 blows and 20,659.86 J at 70% damage. P6-I reached 311 blows and 9,152.73 J, while P4-I reached only 29 blows and 853.47 J. The sharp decline from P8-I to P4-I confirms that cross-sectional thickness and plan dimensions strongly governed resistance to repeated impact. Visual observations from the thesis drawings showed that impact damage began near the drop point and developed as flexural, radial, and branched cracks. P8-I distributed cracks more widely, while the thinner P6-I and P4-I specimens developed more localized and concentrated damage around the impact zone. The strain responses of concrete and reinforcement increased with the number of blows, showing progressive deformation until damage accumulation became critical.

Table 5. Pre-injection impact response at initial crack and 70% damage.

Specimen	Blows at initial crack	Blows at 70% damage	Energy at initial crack (J)	Energy at 70% damage (J)	Indentation at initial crack (cm)	Indentation at 70% damage (cm)
P8-I	537	702	15,806.91	20,659.86	0.11	1.90
P6-I	182	311	5,356.26	9,152.73	0.19	1.70
P4-I	17	29	500.31	853.47	0.24	1.40

This result is a strength and a boundary condition of the experiment. The data clearly show the sensitivity of impact resistance to slab geometry, but they also mean that P8-I, P6-I, and P4-I cannot be compared as if thickness were the only changing factor. Plan dimension, thickness, crack length, crack connectivity, and local crushing changed simultaneously. Therefore, the injected-series comparison is best used to identify trends in repair response rather than to establish a general design coefficient for *Bacillus sp.* injection.

3.3. Post-injection impact response

After pre-damage, bacterial injection, and 28 days of immersion, the slabs were retested under repeated impact. Table 6 presents the impact response after injection. P8-I again gave the strongest response among the repaired specimens, failing at 537 post-injection blows and 15,806.91 J. P6-I failed at 26 blows and 765.18 J, while P4-I failed at 4 blows and 117.72 J. The post-injection resistance was therefore highly dependent on slab thickness, pre-existing damage severity, and the ability of the bacterial suspension to reach the active crack network.

The post-injection crack maps in the thesis indicated that new cracks tended to follow or branch from the previously injected crack paths. This suggests that injection did not erase the structural memory of the first impact stage. The more reasonable interpretation is that *Bacillus sp.* precipitates helped fill part of the crack volume, slowed crack reopening, and allowed additional energy absorption, but did not create a brand-new undamaged slab. Thus, the post-repair response should be interpreted as residual capacity, not as full restoration to an undamaged state.

Table 6. Impact response of slabs after *Bacillus sp.* injection.

Specimen	Blows at new crack	Blows at failure	Energy at new crack (J)	Energy at failure (J)	Indentation at new crack (cm)	Indentation at failure (cm)
P8-I	323	537	9,505.89	15,806.91	0.16	2.30
P6-I	10	26	294.30	765.18	0.14	1.60
P4-I	1	4	29.43	117.72	0.19	1.30

Figure 1 presents the relative impact-capacity comparison before and after *Bacillus sp.* injection. In the cumulative comparison, P8-I reached 123.53% of P8-N, whereas P6-I and P4-I reached 151.80% and 137.50% of the non-injected P6-N and P4-N benchmarks from previous comparable research, respectively. These ratios should be read together with the absolute post-injection energy values in Table 6: P8-I still had the highest absolute post-injection capacity (15,806.91 J), while P6-I and P4-I remained much lower at 765.18 J and 117.72 J. Therefore, the percentage comparison indicates repair potential, but the structural interpretation remains governed by slab geometry, damage condition, and benchmark source.

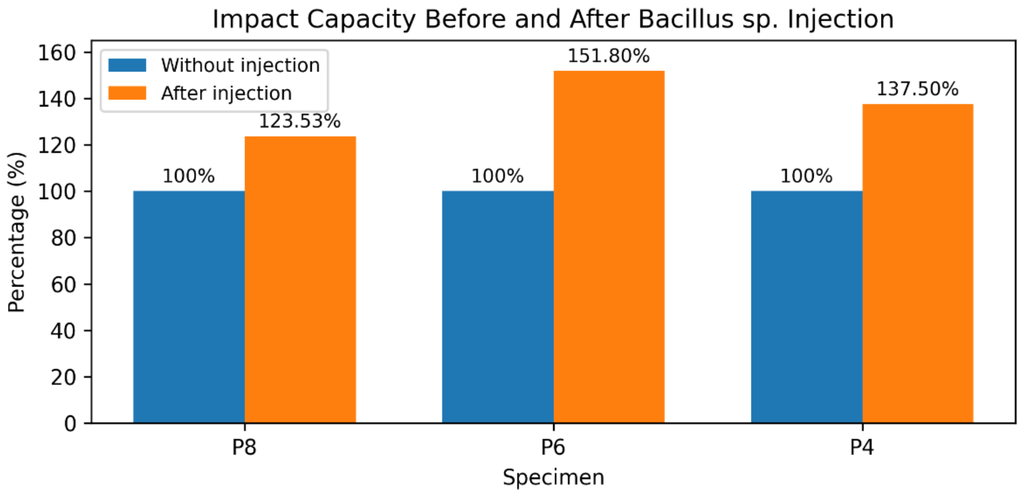

Figure 1. Relative impact capacity of slabs before and after *Bacillus sp.* injection.

3.4. Cumulative capacity, significance, and alternative interpretations

A more direct measure of structural relevance is the final reported capacity after initial damage and repair. Table 7 compares the normal P8-N reference slab with the injected P8-I slab using the cumulative comparison table. P8-N failed at 1003 blows and 29,518.29 J. In contrast, P8-I reached 1239 blows and 36,463.77 J after the injection sequence. This corresponds to 123.53% of the normal P8-N capacity, as illustrated in Figure 1. The comparison is useful because both specimens had the same 80 x 80 x 8 cm slab geometry; however, it should be interpreted as a repaired-member response under the test sequence, not as proof that the biological treatment makes an originally undamaged slab stronger than the control.

Table 7. Cumulative comparison between normal P8-N and injected P8-I slabs.

Specimen	**Blows at initial crack**	**Blows at failure**	**Energy at initial crack (J)**	**Energy at failure (J)**	**Indentation at initial crack (cm)**	**Indentation at failure (cm)**
P8-N	543	1003	15,980.49	29,518.29	0.13	2.40
P8-I	537	1239	15,806.91	36,463.77	0.11	2.30

The result indicates that *Bacillus sp.* injection helped maintain residual integrity after a substantial pre-damage stage. This is significant because most *Bacillus*-based concrete studies emphasize static crack closure, permeability reduction, or strength recovery in cementitious materials, whereas the present study evaluates a reinforced high-strength slab that had already accumulated dynamic impact damage. From a sustainability perspective, a repair method that extends service life can reduce replacement material demand and maintenance interventions. The implication fits the broader direction of bacterial concrete research, where biological mineral formation is investigated as a route to improve durability and reduce repair frequency [12,13].

Alternative explanations should also be considered. The higher P8-I final capacity may reflect not only $CaCO_3$ precipitation, but also aggregate interlock, reinforcement bridging, residual friction along closed crack faces, moisture-induced crack closure during immersion, and the relatively favorable 8 cm slab thickness. The absence of direct SEM, XRD, permeability, or crack-width recovery measurements means that the biological mechanism is supported indirectly by performance recovery and by established *Bacillus*-based precipitation theory, not directly proven at the microstructural level in this specimen set.

3.5. Mechanistic interpretation, limitations, and field relevance

The most plausible mechanism behind the observed capacity improvement is calcium carbonate precipitation inside cracks. The injected *Bacillus sp.* and nutrient medium entered the crack network, and the 28-day immersion supplied moisture for bacterial activity. Urea hydrolysis and calcium availability promoted $CaCO_3$ formation, which may partially fill crack voids and reduce the ease of crack reopening during the second impact stage. However, the repair effect was not uniform among all slab sizes. This confirms that biological crack filling is governed not only by bacterial dosage, but also by crack width, crack connectivity, local crushing, water access, and the remaining structural capacity of the slab.

Several limitations should be recognized. First, the study used one bacterial dosage, so the optimum concentration cannot be claimed. Second, the number of slabs in each configuration was limited, making the results more suitable as experimental evidence than as a full statistical design basis. Third, the study inferred $CaCO_3$ formation from performance improvement and established mechanism rather than direct microstructural confirmation. Fourth, the impact method was adapted for repeated drop-weight response, while the original ASTM D2794 framework was developed for impact deformation of coatings; therefore, the test is suitable for comparative laboratory evidence but should not be generalized directly to all structural impact scenarios. Fifth, long-term durability after repair, repeated wet-dry cycles, permeability recovery, and chloride ingress resistance were not evaluated.

For field application, the method is most defensible as a complementary repair technique for crack networks that remain accessible to injection and moisture curing. It is less suitable as a stand-alone solution when the member has severe local crushing, exposed reinforcement, section loss, or unstable crack widening. Future work should include more replicate specimens, multiple bacterial dosages, direct crack-width measurement, permeability testing, SEM or XRD verification of $CaCO_3$ deposits, additional dynamic or cyclic loading methods, and longer healing-time evaluation.

4. Conclusions

This paper presents a proceeding-style manuscript derived from experimental thesis data on *Bacillus sp.* injection for impact-damaged high-strength reinforced concrete slabs. The following conclusions are supported by the revalidated test results:

1. The concrete achieved an average 28-day compressive strength of 88.17 MPa, exceeding the target value of 85 MPa and confirming that the mixture represented high-strength concrete.
2. The normal P8-N slab failed at 1003 blows with absorbed energy of 29,518.29 J. Prior to injection, the injected-series specimens showed strong size dependence: P8-I reached 702 blows at 70% damage, whereas P6-I and P4-I reached 311 and 29 blows, respectively.
3. After *Bacillus sp.* injection and 28 days of immersion, the repaired slabs retained additional impact resistance. Relative cumulative impact-capacity ratios were 123.53% for P8-I, 151.80% for P6-I, and 137.50% for P4-I relative to their non-injected benchmarks; P6-N and P4-N benchmarks were obtained from comparable previous data. The absolute post-injection capacities show that geometry and damage condition still controlled the repaired response.
4. The cumulative P8-I capacity reached 1239 blows and 36,463.77 J, equivalent to 123.53% of the normal P8-N reference capacity. This finding indicates that *Bacillus sp.* injection can maintain residual impact resistance in a repaired high-strength slab, but it should not be interpreted as complete restoration of an undamaged member.
5. The main limitations are the single bacterial dosage, limited specimen replication, indirect confirmation of $CaCO_3$ precipitation, and absence of long-term durability tests. Future work should combine wider dosage variation, repeated specimens, crack-width and permeability recovery measurements, microscopic verification, additional dynamic or cyclic loading methods, and longer healing-time/durability tests.

5. Acknowledgements

The author acknowledges the Civil Engineering Construction and Building Materials Laboratory and the Microbiology Laboratory of Universitas Syiah Kuala for supporting the experimental work. The author also thanks the thesis supervisors and laboratory technicians for guidance during specimen preparation, testing, and data collection.

References

[1] Chopra, A. K. Dynamics of Structures: Theory and Applications to Earthquake Engineering, 4th ed.; Prentice Hall: Upper Saddle River, NJ, USA, 2012.

[2] De Muynck, W.; De Belie, N.; Verstraete, W. Microbial Carbonate Precipitation in Construction Materials: A Review. Ecological Engineering 2010, 36, 118-136.

[3] Jonkers, H. M. Self Healing Concrete: A Biological Approach. In Self Healing Materials: An Alternative Approach to 20 Centuries of Materials Science; Springer: Dordrecht, The Netherlands, 2007; pp. 195-204.

[4] Bandyopadhyay, A.; Saha, A.; Ghosh, D.; Dam, B.; Samanta, A. K.; Dutta, S. Microbial Repairing of Concrete and Its Role in CO2 Sequestration: A Critical Review. Beni-Suef University Journal of Basic and Applied Sciences 2023, 12, 1. https://doi.org/10.1186/s43088-023-00344-1.

[5] Hammes, F.; Boon, N.; De Villiers, J.; Verstraete, W.; Siciliano, S. D. Strain-Specific Ureolytic Microbial Calcium Carbonate Precipitation. Applied and Environmental Microbiology 2003, 69, 4901-4909. https://doi.org/10.1128/AEM.69.8.4901-4909.2003.

[6] Achal, V.; Mukherjee, A.; Basu, P. C.; Reddy, M. S. Strain Improvement of Sporosarcina pasteurii for Enhanced Urease and Calcite Production. Journal of Industrial Microbiology & Biotechnology 2009, 36, 981-988. https://doi.org/10.1007/s10295-009-0561-4.

[7] Huynh, N. N. T.; Phuong, N. M.; Toan, N. P. A.; Son, N. K. Bacillus subtilis HU58 Immobilized in Micropores of Diatomite for Using in Self-Healing Concrete. Procedia Engineering 2017, 171. https://doi.org/10.1016/j.proeng.2017.01.385.

[8] Gumelar, F.; Nuraini, R. Bakteri Bacillus subtilis Sebagai Agen Self Healing Concrete dengan Variasi Persentase dan Nilai pH. Jurnal Rekayasa 2021, 10, 2. https://doi.org/10.37037/jrftsp.v10i2.71.

[9] Nindhita, K. W.; Zaki, A.; Zeyad, A. M. Effect of Bacillus subtilis Bacteria on the Mechanical Properties of Corroded Self-Healing Concrete. Frattura ed Integrita Strutturale 2024, 18, 68. https://doi.org/10.3221/IGF-ESIS.68.09.

[10] ASTM International. ASTM D2794-93: Standard Test Method for Resistance of Organic Coatings to the Effects of Rapid Deformation (Impact); ASTM International: West Conshohocken, PA, USA, 1993.

[11] Badan Standardisasi Nasional. SNI 1974: Cara Uji Kuat Tekan Beton dengan Benda Uji Silinder yang Dicetak; BSN: Jakarta, Indonesia, 2011.

[12] Bashaveni, B.; Pannem, R. M. R. Development of Self-Healing Property in Self Compacting Concrete. Case Studies in Construction Materials 2024, 20. https://doi.org/10.1016/j.cscm.2024.e02942.

[13] Rossi, E.; Vermeer, C. M.; Mors, R.; Kleerebezem, R.; Copuroglu, O.; Jonkers, H. M. On the Applicability of a Precursor Derived from Organic Waste Streams for Bacteria-Based Self-Healing Concrete. Frontiers in Built Environment 2021, 7. https://doi.org/10.3389/fbuil.2021.632921.

[14] Arivandi. Penggunaan Bakteri Bacillus sp. untuk Perbaikan Struktur dengan Metode Injeksi pada Plat Beton Bertulang Mutu Tinggi 85 MPa yang Mengalami Gagal Impact. Master Thesis, Universitas Syiah Kuala, Banda Aceh, Indonesia, 2026.

V. Other Related Topics

Greening the Algorithm: A Systematic Review of Artificial Intelligence in Green Marketing

Narubodee Wathanakom[1]*

[1]Sukhothai Thammathirat Open University; narubodee.wat@stou.ac.th
*Correspondence: narubodee.wat@stou.ac.th

Abstract

Artificial intelligence (AI) has rapidly migrated from a back-office automation layer into the front line of green marketing, mediating eco-claims, personalising sustainability appeals, and orchestrating circular-economy operations. The literature remains fragmented across consumer-behaviour, technology, governance, and industry silos. This study synthesises the state of evidence and proposes an integrative framework. A PRISMA 2020 systematic review was conducted on a curated corpus of 178 records identified from peer-reviewed journals and IEEE/Scopus-indexed proceedings published between 2020 and 2026. After duplicate removal and full-text screening for explicit AI and green-marketing focus, 28 studies were included in the qualitative synthesis. Eight overlapping clusters emerged: theoretical frameworks; consumer cognition and intentions; generative-AI persuasion; greenwashing and traceability; industry applications; enterprise decision support; engagement and gamification; and meta-research. The findings are integrated into a four-pillar TIBE framework; Technology stack, Influence pathways, Boundary conditions, and Ethical-environmental guardrails. AI is a powerful but conditional accelerator of green marketing because its credibility now depends on transparent governance, balanced human–AI co-creation, and explicit accounting for AI's own environmental footprint.

Keywords: artificial intelligence; green marketing; systematic review; PRISMA 2020; greenwashing; sustainable consumer behaviour

1. Introduction

The new reality of marketing lies at the intersection of environmental responsibility and machine intelligence in the same brief [1, 2]. Environmental urgency, regulation, and increasing consumer skepticism have made sustainability not only a key message but also a cornerstone of brand legitimacy [1, 2]. At the same time, generative AI, large language models, agent-based models, recommendation algorithms, and convolutional neural networks have moved out of the laboratory and into the daily practice of marketing [3, 4]. Thus, the confluence of these two trends, referred to below as AI-powered green marketing, leads to the rapid growth of a fragmented literature.

While existing literature reviews cover such areas as AI in advertising, sustainability marketing, circular-economy marketing, greenwashing through ESG reporting, and gamification, the terminology remains quite different, and none of the works connect them [1, 2, 3, 5, 6, 7]. Works focusing on consumer behavior use the S-O-R approach, the VAB model, and the ADO logic [8, 9, 10, 11]; studies of advertising rely on the concepts of processing fluency and illusion of control [12, 13]; those concerned with governance provide ESG reporting strategies with the involvement of AI [5, 14]; and engineering papers design decision support systems using neural network and reinforcement learning approaches [4, 15, 16]. The streams do not interact with each other, leaving practitioners and researchers without a clear overview of the topic.

The present study attempts to fill this void. We conducted a systematic review based on the PRISMA guidelines and selected twenty-eight papers discussing AI usage in green marketing published from 2020 to 2026. The paper provides (i) mapping of theories, methodologies, industries, and geographical coverage; (ii) extraction of key mechanisms by which AI influences the success of green marketing activities; (iii) identification of gaps in literature; and (iv) consolidation of results in a four-pillar framework of Technology stack, Influence pathways, Boundary conditions, and Ethical and environmental guardrails (TIBE). Contributions are twofold: an evidence base, cross-cluster synthesis, and a roadmap for further research and practice.

2. Materials and Methods

PRISMA 2020 guidelines have been followed in conducting this systematic review. This includes the following steps of protocol: identification, screening, eligibility, inclusion, data extraction, and qualitative synthesis. As the literature corpus had already been retrieved earlier by searching on Scopus using combined queries with the key terms "artificial intelligence" AND "green marketing"/"sustainable marketing"/"circular marketing"/"greenwashing"), no database search was conducted anew; instead, this retrieved corpus constituted the identification step. The search date was conducted on May 13th, 2026.

2.1 Eligibility criteria

Records were deemed eligible if they (1) comprised peer-reviewed journal articles and conference proceedings indexed on Scopus; (2) were published in the period 2020-2026; (3) concerned the use of artificial intelligence techniques (machine learning, deep learning, large language models, generative AI, agent-based modeling, recommender systems, neural networks, decision support systems) in green, sustainable, eco, circular, or ESG marketing contexts; and (4) offered evidence in the form of empirical research, theory building, systematic reviews, bibliometric studies, and design science. The records were excluded if they did not have sustainability component to their use of AI in marketing context, were non-peer-reviewed publications, or duplicated a record already selected into the review corpus.

2.2 Information sources and screening

178 records were identified from the researcher-curated database (Scopus). After removing 32 duplicates, 146 records were screened on the basis of title and abstract, of which 118 were excluded for not meeting the inclusion criteria. The remaining 28 reports were sought for full-text retrieval, all of which were successfully obtained. All 28 reports were assessed for eligibility, and none was subsequently excluded. A total of 28 studies were included in the qualitative synthesis.

Identification: 178 records identified from researcher-curated databases (Scopus)
↓ Duplicates removed: 32
Screening: 146 records screened on title and abstract | Excluded: 118
↓ Reports sought: 28 | Reports not retrieved: 0
Eligibility: 28 reports assessed for eligibility | Excluded at full-text: 0
↓
Included: 28 studies in the qualitative synthesis

Figure 1. PRISMA 2020 flow diagram for the systematic review.

2.3 Data extraction and synthesis

A systematic template was used to extract the following information from each paper: bibliographic details; AI classification following the typology outlined by Huang and Rust [18] (Mechanical / Thinking / Feeling); theoretical foundations; methodology used; sample/context; sector; geographic location; dependent variable; and main result. Double-coding was undertaken, followed by clustering analysis to identify thematic areas through thematic synthesis. The risk of bias was judged based on qualitative criteria due to the heterogeneity of the literature review corpus (PLS-SEM, fsQCA, NCA, SEM-ANN, experimentation, LDA, bibliometric studies, and conceptual contributions). For each piece of research, the following were used as criteria: sampling size, construct definition, clear inclusion criteria for reviews, and effect sizes reported.

3. Results and Discussion

Table 1 presents an overview of the twenty-eight included studies. The corpus is dominated by 2025 publications (n=18), followed by 2026 (n=8) and one 2024 entry, reflecting the explosive recent growth of the field. PLS-SEM is the most frequent method (n=8), followed by systematic-review/bibliometric (n=7), experimental (n=3), and design-science / prediction-model (n=3). Empirical studies cluster around China (n=6), the UAE (n=2), Egypt, India, Japan, Turkey, Malaysia, Palestine, and Greece. Industries span e-commerce, tourism, cosmetics, second-hand electronics, agri-food, smart homes, and smart cities.

Table 1. Overview of the 28 included studies (ID corresponds to the reference list).

ID	Author(s) Year	Method	Context / Sample	Headline focus
1	Mei et al. 2025	PRISMA SLR (n=47)	AI × 4Ps mapping	AI typology applied to green marketing mix
2	Paiva 2025	PRISMA SLR (n=39)	Circular-economy marketing	Tech-enabled CEM and greenwashing risks
3	Garg et al. 2025	SLR + ADO (n=28)	AI × sustainability perception	Trust/loyalty via ML and personalisation
4	Liu & Li 2025	SLR + quantitative	Enterprise digital marketing	+22.5% conversion, –15% cost
5	Hu et al. 2026	CiteSpace bibliometric	ESG greenwashing 2017–25	English vs Chinese literature divergence
6	Nguyen-Viet & Nguyen 2025	PRISMA + ADO-TCM, n=56	Green gamification	AI ethics underexplored
7	Kumar et al. 2025	LDA, n=2,061	Green marketing 1991–2025	TCM framework for future research
8	Ma et al. 2025	PLS-SEM + fsQCA, n=461	Green AI products	VAB → green purchasing behaviour
9	Imran et al. 2026	PLS-SEM, n=427	Chinese tourists	Eco-social receptivity → e-vocacy
10	Armutcu 2026	SEM-ANN, n=609	Turkish Gen Z	AI efforts → brand → green purchasing
11	Li et al. 2026	PLS-SEM, n=489	Chinese social commerce	AI chatbots → eco-friendly buying intention
12	Wan et al. 2026	Field + 2 experiments	Illusion of control	AI autonomy → WTP via perceived control

ID	Author(s) Year	Method	Context / Sample	Headline focus
13	Hu & Frank 2026	2 experiments, n=5,754	Japanese consumers	AI vs human ads: fluency boundary conditions
14	Chen 2026	Document analysis	US/EU/CN ESG reports	ESG-AI optimisation framework
15	Ni 2024	System design	DSS architecture	AI-based green-marketing decision support
16	Briana et al. 2025	Bibliometric, n=1,908	Smart cities 2000–24	Digital marketing as driver of sustainable urban branding
17	Sohaib et al. 2025	PLS-SEM + NCA	UAE survey	AI-enabled GM strategies → green intention
18	Komathi et al. 2026	fsQCA + K-means	UAE cosmetics, n=254	AI segmentation drives green purchase
19	Dong et al. 2025	Logit + LDA, 3 studies	Second-hand electronics	AI-ad effect drops when AI authorship disclosed
20	Nicolau & Petcu 2026	Qualitative + scenario	Agri-food supply chains	Blockchain+IoT+AI for green-claim verification
21	Sahoo et al. 2025	Conceptual + sentiment	Amazon reviews	AI engagement → attitude → Green Purchase Intention
22	Yin et al. 2025	Conceptual integrative	Generative AI	Dual G.R.E.E.N. circle framework
23	Ahmed et al. 2025	PLS-SEM, n=312	Malaysia	Green media → PI; AI moderates +
24	Alsaffarini & Awwad 2026	PLS-SEM + interviews	Palestinian industry	GM strongest; AI complementary
25	Alaflak et al. 2025	PLS-SEM, n=583	Egyptian tourism	SMB + AI → green tourism behaviour
26	Keskin et al. 2025	Mixed methods, n=310	Turkish firms	CE → EP via SGMO; AI moderates
27	Hu et al. 2025	CNN + regression	Green digital marketing	+27.8% sales-performance lift

ID	Author(s) Year	Method	Context / Sample	Headline focus
28	Al-Ahmed et al. 2025	Parallel mixed	Firm reports + interviews	AI moderates GM → accounting performance

3.1 Theoretical foundations and typologies

Eight theoretical lenses emerge from the corpus. The Stimulus–Organism–Response (S-O-R) lens underlies three highly cited papers on consumers' response to AI. Namely, Imran et al. [9] analyze AI-enabled tourism in China, Armutcu [10] explores the Gen-Z brand elements enabled by AI in Turkey, and Li et al. [11] examine the impact of AI-based chatbots in eco-friendly e-commerce in China. The Value–Attitude–Behavior (VAB) model informs Ma et al.'s analysis of AI-enabled purchases of green products [8]. The Antedents–Decisions–Outcomes (ADO) and Theories–Contexts–Methodologies (TCM) frameworks guide the systematic review corpus [3, 7]. Engineering studies draw on dynamic capability and resource orchestration perspectives [28], experimental advertising studies draw on the processing fluency theory and illusion of control theory [12, 13]. Mei et al. make a significant contribution by introducing the typology of Huang and Rust's mechanical, thinking, and feeling AI mapped on Kotler's 4Ps [1]; their corpus suggests Thinking AI is prevalent (about 45 studies), Mechanical AI is moderately popular (23), and Feeling AI is less common (15). Yin et al. offer the conceptual framework named Dual G.R.E.E.N. circle and describe the interplay of awareness, reward, accessibility, experience, and nudging with generational, visual, creative, educational, and narrative effects [24].

Despite the richness of theoretical approaches found in the corpus, there is limited theoretical convergence in terms of the number of different frameworks used to describe similar constructs (e.g., green purchase intention) and scarce comparative testing of competing theories. The conclusion is the presence of an abundance of conceptual approaches to green marketing but insufficient theory building.

3.2 Consumer cognition, affect, and behavioral intentions

There are nine studies analyzing how AI impacts consumer cognition, emotions, and intention related to eco-products. Specifically, AI-based green-marketing strategies (strategic, tactical, internal) contribute to trust and satisfaction, leading to increased green intention among the UAE consumers (PLS-SEM + NCA) [17]. Alaflak et al.'s empirical study of AI-based marketing activities in Egyptian tourism shows that social-media branding combined with AI contributes substantially to the explained variance in tourists' behaviors (PLS-SEM, n=583) [27]. Ma et al. reveal that egoistic, altruistic, and biospheric values predict green-AI product purchases indirectly, via attitude and price sensitivity being a moderator [8]. Armutcu, utilizing SEM-ANN approach, discovers customization, interaction, and accessibility to be the principal AI-based marketing tools that help promote eco-brands (n=609, Gen-Z in Turkey) [10]. Li et al. identify eco-advertisement attention and smart consumer social value to be dual mediators in the relationship between AI chatbot use and purchase intention in social commerce in China [11]. Imran et al. identify the affective channel (warm-glow or green happiness, eco-brands trust) in AI-enabled tourist experience [9]. Komathi et al. conduct a segmentation of cosmetics consumers via fsQCA [18]. Sahoo et al. consider greenwashing scepticism as a crucial boundary condition influencing the relationship between AI engagement and attitude [23]. Wan et al. identify AI-induced autonomy in environmental benefits and reveal its positive impact on willingness to pay in relation to the perceived consumer control [12].

Comparing the findings of those studies demonstrates that there are at least two major channels – cognitive (value perceptions, perceived consumer control, eco-advertisement attention) and affective (warm-glow, satisfaction, trust). Which channel AI inputs may follow varies by the nature of the product, timing, and consumer personality. At the same time, all studies identify AI as having a positive impact on the consumer's green purchase intention while also noting such critical factors as scepticism, greenwashing, and price sensitivity [8, 21, 23].

3.3 Generative AI and green advertising

AI-based green advertising represents a distinct experimental stream with four major findings. First, Hu and Frank conducted two experiments with a sample of Japanese consumers (n=5,754) and demonstrated that AI-generated advertisements perform just as good as human-generated for inexpensive utilitarian products but inferior in relation to high-involvement audiences [13]. In the second case, Dong et al. also discovered contingency with respect to AI-based advertisement effectiveness – second-hand electronics' consumers' green consumption intention is equally stimulated by AI-based ads and regular ads but stops when consumers learn about the true source of advertisements [21]. Finally, Wan et al. conducted a field experiment and two scenario experiments that demonstrate that AI-induced autonomous environmental benefits result in higher willingness to pay premium, mediated by perceived consumer control [12].

The bottom line is that AI can be considered an equal creative partner, but its persuasive power has clear limitations linked to processing fluency, locus of control, and disclosure of the AI's role. Thus, marketers need to strategically combine human creativity with AI-driven automation.

3.4 Greenwashing, traceability, and ESG-AI governance

Four studies are associated with the topics of AI-based governance and verification. First, Nicolau and Petcu propose a Convergent Traceability and Sustainability Authentication Framework (CTSAF) combining blockchain, IoT, and AI technology in transnational agricultural food supply chains and prove that the integrated Scenario III achieves Very High level of data accuracy according to the Green Claim Veracity Index [22]. Second, Chen analyzes ESG reports in the United States, European Union, and China and establishes that ESG becomes the predominant channel in the disclosure of AI. However, the current situation shows some gaps between AI development, application, manufacturing, and consumption processes which justify the development of the optimization framework for the ESG-AI integration [14]. Third, Hu et al.'s bibliometric analysis of 652 papers (CiteSpace) from 2017 to 2025 revealed that greenwashing ESG research cluster in the English-language literature focuses on green marketing, CSR, and legitimacy, while the Chinese-language ESG greenwashing research focuses on financing, disclosure, and governance [5]. Fourth, Paiva's PRISMA review identified blockchain and AI to be the key drivers in the traceability and marketing of circular economies [2].

The emerging picture highlights AI as a technology that can accelerate the greenwashing process or become the main driver of its deceleration. Most importantly, none of the above-mentioned studies provide an audit of AI's energy costs that would help improve its credibility.

3.5 Industry-specific applications

There are six industries receiving sustained scholarly attention. Cosmetics industry (Komathi et al.) [18] benefits from fsQCA-based segmentation for eco-product strategy. Second-hand electronics industry (Dong et al.) makes use of carbon-reduction promotions and discounts to achieve sustainable reuse [21]. Agri-food supply chains (Nicolau and Petcu) require multi-tier traceability, which requires convergence of AI, blockchain, and IoT [22]. Tourism industry (Imran et al., Alaflak et al.) uses generative AI in travel planning and social media branding to foster greater ecological and social receptivity in Chinese and Egyptian societies [9, 27]. Smart home and consumer electronics social commerce (Li et al.) use AI chatbots for persuasion [11]. Smart city urban branding (Briana et al.) explores the contribution of AI, IoT, and digital marketing to sustainability-oriented civic identity [16]. The common denominator of successful AI applications is their alignment with the characteristics of the product category.

3.6 Enterprise systems and decision support

Most enterprise-level contributions focus on productivity and decision support. Ni provides a decision support system (DSS) consisting of four layers – data collection, data processing, decision making, and user interfaces – where ML, regression, support vector machines, and reinforcement learning are applied to optimize green marketing decisions [15]. Liu and Li analyze the results of systematic literature review and perform quantitative analysis showing +22.5% conversion and approximately 15% cost reduction due to implementation of AI marketing in enterprises [4]. Hu et al. develop a convolutional neural network prediction model that helps achieve 27.8% better sales performance when combined with green development strategies [29]. Keskin et al. find that AI use has a moderation effect on the relationship between firms' circular economy capacity, strategic green marketing orientation, and environmental performance [28]. Alsaffarini and Awwad identify green marketing as the strongest predictor of corporate sustainability performance in Palestine, while AI shows a modest additional effect (mixed-method approach, n=500 and 15 interviews) [26]. Al-Ahmed et al. prove the moderation effect of AI on the relationship between green marketing and accounting performance (ROA, ROE, profit margins) [30]. In other words, all of these studies disprove the idea that AI replaces intuition in green marketing; instead, they prove the contrary and highlight that AI accelerates existing green marketing capabilities.

3.7 Engagement and gamification

Two papers focus on consumer engagement and gamification as the connection between AI and eco-friendly behavior. Specifically, Nguyen-Viet and Nguyen perform PRISMA, bibliometric, and ADO-TCM analyses of 56 papers devoted to green gamification. They identify seven thematic clusters of research but also note some underdeveloped aspects (ethics of AI, blockchain, behavioral durability) [6]. Sahoo et al. model AI customer engagement through conceptual modeling and sentiment analysis of Amazon customer reviews to demonstrate how AI nudging affects customers' attitude towards green products; greenwashing scepticism and risk perception serve as boundaries to the effect [23].
Overall, AI-driven gamification is powerful in terms of behavior replication but raises important questions in terms of behavioral durability.

3.8 Meta-research, bibliometrics, and topic modeling

Seven meta-papers were analyzed. Mei et al. and Garg et al. perform systematic reviews and summarize the state-of-the-art of AI × green-marketing field based on the analysis of 4Ps and ADO frameworks [1, 3]. Paiva and Nguyen-Viet & Nguyen cover adjacent domains, namely circular economy marketing and green gamification, respectively [2, 6]. Hu et al. and Briana et al. provide CiteSpace and VOS viewer analyses of greenwashing-related research and smart cities [5, 16]. Lastly, Kumar et al. perform topic modeling via Latent Dirichlet Allocation (LDA) and identify 2,061 papers related to their topic [7]. Methodologically, all papers reveal three recurring trends: (i) the growth in publication volumes since 2024; (ii) recurrence of themes of consumer perception, trust, and personalization; and (iii) lack of investigation of AI ethics, traceability, and Global South.

3.9 Integrative synthesis: the TIBE framework

Integrating all the insights provided in the above sections leads to the proposed TIBE (Technology Stack, Influence Paths, Boundary Conditions, Ethics and Environment) framework illustrated by Figure 2. First, the Technology stack component includes mechanical, thinking, and feeling AI as well as LLMs, ABMs, and blockchain + IoT + AI integration [1, 22, 26]. Second, the Influence Paths include cognitive (ecoadvertisement attention, value perceptions, and perceived control), affective (warm-glow, trust, and satisfaction), social (environmental vocation and social value), and normative paths (legitimacy as shown in ESG reporting) [9, 10, 11, 12, 14, 23]. Third, the Boundary Conditions aggregate all frequently observed moderators (product category and price [13], advertisement length and disclosure [13, 21], environmental locus of control [12], generation and culture [10, 27], price sensitivity [8], greenwashing scepticism [23], and AI literacy [11]). Fourth, the Ethics and Environment guardrails include AI-generated greenwashing verification via CTSAF framework [22], ESG-AI disclosure [14], energy cost, and e-waste footprint, fairness of algorithms, and moral economy of generative AI [4, 6].

T — Technology stack	I — Influence pathways	B — Boundary conditions	E — Ethical-environmental guardrails
Mechanical / Thinking / Feeling AI; LLMs; ABMs; blockchain-IoT-AI; recommender systems; CNNs; RL	Cognitive (perceived value, control, attention); Affective (warm-glow, trust, satisfaction); Social (e-vocacy); Normative (ESG legitimacy)	Product category and price; ad length; AI authorship disclosure; environmental locus of control; generation; culture; AI literacy; greenwashing scepticism	Greenwashing verification (CTSAF, GCVI); ESG-AI disclosure; AI energy and e-waste footprint; algorithmic fairness; data privacy

Figure 2. TIBE framework: a four-pillar synthesis of AI-driven green marketing.

3.10 Research Gaps and an Agenda for Future Work

Five recurrent gaps emerge. First, the literature falls short of longitudinal studies to examine whether AI-induced attitude changes result in sustained behavioral change; empirical studies are predominantly based on cross-sectional surveys or short experiments. Second, Feeling AI applications within green marketing have received surprisingly scant attention: out of more than seventy items in the general Mei et al. corpus, only fifteen refer to emotion-aware applications in marketing – in spite of emotions playing a pivotal role in domains like tourism, fashion, and food [1, 9]. Third, the carbon footprint of AI in terms of energy, e-waste, and water footprint is notably missing from this marketing-research agenda; yet, it poses a fundamental risk to the integrity of the green claims produced by AI systems [28]. Fourth, a considerable geographic imbalance exists, with many more studies conducted in Asia, the Middle East, and Mediterranean Europe than in Sub-Saharan Africa and Latin America. Finally, while techno-optimism has been a predominant theme, ethics-focused scholarship has not followed suit as regards algorithmic greenwashing, dark patterns, and persuasive autonomy [4, 6, 14]. Therefore, the following future directions should be pursued: (i) longitudinal field experiments registering AI-informed green behavior over 12+ months; (ii) interventions involving Feeling AI in tourism, fashion, and food and pitting them against text-based generation models; (iii) green marketing protocols for assessing AI's carbon footprint; (iv) global-South and cross-cultural replications; and (v) regulatory-readiness research for alignment of AI Acts (EU 2024) and EU Green Claims.

4. Conclusions

AI is reshaping green marketing in ways that are simultaneously powerful, conditional, and ethically charged. This PRISMA 2020 review of twenty-eight peer-reviewed studies published between 2024 and 2026 has shown that the field has matured rapidly along eight overlapping clusters — frameworks, consumer cognition, generative-AI persuasion, governance and traceability, industries, enterprise applications, gamification, and meta-research — yet remains theoretically fragmented and geographically skewed. The integrative TIBE framework (Technology stack, Influence pathways, Boundary conditions, Ethical-environmental guardrails) consolidates the evidence and offers an actionable lens for scholars, marketers, and policy-makers. The most consistent message is that AI works best as a complement to credible sustainability practice, never as a substitute, and that its persuasive gains are bounded by transparency, disclosure, and the AI system's own environmental footprint. Future research should pursue longitudinal, cross-cultural, and Feeling-AI evidence while explicitly auditing the ecological cost of the very algorithms that now sell green claims to consumers.

5. Acknowledgements
N/A

References

[1] Mei, Y.; Geng, L.; Cao, X.; Xie, Y. Artificial Intelligence in Green Marketing: A Systematic Literature Review. Sustainability 2025, 17, 10382. https://doi.org/10.3390/su172210382

[2] Paiva, T. A Systematic Review of Driving Sustainability through Circular Economy Marketing. Encyclopedia 2025, 5, 61. https://doi.org/10.3390/encyclopedia5020061

[3] Garg, V.; Bohara, S.; Srivastav, A. AI-driven sustainability marketing transforming consumers' perception toward eco-friendly brands. Discov. Sustain. 2025, 6, 984. https://doi.org/10.1007/s43621-025-01765-x

[4] Liu, C.; Li, Y. Research on the Application of Artificial Intelligence in Enterprise Digital Marketing. In Proc. DECS 2025, Wuhan, China, 2025.

[5] Hu, G.; Xu, Z.; Chen, W. Comparative mapping of ESG greenwashing research between China and the global context: A CiteSpace-based bibliometric analysis. Front. Sustain. 2026, 6, 1738383. https://doi.org/10.3389/frsus.2025.1738383

[6] Nguyen-Viet, B.; Nguyen, Y. T. H. Green gamification in marketing: Bibliometric mapping, framework-based systematic review, and future research agenda. Acta Psychol. 2025, 261, 105874. https://doi.org/10.1016/j.actpsy.2025.105874

[7] Kumar, S.; Sharma, C.; Mishra, M. K.; Sharma, S.; Bhardwaj, V. Smart, sustainable, and green: the digital transformation of green-marketing. Discov. Sustain. 2025, 6, 388. https://doi.org/10.1007/s43621-025-01242-5

[8] Ma, J.; Wang, Q.; Liu, D.; Pan, H.; Ran, H. Do environmental values drive artificial intelligence products green purchasing behavior? A value-attitude-behavior approach. Acta Psychol. 2025, 260, 105467. https://doi.org/10.1016/j.actpsy.2025.105467

[9] Imran, M.; Xu, H.; Wei, N.; Alzuman, A.; Jam, M.; Ahmad, N. Emotional and cognitive mechanisms of eco-social receptivity: Exploring tourism brand e-vocacy in AI-enabled travel. Acta Psychol. 2026, 263, 106311. https://doi.org/10.1016/j.actpsy.2026.106311

[10] Armutcu, B. Shaping consumer behavior with artificial intelligence and brand elements. Carbon Balance Manag. 2026, 21, 53. https://doi.org/10.1186/s13021-026-00299-w

[11] Li, J.; Yang, X.; Arshad, M. Z. Smart choices, green voices: The role of AI and social influence in eco-friendly online shopping. Acta Psychol. 2026, 265, 106734. https://doi.org/10.1016/j.actpsy.2026.106734

[12] Wan, D.; Shen, P.; Zhu, A. Are You Willing to Pay for "Greater Environmental Friendliness"? The Role of AI in Enhancing Products' Environmental Benefits. Int. J. Consum. Stud. 2026, 50, e70215. https://doi.org/10.1111/ijcs.70215

[13] Hu, Y.; Frank, B. Communicating cleaner production: When AI or human creativity enables more effective green advertising. J. Clean. Prod. 2026, 561, 148293. https://doi.org/10.1016/j.jclepro.2025.148293

[14] Chen, J. Pathways to Green AI: Information Disclosure of Artificial Intelligence Within the ESG Framework of Commercial Entities. Sustainability 2026, 18, 2922. https://doi.org/10.3390/su18072922

[15] Ni, Y. Design and Implementation of an AI-Based Green Marketing Decision Support System. In Proc. ICCSMT 2024, Xiamen, China, 2024.

[16] Briana, M.; Mitoula, R.; Sardianou, E. Sustainable Urban Branding: The Nexus Between Digital Marketing and Smart Cities. Urban Sci. 2025, 9, 278. https://doi.org/10.3390/urbansci9070278

[17] Page, M. J.; McKenzie, J. E.; Bossuyt, P. M.; Boutron, I.; Hoffmann, T. C.; Mulrow, C. D.; et al. The PRISMA 2020 statement: an updated guideline for reporting systematic reviews. BMJ 2021, 372, n71. https://doi.org/10.1136/bmj.n71

[18] Huang, M.-H.; Rust, R. T. A Strategic Framework for Artificial Intelligence in Marketing. J. Acad. Mark. Sci. 2021, 49, 30–50. https://doi.org/10.1007/s11747-020-00749-9

[19] Sohaib, O.; Alshemeili, A.; Bhatti, T. Exploring AI-enabled green marketing and green intention: An integrated PLS-SEM and NCA approach. Clean. Responsible Consum. 2025, 17, 100269. https://doi.org/10.1016/j.clrc.2025.100269
[20] Komathi, C.; Nair, S. S.; Khanna, A.; Gaur, D.; Ravisankar, S. A hybrid AI model for consumer insights and sustainable cosmetics marketing analysis in the UAE. Clean. Responsible Consum. 2026, 21, 100422. https://doi.org/10.1016/j.clrc.2026.100422
[21] Dong, Y.; Fu, B.; Lv, N.; Luo, Y. AI-Driven Advertising and Climate Change Awareness: Motivators for Green Consumption in the Second-Hand Electronics. SAGE Open 2025, 15, 1–18. https://doi.org/10.1177/21582440251357188
[22] Nicolau, A.-M.; Petcu, P. Beyond Green Labels: Leveraging Blockchain, IoT, and AI for Enhanced Traceability and Verification of Green Marketing Claims in Transnational Agri-Food Supply Chains. Sustainability 2026, 18, 782. https://doi.org/10.3390/su18020782
[23] Sahoo, S. K.; Fabus, J.; Garbarova, M.; Kvasnicova-Galovicova, T.; Pattnaik, L.; Sahoo, S. Devising AI-Based Customer Engagement to Foster Positive Attitude Towards Green Purchase Intentions. Sustainability 2025, 17, 9282. https://doi.org/10.3390/su17209282
[24] Yin, M.; Xu, W.; Wang, Y. Dual G.R.E.E.N circle: a mechanism and practical framework for promoting green consumption embedding generative AI. Environ. Res. Commun. 2025, 7, 092001. https://doi.org/10.1088/2515-7620/adfc66
[25] Ahmed, A.; Fadzilah, A. H. H.; Chan, T. J. Impact of Green Media on Purchase Intention: The Moderating Role of AI in Sustainable Marketing. Compend. paperASIA 2025, 41 (4b).
[26] Alsaffarini, E.; Awwad, B. S. The Integration Between Green Marketing and Artificial Intelligence to Achieve Corporate Sustainability. Sustainability 2026, 18, 3597. https://doi.org/10.3390/su18073597
[27] Alaflak, A.; Sharma, N.; Gawshinde, S. The impact of social media branding and AI on promoting green tourism in emerging economies like Egypt. J. Hosp. Tour. Insights 2025, 8 (9), 3496–3511. https://doi.org/10.1108/JHTI-08-2024-0886
[28] Keskin, H.; Akgün, A. E.; Esen, E. The Role of Artificial Intelligence (AI) in Enhancing Circular Economy and Strategic Green Marketing for Environmental Performance: A Mixed-Method Study. Bus. Strategy Dev. 2025, 8, e70250. https://doi.org/10.1002/bsd2.70250
[29] Hu, Q.; Xu, Q.; Wu, J.; Zhang, L. Neural network prediction model of digital marketing under the green development mode of enterprises. Discov. Comput. 2025, 28, 86. https://doi.org/10.1007/s10791-025-09568-4
[30] Al-Ahmed, H.; Alshakhetheep, K.; Shajrawi, A.; Mansour, A.; Zraqat, O.; Deeb, A.; Hussien, L. F. The impact of green marketing strategies on the accounting performance: the moderating role of AI utilization. Herit. Sustain. Dev. 2025, 7 (1), 289–300. https://doi.org/10.37868/hsd.v7i1.1074

Innovative Hybrid Activity-Based Learning Workshop Series for Developing Research Competencies in Graduate Engineering Education

Jompob Waewsak*, Chokchai Mueanmas, Ruamporn Nikom, Zaigham Ali

[1] Faculty of Engineering, Thaksin University (Phatthalung Campus), Phatthalung, Thailand;
*Correspondence: jompob@tsu.ac.th

Abstract

Graduate engineering students are expected to conduct independent research; however, conventional lecture-based instruction alone often fails to develop the practical competencies required for thesis work. This study presents the design, implementation, and evaluation of an innovative hybrid activity-based learning workshop series for a graduate Research Methodology course at the Faculty of Engineering, Thaksin University, Thailand. The hybrid model integrates conventional lecture-based learning with a series of 12 hands-on workshops covering contemporary research tools, including systematic literature review, AI-assisted manuscript preparation, computational fluid dynamics, solar and wind energy simulation, geographic information systems, reference management, design of experiments, and intellectual-property mapping. The teaching instrument was validated through Item-Objective Congruence (IOC) analysis by three experts, and its internal consistency was assessed using Cronbach's alpha. Items with an IOC index below 0.5 were removed, yielding a refined nine-item questionnaire that achieved a Cronbach's alpha of 0.844, indicating good reliability. The course outcomes were aligned with an outcome-based education (OBE) framework and assessed through a virtual thesis proposal incorporating both formative and summative rubric scoring. The results demonstrate that the proposed hybrid workshop series provides a valid and reliable approach to strengthening research competencies in graduate engineering education.

Keywords: activity-based learning; workshop series; graduate engineering education; Cronbach's Alpha

1. Introduction

Research competency is a defining outcome of graduate engineering education. Master's and doctoral students are expected to formulate research problems, critically review the literature, design rigorous methodologies, and communicate their findings to the scientific community. However, these higher-order skills are difficult to cultivate through traditional lecture-based instruction alone, in which knowledge is transmitted passively and students have limited opportunities to practice the tools and reasoning that research actually demands [1,2].

Active and activity-based learning approaches address this gap by placing students at the center of the learning process through problem-solving, hands-on practice, and reflection. A large body of evidence indicates that active learning improves performance and engagement in science, technology, engineering, and mathematics relative to passive lecturing [3]. Experiential learning theory similarly emphasizes that durable competency develops through concrete experience and active experimentation rather than listening alone [4,5]. In the contemporary research environment, these experiences increasingly involve specialized digital tools for literature analysis, simulation, data analysis, and scholarly writing, which students must be able to use confidently and ethically.

The rapid expansion of digital and artificial intelligence tools has reshaped how research is conducted and taught. Frameworks such as Technological Pedagogical Content Knowledge (TPACK) state that the effective use of such tools requires the deliberate integration of technological, pedagogical, and content knowledge rather than their incidental adoption [6]. In engineering research training, students are now expected to perform systematic literature mapping with dedicated bibliometric software [7] and draft and refine manuscripts with AI-assisted writing tools, the responsible and ethical use of which has become a distinct research competency [8]. A structured workshop series that introduces these tools within an aligned pedagogical framework offers a promising route to developing modern research competencies, provided that the instrument used to evaluate it is shown to be valid and reliable.

A substantial body of engineering education research has examined how active and inductive pedagogies translate into measurable learning gains. Inductive approaches, including inquiry-based, problem-based, and project-based learning, consistently outperform purely transmissive instruction by anchoring abstract concepts in authentic tasks and requiring learners to construct knowledge actively [9]. Problem- and project-based learning, in particular, has been widely adopted in engineering programs because it mirrors professional practice and cultivates the self-direction that research demands, although its success depends heavily on careful scaffolding and assessment design [10,11]. The flipped classroom, in which content delivery is shifted outside the class to free contact time for guided practice, has likewise shown promise for engineering instruction, with systematic reviews reporting improved engagement and performance while cautioning that outcomes vary with implementation quality [12]. Collectively, these studies establish that the pedagogical value of activity-based learning is well supported; however, they also indicate that its benefits are realized only when activities are deliberately aligned with intended outcomes and underpinned by robust assessment.

At the graduate level, however, the literature on the explicit teaching of research methodology remains comparatively thin and fragmented, despite repeated calls to treat methods instruction as a distinct competency rather than an implicit by-product of supervision [13]. Where structured training is reported, it increasingly centers on the practical tools of modern scholarship: systematic literature reviewing, which has matured into a recognized research methodology with established protocols and reporting standards [14], together with bibliometric mapping, simulation, and AI-assisted writing. Equally important, and frequently overlooked, is the methodological rigor of the instruments used to evaluate such training, as best practice in scale development requires that content validity and internal-consistency reliability be established before an instrument is used to draw inferences about learning [15]. The present study addresses both gaps by embedding contemporary research tools within a structured, outcome-aligned workshop series and formally validating the instrument used for evaluation.

Despite the recognized value of activity-based learning, few graduate research methodology courses systematically combine conventional instruction with structured, tool-oriented workshops, and even fewer report the validity and reliability of the instruments used to evaluate them. Establishing the content validity of an assessment instrument through Item-Objective Congruence (IOC) analysis [16] and its internal consistency through Cronbach's alpha [17] is essential before any conclusions about learning can be drawn. Aligning the course with an outcome-based education (OBE) framework further ensures that activities, assessments, and intended learning outcomes are constructively aligned [18]. Accordingly, this study aims to design, implement, and evaluate an innovative hybrid activity-based learning workshop series for developing research competencies in graduate engineering education and to validate the associated teaching instrument using the IOC analysis and Cronbach's alpha.

2. Materials and Methods

This study was conducted as a classroom action research in the graduate Research Methodology course offered by the Faculty of Engineering at Thaksin University (Phatthalung Campus), Thailand. The course was redesigned following an outcome-based education approach, in which the intended course learning outcomes (CLOs) were mapped to a set of learning activities and both formative and summative assessments [18,19]. The overall research methodology adopted in this study is illustrated in Figure 1.

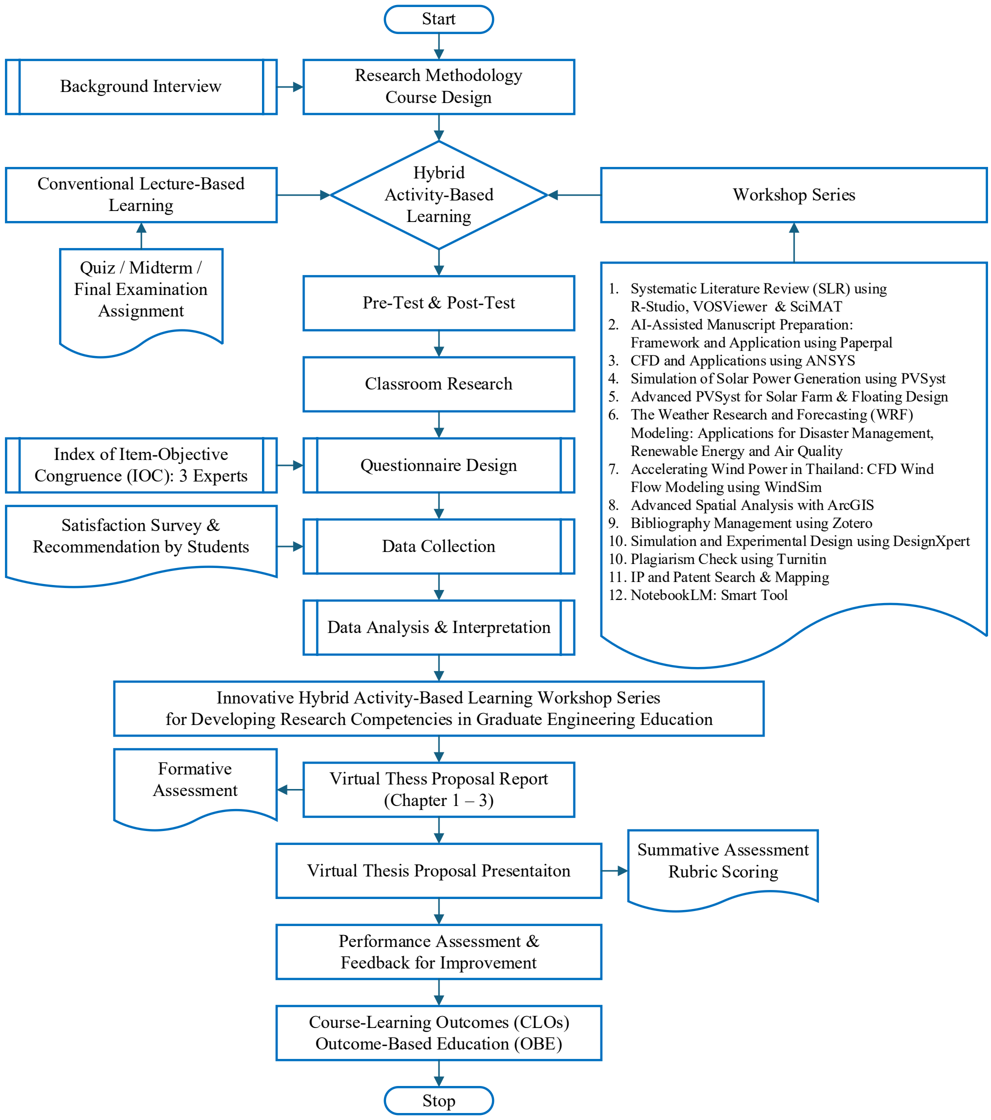

Figure 1. Research methodology used in this study.

Following a background interview and analysis of student needs, the course was structured as a hybrid model that deliberately combined conventional lecture-based learning with an activity-based workshop series. The lecture component delivers the theoretical foundations of research methodology and is assessed through quizzes and midterm and final exams. In parallel, the activity-based component immerses students in a sequence of 12 hands-on workshops, each focused on a contemporary research tool or skill.

i. Systematic Literature Review (SLR) using R-Studio, VOSViewer and SciMAT
ii. AI-assisted manuscript preparation: framework and application using Paperpal
iii. Computational fluid dynamics (CFD) and applications using ANSYS
iv. simulation of solar power generation using PVSyst
v. advanced PVSyst for solar farm and floating photovoltaic design
vi. the Weather Research and Forecasting (WRF) model for disaster management, renewable energy and air quality
vii. accelerating wind power in Thailand: CFD wind-flow modelling using WindSim
viii. advanced spatial analysis with ArcGIS
ix. bibliography management using Zotero

x. simulation and experimental design using Design-Expert
xi. intellectual-property and patent search and mapping
xii. NotebookLM as a smart research tool.

Several of these workshops draw on well-established research mapping and design-of-experiment toolchains [20,21], reflecting a CDIO-style emphasis on authentic engineering practices [22]. Student learning was monitored through a pre-test and post-test, classroom research activities, a questionnaire survey, and the collection of satisfaction ratings and recommendations. The culminating deliverable of the course is a virtual thesis proposal (Chapter 1 - 3), which is presented orally and evaluated through formative feedback and a summative-scoring rubric. Performance assessment and feedback for improvement were then fed back into the course learning outcomes, closing the outcome-based education loop. Prior to deployment, the questionnaire was examined for validity and reliability, as described in the following subsections.

2.1 Item-Objective Congruence (IOC) Analysis

The Item-Objective Congruence (IOC) index was calculated using Eq. 1.

$$\mathrm{IOC} = \frac{\sum R}{N} \tag{1}$$

where $\sum R$ is the sum of the ratings assigned by the experts to a given item, and N is the number of experts. Each of the three content experts rated every item as congruent (+1), uncertain (0), or not congruent (−1) with the corresponding objective, using the scale in Table 1. Items with an IOC index of 0.5 or greater were retained, while those below this threshold were revised or removed [16]. The initial ten-item questionnaire submitted for expert review is presented in Table 2.

Table 1. Rating scale for the index of item-objective congruence (IOC) analysis.

Score	Interpretation
+1	Clearly congruent with the objective
0	Uncertain
-1	Not congruent with the objective

Table 1 summarizes the three-point rating scale applied by the experts, and Table 2 lists the ten candidate items covering course content, instruction, analytical-thinking activities, research skill development, use of AI and digital tools, teaching media, and overall satisfaction.

2.2. Reliability Analysis

After the validated items were refined, the internal consistency reliability of the questionnaire was evaluated using Cronbach's alpha, which was calculated using Eq. 2 [17,23].

$$\alpha = \frac{k}{k-1}\left(1 - \frac{\sum \sigma_i^2}{\sigma_t^2}\right) \tag{2}$$

where k is the number of items, $\sum \sigma_i^2$ is the sum of the individual item variances, and σ_t^2 is the variance of the total scores. A Cronbach's alpha value of 0.7 or above is generally regarded as acceptable for research instruments [23,24]. The interpretation of the reliability levels used in this study is presented in Table 3.

Table 2. Initial questionnaire for the index of item-objective congruence (IOC) analysis.

No.	Question Item	+1	0	-1
1	The course content is clear and easy to understand			
2	The instructor explains the content systematically			
3	The learning activities help promote analytical thinking			
4	Students can define research problems better			
5	Students can set research objectives			
6	Students can design research instruments			
7	Using AI or Digital Tools helps in better understanding the lessons			
8	The teaching media are modern and appropriate			
9	Students have greater confidence in conducting research			
10	Overall satisfaction with this course			

Table 3. Cronbach's alpha reliability levels.

Cronbach's Alpha	Reliability Level
>0.9	Excellent
0.80 – 0.89	Good
0.70 – 0.79	Acceptable
0.60 – 0.69	Questionable
0.50 – 0.59	Poor
<0.5	Unacceptable

3. Results and Discussion

3.1. Validity (Item-Objective Congruence) Results

The content validity of the questionnaire was first established through an Item-Objective Congruence (IOC) analysis. The ratings of the three experts for each of the ten items, together with the resulting total scores and IOC indices, are presented in Figure 2.

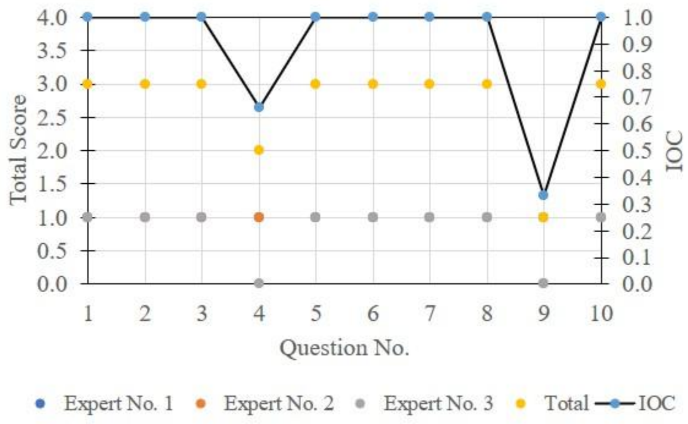

Figure 2. Index of item-objective congruence (IOC) analysis.

As shown in Figure 2, eight of the ten items (items 1–3, 5–8, and 10) obtained a perfect IOC index of 1.00, indicating unanimous agreement among the experts that these items were congruent with their objectives. Item 4 obtained an IOC of 0.67, which is above the 0.5 threshold and was therefore retained after minor wording revision, whereas item 9 obtained an IOC of only 0.33 and was removed from the instrument. Thus, the refined questionnaire retained nine items, all of which had acceptable content validity.

3.2. Reliability (Cronbach's Alpha) Results

The reliability of the refined nine-item questionnaire was evaluated using three respondents on a five-point Likert scale [20]. The individual item scores are presented in Figure 3.

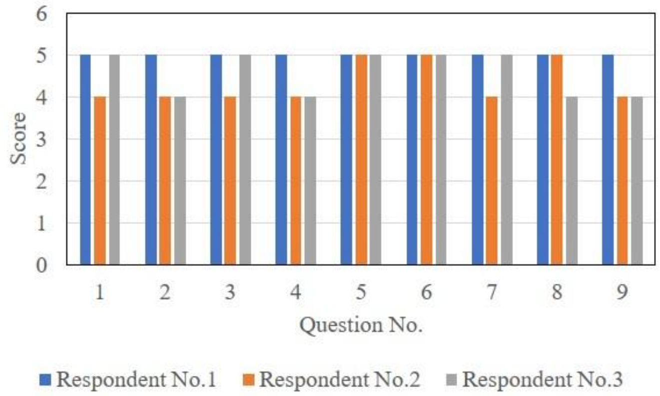

Figure 3. The testing results of the improved questionnaire showed a Cronbach's alpha of 0.844 (>0.7 is acceptable).

Using the response data in Figure 3, the number of items was k = 9, the sum of the item variances was $\sum\sigma_i^2 = 2.333$, and the variance of the total scores was $\sigma_t^2 = 9.333$. Substituting these values into Eq. 2 gives a Cronbach's alpha of 0.844. According to the interpretation in Table 3, this value lies in the 0.80–0.89 range and corresponds to a good level of internal consistency reliability, comfortably exceeding the 0.7 threshold that is commonly recommended for research instruments [23,24].

Taken together, the IOC and Cronbach's alpha results confirm that the questionnaire is both valid and reliable for evaluating the hybrid activity-based learning workshop series. The high agreement among experts indicates that the items are well aligned with the intended course learning outcomes, while the strong internal consistency indicates that the items measure the targeted research competency construct coherently.

Typically, following the validation of questionnaire items through the Item-Objective Congruence (IOC) method and the assessment of internal consistency using Cronbach's alpha, the finalized questionnaire is administered to the study sample. However, because the total population of graduate students enrolled in the course consisted of only three students, separate pilot-testing and actual-survey groups could not be established. Consequently, the same respondents were employed for both the refinement of the questionnaire and the estimation of Cronbach's alpha reliability. This methodological decision was necessitated by the small population size and the classroom-based nature of the study.

In addition, the students suggested the inclusion of supplementary workshops and learning activities on advanced research skills, particularly in data analysis and graphical presentation techniques using emerging tools such as R and Python programming languages. They believed that these competencies would enhance their research capabilities and support the successful completion of their theses and dissertations. The feedback obtained from both the questionnaire and interview processes provides valuable insights for the continuous improvement of teaching and learning practices in graduate engineering education.

These findings are consistent with the broader literature reporting that active and activity-based learning improves engagement and skill acquisition in engineering education [2,3] and that authentic inquiry-based experiences are particularly effective for developing research capability [25]. By embedding contemporary research tools within a structured workshop series and aligning the assessment with an outcome-based framework, the proposed approach connects theoretical instruction to the practical demands of thesis work. The validated instrument provides a sound basis for subsequent measurements of student satisfaction and learning gains across larger cohorts.

4. Conclusion

This study designed, implemented, and evaluated an innovative hybrid activity-based learning workshop series for developing research competencies in graduate engineering education at Thaksin University. The course integrates conventional lecture-based learning with 12 hands-on workshops on contemporary research tools and aligns its activities and assessments with an outcome-based education framework culminating in a virtual thesis proposal. The teaching instrument was validated rigorously. Item-Objective Congruence analysis by three experts identified one item with an IOC index below the 0.5 threshold, which was removed, leaving a refined nine-item questionnaire with strong content validity. The internal consistency reliability of this refined instrument, measured by Cronbach's alpha, was 0.844, which corresponds to a good level of reliability and exceeds the recommended threshold. These results demonstrate that the proposed hybrid workshop series, together with its validated evaluation instrument, provides a valid and reliable approach to strengthening research competencies in graduate engineering education. Future work will deploy the validated instrument with larger student cohorts and across multiple course offerings to quantify learning gains, satisfaction, and the longer-term impact of the workshop series on thesis quality and research productivity. Beyond quantifying learning gains, future research will examine how individual workshops in the series contribute to specific research competencies and explore the transferability of the hybrid model to other engineering disciplines and institutions. Embedding the validated instrument within a continuous-improvement cycle is expected to support the ongoing refinement of both the workshop content and its assessment, thereby reinforcing the constructive alignment between learning activities, intended learning outcomes, and graduate research practice.

5. Acknowledgement

The authors would like to express their sincere appreciation to the Division of Student Affairs, Thaksin University, for its financial support of the workshop series on activity-based learning. The authors are also deeply grateful to Asst. Prof. Dr. Sirilak Chuaypanang (TH-PSF Level 3) of the Faculty of Agriculture, Thaksin University (Phatthalung Campus), and Asst. Prof. Dr. Chuleerat Kongruang, Senior Fellow of Advance (SFHEA) of the School of Accountancy and Finance, Walailak University, for their invaluable guidance, constructive suggestions, and insightful recommendations, which significantly contributed to the completion of this work.

References

[1] Bonwell, C. C.; Eison, J. A. Active Learning: Creating Excitement in the Classroom; ASHE-ERIC Higher Education Report No. 1; The George Washington University: Washington, DC, USA, 1991.
[2] Prince, M. Does Active Learning Work? A Review of the Research. J. Eng. Educ. 2004, 93, 223–231.
[3] Freeman, S.; Eddy, S. L.; McDonough, M.; Smith, M. K.; Okoroafor, N.; Jordt, H.; Wenderoth, M. P. Active Learning Increases Student Performance in Science, Engineering, and Mathematics. Proc. Natl. Acad. Sci. U.S.A. 2014, 111, 8410–8415.
[4] Kolb, D. A. Experiential Learning: Experience as the Source of Learning and Development, 2nd ed.; Pearson Education: Upper Saddle River, NJ, USA, 2015.
[5] Felder, R. M.; Brent, R. Teaching and Learning STEM: A Practical Guide; Jossey-Bass: San Francisco, CA, USA, 2016.
[6] Mishra, P.; Koehler, M. J. Technological Pedagogical Content Knowledge: A Framework for Teacher Knowledge. Teach. Coll. Rec. 2006, 108, 1017–1054.

[7] van Eck, N. J.; Waltman, L. Software Survey: VOSviewer, a Computer Program for Bibliometric Mapping. Scientometrics 2010, 84, 523–538.
[8] Kohnke, L.; Moorhouse, B. L.; Zou, D. ChatGPT for Language Teaching and Learning. RELC J. 2023, 54, 537–550.
[9] Prince, M. J.; Felder, R. M. Inductive Teaching and Learning Methods: Definitions, Comparisons, and Research Bases. J. Eng. Educ. 2006, 95, 123–138.
[10] Mills, J. E.; Treagust, D. F. Engineering Education—Is Problem-Based or Project-Based Learning the Answer? Australas. J. Eng. Educ. 2003, 3, 2–16.
[11] Kokotsaki, D.; Menzies, V.; Wiggins, A. Project-Based Learning: A Review of the Literature. Improving Schools 2016, 19, 267–277.
[12] Karabulut-Ilgu, A.; Jaramillo Cherrez, N.; Jahren, C. T. A Systematic Review of Research on the Flipped Learning Method in Engineering Education. Br. J. Educ. Technol. 2018, 49, 398–411.
[13] Earley, M. A. A Synthesis of the Literature on Research Methods Education. Teach. High. Educ. 2014, 19, 242–253.
[14] Snyder, H. Literature Review as a Research Methodology: An Overview and Guidelines. J. Bus. Res. 2019, 104, 333–339.
[15] DeVellis, R. F. Scale Development: Theory and Applications, 4th ed.; SAGE Publications: Thousand Oaks, CA, USA, 2017.
[16] Rovinelli, R. J.; Hambleton, R. K. On the Use of Content Specialists in the Assessment of Criterion-Referenced Test Item Validity. Tijdschr. Onderwijsres. 1977, 2, 49–60.
[17] Cronbach, L. J. Coefficient Alpha and the Internal Structure of Tests. Psychometrika 1951, 16, 297–334.
[18] Biggs, J.; Tang, C. Teaching for Quality Learning at University, 4th ed.; Open University Press: Maidenhead, UK, 2011.
[19] Spady, W. G. Outcome-Based Education: Critical Issues and Answers; American Association of School Administrators: Arlington, VA, USA, 1994.
[20] Likert, R. A Technique for the Measurement of Attitudes. Arch. Psychol. 1932, 22, 5–55.
[21] Aria, M.; Cuccurullo, C. bibliometrix: An R-Tool for Comprehensive Science Mapping Analysis. J. Informetr. 2017, 11, 959–975.
[22] Crawley, E. F.; Malmqvist, J.; Östlund, S.; Brodeur, D. R.; Edström, K. Rethinking Engineering Education: The CDIO Approach, 2nd ed.; Springer: Cham, Switzerland, 2014.
[23] Tavakol, M.; Dennick, R. Making Sense of Cronbach's Alpha. Int. J. Med. Educ. 2011, 2, 53–55.
[24] Taber, K. S. The Use of Cronbach's Alpha When Developing and Reporting Research Instruments in Science Education. Res. Sci. Educ. 2018, 48, 1273–1296.
[25] Healey, M.; Jenkins, A. Developing Undergraduate Research and Inquiry; Higher Education Academy: York, UK, 2009.